Doctoral Thesis

Cardiovascular optoacoustic tomography for real-time imaging of rodent models and handheld investigations

Author(s):
Ivankovic, Ivana

Publication Date:
2020

Permanent Link:
https://doi.org/10.3929/ethz-b-000440784 →

DISS. ETH NO. 26799

Cardiovascular Optoacoustic Tomography for Real-Time Imaging of Rodent Models and Handheld Investigations

A thesis submitted to attain the degree of

DOCTOR OF SCIENCES of ETH ZURICH

(Dr. sc. ETH Zurich)

Presented by
IVANA IVANKOVIC

M.Sc Bioengineering, University College Dublin

Born on 6th June 1992

Citizen of United Kingdom

Accepted on the recommendation of

Prof. Dr. Daniel Razansky

Prof. Dr. med. Susanne Wegener

Prof. Dr. Orçun Göksel

2020

Acknowledgements

I would first like to thank Prof. Daniel Razansky, to whom to I am very grateful for, for taking me on with my ‘diverse’ academic background. I thank you for the opportunity and freedom to explore new things with guidance and motivation on the way. I will always appreciate that.

Xose-Luis Dean-Ben, you have been instrumental to my PhD and I really couldn’t have done it without you. Showing me everything from reconstructions in Matlab to switching on a laser and coupling fibres to the 1064nm output; I will never forget how much you taught me and also the patience you had, as I really entered the lab knowing very little. Thank you, you are wonderful!

To my lab, such a brilliant group of people: Amy, Ben, Ali, all of you! The time throughout my PhD would absolutely not be the same without you. I especially want to thank Johannes and Urs, who have both become like brothers to me. What a ride it has been with you both - friendships for life. Also to my non-lab friends including amazing Mary and my wonderful new friends of Zurich. But most importantly to those friends that have supported me from afar, especially Killian who has been there every step of the way with me.

Finally, the most important and largest thanks goes to my family; Mama, Tata, Davor and Mia (and Ollie). Firstly, I obviously wouldn’t be here without you… but thank you for *always* being there with constant good advice and the best family ‘recharge’ trips throughout the year. You’re some family. Kucaposao.

English Summary

Cardiovascular diseases (CVDs) remain the leading cause of death worldwide with myocardial infarction and stroke as their main clinical manifestations. Advanced imaging techniques are required to gain further insight into the underlying biological processes of CVD, especially to capture *in vivo* dynamics non-invasively. Optoacoustic imaging is a biomedical imaging technology based on light absorption of biological tissues causing thermal expansion of molecules, which then emit detectable ultrasound waves. This phenomenon is known as the optoacoustic[1] (OA) effect. In optoacoustic tomography (OAT), a single nano-second laser pulse allows volumetric imaging with optical contrast at centimetre-scale depths, hence serving as a valuable imaging modality for deep tissue imaging of rapid cardiovascular dynamics. In particular, the strong optical absorption of haemoglobin in the near-infrared wavelength range allows detection of numerous cardiovascular structures. OAT has been successfully applied to study different aspects of the cardiovascular system, but is still not considered a standard tool for cardiovascular imaging because of technical limitations and a small number of preclinical and clinical studies. This thesis thus further explores potential applications and usability of OAT for preclinical and clinical use by capitalizing on its unique volumetric, real-time and non-invasive capabilities, therefore addressing current limitations in cardiovascular imaging. In particular, the capabilities of OAT will be assessed as a preclinical imaging modality in murine models of heart disease, including myocardial infarction and pulmonary heart disease. OAT will also be assessed on a human scale, specifically geared towards carotid artery imaging.

---

[1] Also known as photoacoustic effect.

German Summary

Herz-Kreislauferkrankungen sind die verbreitetste Todesursache weltweit. Herzinfarkt und Schlaganfall stellen dabei die beiden häufigsten klinischen Krankheitsbilder dar. Fortgeschrittene Bildgebungsverfahren werden benötigt um vertiefte Einblicke in die biologischen Prozesse hinter Herz-Kreislauferkrankungen zu erlangen mit besonderem Augenmerk auf dynamische, nicht-invasive und *in vivo* Verfahren. Optoakustische Bildgebung ist eine biomedizinische Bildgebungstechnologie basierend auf der Absorption von Licht in biologischem Gewebe welche zu temporärer thermischer Expansion von Molekülen und damit der Entstehung von Ultraschallwellen führt, auch bekannt als der optoakustische Effekt. Optoakustische Tomographie (OAT) erlaubt volumetrische Bildgebung basierend auf einzelnen Nanosekunden Laserpulsen und verbindet optischen Kontrast mit Ultraschall basierter Tiefenauflösung und stellt ein vielversprechendes Bildgebungsverfahren dar um schnelle kardiovaskuläre Prozesse zu beobachten. Die starke optische Absorption von Hämoglobin im Nahinfrarot erlaubt die Detektierung verschiedener kardiovaskulärer Strukturen. OAT wurde erfolgreich verwendet um verschiedene Aspekte des kardiovaskulären Systems zu untersuchen und kann dennoch nicht als ein Standardtool in Biologie und Medizin bezeichnet werden aufgrund technischer Limitierungen und einer geringen Anzahl vorklinischer und klinischer Studien. In Rahmen dieser Arbeit wurden potentielle Anwendungen und Nutzbarkeit von OAT für vorklinische und klinische Verwendung erörtert. Durch die einzigartige Kombination von volumetrischer und nicht-invasiver Bildgebung in Echtzeit konnten existierende Limitierungen in kardiovaskulärer Forschung überbrückt werden. Im Speziellen wurde OAT als ein vorklinisches Bildgebungsverfahren für Mausmodelle mit Herz-Kreislauferkrankungen wie Herzinfarkt und Lungenherz evaluiert. Die Anwendung für menschliche Bildgebung wurde am Beispiel der Halsschlagader exploriert.

Curriculum Vitae

Education and Work Experience

Post-Doctoral Researcher, ETH Zurich; ***Aug 20 - Current***

- Prof. Daniel Razansky Lab
- Institute of Biomedical Engineering
- Institute of Pharmacology and Toxicology (University of Zurich)

PhD Candidate, ETH Zurich; ***Jan 19 – Jun20***

- Prof. Daniel Razansky Lab
- Institute of Biomedical Engineering
- Institute of Pharmacology and Toxicology (University of Zurich)

PhD Candidate, Technical University Munich, Munich; ***Oct 16 – Jan 19***

- Prof. Daniel Razansky Lab
- Four Dimensional Molecular Optoacoustic Imaging of the Cardiovascular System
- Scholarship at International Graduate School of Science and Engineering
- Institute of Biological and Medical Imaging, Helmholtz Centre Munich

Research Assistant, Royal College of Surgeons Ireland (RSCI), ROI: ***Oct 15 – Sep 16***

- Research assistant in Bioengineering within the School of Pharmacy
- Airway tissue engineering

Lab Demonstrator, RSCI, ROI:

- Pharmaceutics for university students ***May 16***

Consultancy, *Maxxos Medical Ltd* & Prof R. Flavin, ROI: ***July 15***

- Finite element analysis of orthopaedic medical devices

MSc in Bioengineering, University College Dublin (UCD), ROI: ***Sep 14 – Aug 15***

- First Class Honours (1.1 – GPA 3.72/4.2)
- Graduated first in class
- Thesis: Experimental and Numerical Investigation of the Mechanical Behaviour of Medial and Anterolateral Distal Tibial Plates

B.A Natural Sciences (Zoology specialisation), Trinity College Dublin (TCD), ROI: ***Oct 10 – May 14***

- Second Class Honours Grade 1 (2.1 or 66%)
- Thesis: Expression of the p53 Gene Network in the Developing Chick Retina

Tutoring, ROI:

- IT-Tuition Ireland – Biology, Geography and Art – Leaving Certificate
- Tutor for secondary school student in all Junior certificate subjects ***Oct 12 – May 15***

Research Support Assistant, UCD, ROI: ***Jun 13 – Aug 13***

- School of Mechanical and Materials Engineering

Secondary School, Holy Child Killiney (HCK), ROI: ***Sep 04 – Jun 10***

- Leaving Certificate (All higher level) – 505/600 points
- Junior Certificate (All higher level) – 8A’s & 2B’s

- German Award
- Member of Senior 1st Hockey team

Scientific Techniques and Expertise

- **Imaging Techniques:** Optoacoustic (photoacoustic) imaging. Human vasculature imaging (carotid artery). Pre-clinical animal imaging (murine models).
  Molecular imaging (contrast and contrast free). Real-time Imaging. Dynamic Imaging. Multispectral Imaging. Ultrasound imaging (limited experience). Scanning Electron microscopy (image analysis).
- ***In vivo* Studies:** Felasa B certificate for animal handling and *in vivo* imaging studies (murine).
- **Image Analysis:** Matlab for image reconstruction. Amira and Fiji for image visualisation.
- **Prototyping:** Autodesk Inventor, 3D mechanical design, 3D printing.
- **Mechanical testing:** Experimental: Fatigue, tensile and compression testing. Numerical: Finite Element Analysis (Abaqus).
- **Tissue Engineering:** Electrospinning scaffolds. Electrospraying (drug delivery).
- **Molecular Techniques:** qPCR, RT-PCR, DNA preparation, RNA extraction, Bone marrow extraction.
- **Software:** Microsoft office package, Matlab, Abaqus, Fiji, Amira, Inventor.

Publications

- **Coregistration and spatial compounding of optoacoustic cardiac images via Fourier analysis of four-dimensional data**
  *Li H**, Ivankovic I.,** Li J., Razansky D., & Dean-Ben XL **Applied Sciences (2020)***

- **Volumetric Optoacoustic Tomography Differentiates Myocardial Remodelling**
  Ivankovic, I**., Déan-Ben, X. L, Haas, H., Kimm, A.M., Wildgruber, M. & Razansky, D**. Molecular Imaging and Biology (2020)

- **The Fabrication and in vitro Evaluation of Retinoic Acid-Loaded Electrospun Composite Biomaterials for Tracheal Tissue Regeneration**
  *O'Leary, C. Soriano, L, Fagan Murphy, A., **Ivankovic, I**., Cavanagh, L.B., & O'Brien, J.F. **Frontiers in Bioengineering and Biotechnology (2020)***

- **Non-invasive 3D imaging of the human carotid artery with volumetric multispectral optoacoustic tomography (vMSOT)**
  Ivankovic I., &** Razansky, D. **Diagnostic Imaging Europe (2019)

- **Rapid Non-invasive Functional Assessment of the Human Carotid Artery with Handheld Volumetric Multi-Spectral Optoacoustic Tomography;**
  Ivankovic, I**., Merčep, E., Deán-Ben, X.L., & Razansky, D. **Radiology (2019)

- **Volumetric Optoaoustic Tomorgraphy Enables Non-invasive *in vivo* Characterisation of Impaired Heart Function in Hypoxic Conditions**
  Ivankovic, I**., Hsiao-Chun, A.L., Déan-Ben, X. L., Zhang, Z., Gorlach, A., & Razansky, D. **Scientific Reports (2019)

- **In vivo assessment of heart function under chronic hypoxic stress with volumetric optoacoustic tomography**
  Ivankovic I.,** Lin, H.C.A., Dean-Ben X.L, Zhang, Z., Trautz, B., Gorlach, A., & Razansky, D. **Photons Plus Ultrasound: Imaging and Sensing, International Society for Optics and Photonics (2019)

- **Characterization of Cardiac Dynamics in an Acute Myocardial Infarction Model by Four-Dimensional Optoacoustic and Magnetic Resonance Imaging;**
  *Lin, H. C. A., Déan-Ben, X. L., **Ivankovic, I.**, Kimm, M. A., Kosanke, K., Haas, H., Reinhard, M., Lohofer, F, Wildgruber, M., & Razansky, D. **Theranostics (2017)***

Presentations

- **'Volumetric Optoaoustic Tomorgraphy Enables Non-invasive *in vivo* Characterisation of Impaired Heart Function in Hypoxic Conditions'**
  SPIE Photonics West; BiOs Conference; San Francisco, USA. *February 2019. (Speaker)*

- **'Rapid Non-invasive Functional Assessment of the Human Carotid Artery with Handheld Volumetric Multi-Spectral Optoacoustic Tomography'**
  12th European Molecular Imaging Meeting (EMIM); San Sebastian, Spain. *March 2018. (Poster Presentation)*

- **'Rapid Non-invasive Functional Assessment of the Human Carotid Artery with Handheld Volumetric Multi-Spectral Optoacoustic Tomography'**
  SPIE Photonics West; BiOs Conference; San Francisco, USA. *January 2018. (Speaker)*

Grant contributions

- **Research Equipment (R'Equip) awarded by the Swiss National Science Foundation (SNF), Zurich, Switzerland (2019).**
  Grant awarded for top-quality, innovative research equipment: Multispectral Optoacoustic Tomography (MSOT) for implementation into University Zurich Hospitals (UZS). (Contribution in grant writing, project organisation, meeting organisation)

- **GRC Grant for Junior Researchers awarded by the Graduate Campus of University of Zurich, Switzerland (2019).**
  Student-run transferable skills workshop – 'Lab Hack Days'. (Contribution in grant editing, workshop organising and in teaching assistance in workshop.

- **Irish Research Council Government of Ireland Postgraduate Scholarship Scheme. Dublin, Ireland (2016)**
  Granted scholarship for funded doctoral position – however not undertaken. (Contribution in grant writing)

Other Skills

- **Classical Ballet:** Grades 1-8 passed with distinction; Royal Academy of Dance. Preformed several shows in London and Dublin. Irish tours with 'Music in the Classroom'.
- **Modern Dance:** Sneakers Dance Group, Munich, TTC. Winners of Oberliga Sud, Deutschland. Several shows preformed in Dublin.
- **Sport:** Skiing (Advanced level – Secretary of TCD Snow Sports Club), Swimming (Several medals in races), Hockey (Member of senior 1st team, HCK). Tag rugby (competitions).
- **Art:** Painting (commissioned a painting). Drawing.
- **Music:** Violin (Grades 1 -4).
- **Awards:** IRSC Foundation Scholarship, Ireland. German Student Awards for Final Year (HCK).

References

Prof. Daniel Razansky
PhD Supervisor
daniel.razansky@uzh.ch
+41 446355932

Prof Robert Flavin
MSc Thesis Supervisor, Trauma and Orthopaedic Surgeon
footankleframe@gmail.com
+353 1 263 8825

Dr. Eoin O'Cearbhaill
MSc Bioengineering Coordinator
Lecturer
eoin.ocearbhaill@ucd.ie
+353 01 716 1715

Contents

Abbreviations

Figure list

Abbreviations

ANOVA – Analysis of variance

CA – Carotid artery

CAB – Carotid artery bifurcation

CAD – Coronary artery disease

CCA – Common carotid artery

c-kit^{+} – c-kit positive

COPD – Chronic obstructive pulmonary disorder

CPTT – Cardiopulmonary transit time

CSCs – Cardiac stem cells

CT – Computed tomography

CVD – Cardiovascular disease

CW – Carotid wall

ECA – External carotid artery

FB – Fibre bundle

FFPE – Formalin fixed and paraffin embedded

FOV – Field of view

Hb – Deoxygenated haemoglobin

HbO – Oxygenated haemoglobin

HF – Heart failure

HIF – Hypoxia-inducible factor

I/R – Ischemic-reperfusion

ICA – Internal carotid artery

ICG – Indocyanine green

$\mathit{kit}^{W}/\mathit{kit}^{W\text{-}v}$ – c-kit deficient

LAD – Left anterior descending coronary artery

LB – Laser beam

LRNC – Lipid rich necrotic core

LV – Left ventricle

LVEF – Left ventricular ejection fraction

MI – Myocardial infarction

MIPs – Maximum intensity projections

MRI – Magnetic resonance imaging

MSOT – Multispectral optoacoustic tomography

NIR – Near-infrared

OA – Optoacoustic imaging

PH – Pulmonary hypertension

PHD – Pulmonary heart disease

PO – Permanent occlusion

PTT – Pulmonary transit time

ROI – Region of interest

RV – Right ventricle

S – Skin

SNR – Signal to noise ratio

STA – Superior thyroid artery

STFT – Short-time Fourier transform

TA – Transducer array

TM – Transparent membrane

US – Ultrasound

UW – Ultrasound waves

vMSOT – Volumetric multispectral optoacoustic tomography

VOT – Volumetric optoacoustic tomography

WH – Water holder

wt – Wild type

1. Introduction

Cardiovascular disease (CVD) remains the leading cause of mortality worldwide, where myocardial infarction (MI) and stroke are the main clinical manifestations of CVD (Roth et al., 2017a). In the past decade, there has been significant progress on improving the outlook of CVD (Arnett et al., 2019); nevertheless, the unceasing high mortality rates only emphasize the necessity to continue advanced research on CVD. CVD is subject to multiple risk factors that can be considered as either modifiable risk factors (high cholesterol, tobacco-smoking) and non-modifiable risk factors (family history, gender), making research efforts particularly difficult due to the multifactorial nature of CVD (Kumar, 2017). Heart failure is a common result of CVD, which can stem from coronary artery disease (CAD) that leads to MI; and also pulmonary heart disease (PHD), which develops from a non-cardiac origin (discussed in detail in Section 1.1). Additionally, CVD can lead to injury of the brain, commonly caused by a stroke (discussed in detail in Section 1.2). It is therefore crucial to explore a variety of approaches for elucidating CVD, including efforts in both preclinical and clinical research.

1.1 Heart failure

CAD is one of the main causes of HF and drives mechanical and electrical alterations within the myocardium causing ventricular dysfunction. The coronary arteries supply blood directly to the heart and in CAD, blood flow is significantly reduced causing ischemia of the myocardium. The underlying cause of CAD is atherosclerosis; the thickening of the arterial wall due to endothelial dysfunction, which will be discussed in detail in Section 1.2. Ischemia of the myocardium, most commonly known as myocardial infarction (MI) is the main outcome of CAD, where part of the myocardium is deteriorated due to the death of cardiomyocytes from lack of oxygen (Roth et al., 2017b). The reduced blood flow increases the workload on the heart to counteract the reduced oxygen supply. This in turn induces various mechanisms of ventricular dysfunction or remodelling, including hypertrophy (thickening of ventricular muscle), dilation (enlargement of ventricle) and arrhythmia (irregular heartbeat), as illustrated in Figure 1.1. These alterations in the mechanical and electrical architecture of the heart are driving factors that lead to HF.

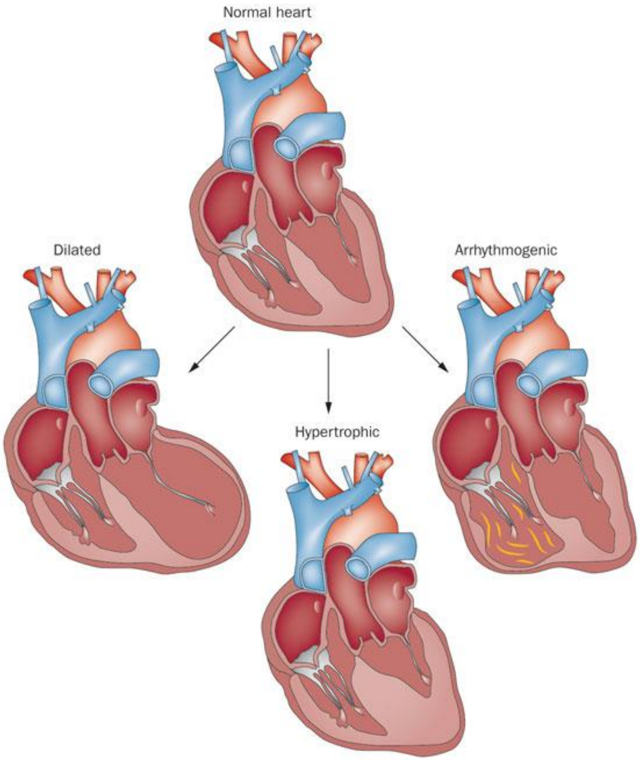

Figure 1.1 Schematic of healthy and diseased myocardium. A normal healthy heart (top). Dilated (left), hypertrophic (bottom) and arrhythmogenic (right) are examples of symptoms of a dysfunctional myocardium that may lead to heart failure. *Reprinted with permission from CodeHealth: https://codehealth.io/library/article-49/the-cardiomyopathies/*

Although CAD is the most common cause of HF, it is important to acknowledge the effects of non-cardiac dysfunction on the myocardium and its influence towards HF. Various non-cardiac diseases can compromise the physiological function of the heart, for example, impairment of the kidneys or lungs (Lam et al., 2011b). Ventricular dysfunction, such as hypertrophy and arrhythmia, can commonly occur in response to non-cardiac diseases without the presence of HF. However, these cardiac symptoms can be important indicators or precursors of HF and should be understood in greater detail. The pulmonary circuit, which involves blood circulation between the lungs and heart is a prime example where heart function can be severely altered by pulmonary dysfunction. Pulmonary hypertension (PH) is such an example, where deteriorated lung function has large implications on heart function causing PHD.

1.1.3. Myocardial infarction

Ischemic myocardial injury is a result of a prolonged period of reduced oxygen supply to the myocardium, where morphological, functional and molecular changes occur in the myocardium. The length and severity of the ischemic event defines the patient’s prognosis, with delayed treatment times strongly increasing the chance of irreversible loss of cardiomyocytes, which in turn can lead to HF (Cho, Fernandez, & Kwon, 2014).

1.1.3.1 Myocardial regeneration

A major issue facing the treatment of MI is the limited regenerative capacity of the heart. Until recently it has been thought that the heart is a post-mitotic organ, however it has become clear that it possesses a small capability of renewal. Studies showed that the capacity of renewal was approximately 1% per annum for younger hearts, further decreasing with age (Bergmann et al., 2009). Myocardial regeneration following MI involves multiple complex processes including scar tissue formation, inflammation and angiogenesis (T. J. Cahill, Choudhury, & Riley, 2017).

Due to the limited regeneration capabilities of the myocardial tissue, restoration of injured or dead cardiomyocytes would be a highly effective way for myocardial repair, thus research efforts have focused on different pathways to promote cardiac stem cell (CSC) repair as a possible method for myocardial restoration (T. J. Cahill et al., 2017) A cell surface receptor has been of particular interest for myocardial regeneration, known as c-kit (Ellison et al., 2013; Keith & Bolli, 2015). c-kit is a tyrosine kinase receptor expressed throughout the body, responsible for binding to a stem cell factor by activation of a downstream signalling cascade. c-kit positive (c-kit^{+}) expression in CSCs has caused controversy due to the inconsistency and questionable reporting of results (Zhou & Wu, 2018). Clinical trials showed small improvements in cardiac function after c-kit^{+} transplantation, however patient numbers were low with uncertainty whether improvement in cardiac function was directly a result of c-kit^{+} transplantation (Makkar et al., 2012). c-kit^{+} cells have an effect on cardiac regeneration after MI, however the basic understanding and scale of the process remains unclear. It is therefore crucial to gain a deeper understanding of the c-kit effect post MI, particularly in pre-clinical models before attempting clinical trials (Zhou & Wu, 2018).

1.1.4 Pulmonary heart disease

PHD is an umbrella term for altered heart function in response to impaired respiratory function (Forfia, Vaidya, & Wiegers, 2013). HF can be caused by many factors that directly affect the heart, however it is important to take into account how pathologies of non-cardiac origins can also be an indirect cause of HF (Lam et al., 2011).

1.1.4.1 Chronic pulmonary hypoxia

A hypoxic pulmonary environment can stem from various respiratory disorders including chronic obstructive pulmonary disorder (COPD), sleep disordered breathing; and also from high altitudes (Bärtsch & Gibbs, 2007; Stenmark, Fagan, & Frid, 2006). Hypoxic conditions induce processes of vascular remodelling within the lungs (Stenmark et al., 2006). In acute hypoxia (short period of time with reduced oxygen), the pulmonary vasculature rapidly constricts in response, however when normal oxygen levels or normoxic conditions are returned, the effect is reversible. In chronic hypoxic conditions, such as in COPD, the outcome is more severe (Bärtsch & Gibbs, 2007; Blanco, Piccari, & Barberà, 2016). Pulmonary vasoconstriction also occurs, however unlike in acute hypoxia, the reversibility of the effect is limited. One of the main results of pulmonary vasoconstriction due to hypoxia is caused by the muscularization of otherwise non-muscular arteries resulting from increased smooth muscle actin (α – SMA) proliferation (Stenmark et al., 2006).

Remodelling of the pulmonary vasculature induces an increased workload on the heart, specifically on the right ventricle (RV), which is thin walled compared to the left ventricle (LV). The sustained increased resistance of the remodeled pulmonary vasculature resulting from chronic hypoxia causes a pressure-overload on the RV and PH. This in turn leads to systolic and diastolic dysfunction, RV hypertrophy, dilation, and arrhythmias (Charolidi & Carroll, 2017; Weitzenblum, 2003) (Figure 1.1). The described effects on the RV are the major prognostic factors of PH which is a main outcome of pulmonary chronic hypoxia (McLaughlin et al., 2004). Pulmonary disorders can systemically manifest themselves, particularly in cardiac function. PH, which is itself a manifestation of lung disease is the cause of 10-30% of HF admissions in the USA, highlighting the importance in assessing the effects of non-cardiac diseases on heart function (Han, McLaughlin, Criner, & Martinez, 2007).

1.2 Atherosclerosis

The two main forms of cardiovascular disease that contribute most to mortality rates are MI and stroke, both of which atherosclerosis is the underlying factor. Development of atherosclerosis is a chronic inflammatory process, characterized by arterial stiffening, narrowing and eventual build-up of plaque. The initial formation of atherosclerotic plaque is inherently site-specific to areas of disturbed blood flow (VanderLaan, Reardon, & Getz, 2004). Blood has laminar flow in straight arteries where the endothelium is exposed to high shear stress. In branching and curving areas of the arterial tree, hemodynamic flow is disturbed and causes areas of low shear stress on the endothelium (Caro, 2009). These areas of disturbed blood flow cause endothelial dysfunction by altering the barrier function of the vascular endothelial cells (Chiu JJ & Chien C, 2011). It is at these localized sites that plaque development begins, meaning these are prime sites for plaque detection.

The formation of an atherosclerotic plaque is a long process beginning with platelet aggregation at lesion-prone sites, followed by the inflammatory response. The increased permeability of the dysfunctional endothelium and increased expression of adhesion molecules, allows for the extravasation and accumulation of lipids, immune cells and other circulating plasma molecules (Massberg et al., 2002). Throughout disease progression, accumulated lipids within the intima are taken up by macrophages creating foam cells, which are a hallmark of advancing atherosclerotic lesions. Increased phagocytosis of lipid material causes macrophage apoptosis, which is the basis of formation of a lipid rich necrotic core (LRNC) (Falk, 2006). On top of the LRNC lies a thin-cap fibroatheroma (TCFA). These are two hallmarks of a vulnerable plaque.

1.2.1 Vulnerable plaque

An unstable or vulnerable plaque is the term used for atherosclerotic plaques that are particularly prone to rupture. These are characterized by the macrophage-infiltrated TCFA overlying a large LRNC (Figure 1.2). In comparison, a stable plaque has an intact thick fibrous layer comprised of smooth muscle layers and collagen (Figure 1.2). Calcification is often present in these plaques and a small LRNC (Finn, Nakano, Narula, Kolodgie, & Virmani, 2010). In the past few decades, it has become increasingly clear that detecting plaque composition is as important as detecting the level of stenosis in the vessel. For example, surgical intervention is considered when the carotid artery (CA) has approximately ≥75% stenosis (Naylor et al., 2018). However, symptomatic events have been recorded with ≤ 75% of luminal narrowing as a result of vulnerable plaque rupture. In fact, it is generally suggested that the composition of the plaque is as important in detecting as stenosis level (Shah, 2003). This highlights the importance of detecting vulnerable plaque along with stenosis in patients, in order to prevent major cardiovascular events such as stroke.

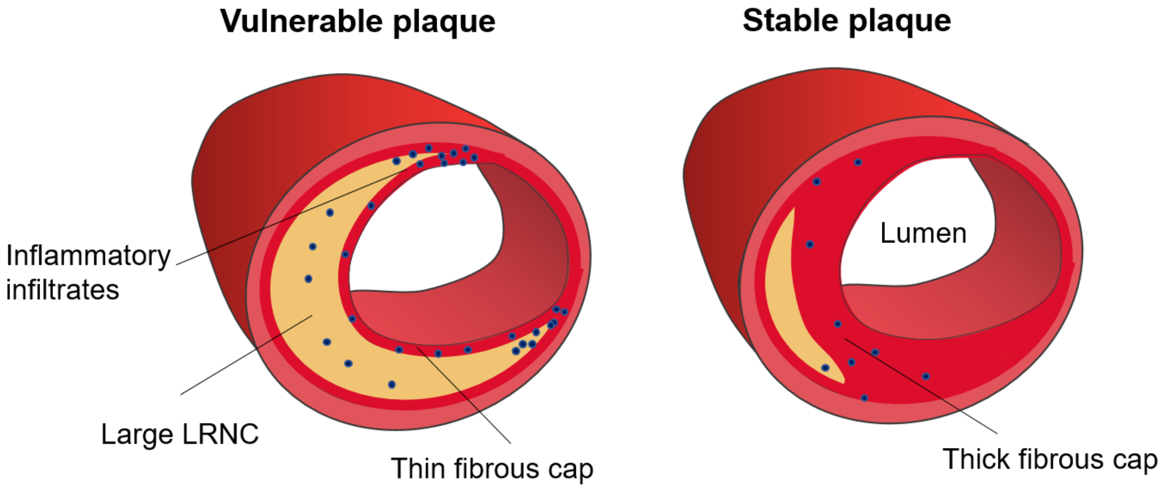

Figure 1.2 Vulnerable vs Stable plaque. Comparison between vulnerable and stable atherosclerotic plaques. Vulnerable plaques are characterized with large lipid rich necrotic core (LRNC), an overlying thin fibrous cap and increased infiltration of inflammatory cells. (LRNC; lipid rich necrotic core).

1.2.2 Stroke

Stroke is one of the primary manifestations of cardiovascular diseases affecting 15 million people annually worldwide with outcomes of paralysis, loss of speech and death (Roth et al., 2017). Stroke is classified as a form of brain injury stemming from a vascular cause, including cerebral ischemia, intracerebral hemorrhage and subarachnoid hemorrhage. This thesis will particularly focus on ischemic stroke. 80% of strokes are induced by ischemia in a region of the brain caused by arterial blockage, where 10-20% of such ischemic strokes are associated with atherosclerotic carotid artery disease (Fairhead & Rothwell, 2005a).

1.2.2.1 The carotid artery

The carotid arteries (CA) are the main blood delivery system to the brain. The carotid bifurcation, which divides the common carotid artery (CCA) into the external and internal carotid arteries (ECA, ICA) is a common and high-risk area for plaque development due to the disturbed blood flow within the bifurcation. The ICA directly supplies blood to the brain while the ECA supplies blood to the facial regions. The CA bifurcation is a crucial area for detection of vulnerable plaques and is one of the primary regions of interest in stroke intervention such as carotid endarterectomy (CEA). The patient selection process for CEA is still under high controversy (Naylor et al., 2018), where guidelines are continuously developed to reduce cases of ‘unnecessary’ surgical interventions. It is therefore important to employ diagnostic tools that are able to characterize plaque composition to reduce avoidable procedures and stroke instances.

1.3 Imaging cardiovascular disease

The complexity and multifactorial nature of CVD demands techniques that can address CVD research questions on a multiscale level. Continuous development of biological and medical imaging technologies has allowed CVD research to progress from *ex vivo* to *in vivo* settings, where complex processes of disease can be visualized in their natural environments, especially with non-invasive technologies. Imaging technologies all hold specific advantages and limitations in imaging CVD. It is therefore important to select the appropriate imaging modality, that offers the best solution for answering a particular CVD question. The decision on choosing an imaging modality is highly based on the specific cardiovascular application. Imaging devices for humans are generally not suitable for imaging mice, therefore specialized devices for pre-clinical or clinical CVD imaging must be carefully assessed.

1.3.1 Preclinical imaging of cardiovascular disease

Imaging modalities used for cardiovascular research in preclinical models must be carefully tailored towards the animal model in question, with this section focusing on murine models in particular. The myocardium and vascular structures are the main targets for imaging cardiovascular biology. Cardiac imaging in mice, particularly the murine heart, is technically challenging due to the small size and fast heart rate (400-600bpm) (Breckenridge, 2013; Phoon & Turnbull, 2016). Several imaging modalities are routinely used for murine heart imaging, including ultrasound (US) and magnetic resonance imaging (MRI). US is based on the transmission of US pulses and the detection of US reflections from tissue structures. It is the most frequently used modality in cardiac research, as it can deal with the spatial and temporal resolution requirements needed for murine heart imaging non-invasively. Variations in anatomical structures such as hypertrophy and dilation can be captured with US. In addition, Colour Doppler US allows for analysis on blood flow direction and velocity. This is useful in detection of turbulent blood flow in the heart or increased rate in blood flow due to hypertrophy-related pressure-overload (Lindsey, Bolli, et al., 2018). However, the majority of murine cardiac US imaging is 2-dimensional and subject to high user-variability, resulting in differences in data interpretation (Phoon & Turnbull, 2016). Recently, advances have been made in cardiac 3D-US imaging, however the temporal resolution necessary for real-time murine heart detection is inadequate (Damen et al., 2017).

MRI is based on the magnetic properties of nuclei within the body and their response to radiofrequency waves and magnetic field gradients. Although MRI is well established in clinical heart imaging, it is still under development for murine heart imaging. The main challenges which face MRI include the small size and fast heartbeat of the murine heart causing motion artefacts and requiring gaiting techniques due to the low temporal resolution (Akki, Gupta, & Weiss, 2013). However, myocardial perfusion, blood flow and anatomy are highly established with preclinical cardiac MRI especially with the use of contrast agents (Lindsey, Bolli, et al., 2018).

1.3.2 Clinical imaging of cardiovascular disease

The diagnosis and appropriate course of intervention in CVD relies on advanced imaging techniques. US, MRI and computer tomography (CT) are the most widely used modalities for imaging vascular and heart diseases. A goal of many CVD imaging devices is to successfully detect arterial stenosis and atherosclerotic plaque, for example in the CA. Intravascular devices such as intravascular US (IVUS) or optical coherence tomography (OCT) are excellent modalities in detecting stenosis (IVUS) or characterizing plaque composition (OCT) (Yoshimura et al., 2012) (Figure 1.3), however intravascular devices are inherently invasive and require surgical procedures, making non-invasive imaging devices much more attractive.

1.3.2.1 Clinical imaging of the carotid artery

Clinical imaging of the CA has historically been directed towards measuring the stenosis level of the CA which is used to guide clinicians in their surgical intervention decisions. However, with the increasing realization that detecting plaque composition and hence assessing plaque vulnerability is crucial in stratifying the risk of stroke; there is a need for non-invasive carotid imaging modalities that can successfully accomplish this. US and Color Doppler US (Figure 1.3) is the gold standard for screening patients due to its real-time imaging capabilities, patient bed-side location, non-ionizing radiation and relative low-cost (Dave et al., 2018). Although US is excellent in measuring stenosis, it is yet to be advanced in characterizing plaque composition. The lipid or calcified content can be estimated by assessing the echogenicity of the plaque, however these estimations are often faced with high inter-user variability (Nyman, Lindqvist, Näslund, & Grönlund, 2018). Clinical MRI on the other hand is most often used as a secondary diagnostic measure after initial US screening, as it offers high accuracy, high spatial resolution and also provides insight into plaque characteristics such as presence of intraplaque hemorrhage and LRNC (Figure 1.3). However, the major pitfall of MRI is its high cost and time constraints, preventing its establishment as a standard screening method in the clinics (Brinjikji et al., 2016).

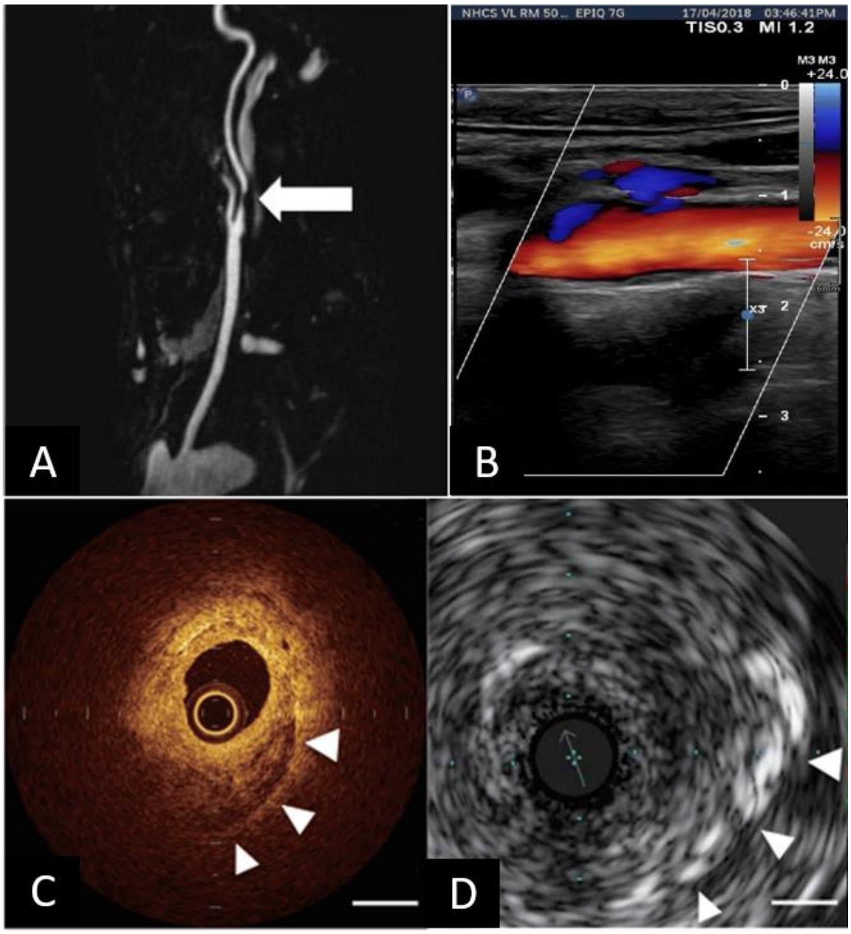

Figure 1.3 Non-invasive and intravascular clinical carotid artery imaging devices. (A) Contrast enhanced MR-angiography (MRA), where the white arrow indicates occlusion. (B) Color Doppler US superimposed over US image indicating change in blood flow velocities. (C) OCT intravascular image of calcified areas of plaque (white arrows) (D) Corresponding IVUS image to (c) also showing calcified areas of plaque in CA (white arrows). (MRA: magnetic resonance angiography, US: ultrasound, OCT: optical coherence tomography, CA: carotid artery, IVUS: intravascular ultrasound) *Figure 1.3 A-B Adapted from Saxena, A. et al 2019. Terms of Use: Images are licensed under a Creative Commons Attribution-NonCommercial-ShareAlike United States License 4.0.* http://creativecommons.org/licenses/by/4.0/. *Figure 1.3 C-D adapted from Yoshimura et al. 2012*

1.3.3 From preclinical to clinical imaging

The difficulty in finding solutions for many CVDs is the translation from pre-clinical studies to clinical studies (Wilson, Jermyn, & Leblond, 2018). Murine models are fundamental for basic research and for exploration of biological questions that can be translated into clinical applications (Koo, Hamilton, & Williamson, 2006). However, mice and humans are inherently different and translation of results from preclinical studies must be strictly regulated. Clinical studies are also invaluable, as they are carried out in the target model, humans. In particular for CVD, many risk factors that influence the disease, which often stem from human behavior have a large impact on CVD outcome and are difficult to implement into animal models.

1.4 Optoacoustic Imaging

The optoacoustic (OA) effect was discovered in 1880 by Alexander Graham Bell, where it was found that light can generate sound (Bell, 1880). Following advances in laser technologies, the OA effect began to be utilized in biomedical imaging research. OA imaging is based on the excitation of acoustic waves by irradiating tissue with pulsed laser light at certain wavelengths. Biological tissues contain a variety of chromophores (light-absorbing molecules) that have wavelength-dependent absorption coefficients. The absorption of light by the chromophore causes a small pressure increase followed by relaxation, which results in the emission of detectable acoustic waves (Figure 1.4A). OA imaging is generally split into two broad areas, OA microscopy and OA tomography (OAT). For imaging cardiovascular dynamics such as the murine heart or cardiovascular structures of large depths such as the human carotid artery, OAT is the most the suitable technique, due to its superior penetration depth and imaging speed (X. L. Deán-Ben, Gottschalk, Mc Larney, Shoham, & Razansky, 2017),

Unlike common optical imaging modalities, OAT is inherently insensitive to scattering of light by tissue and can therefore achieve depth penetration in the millimeter to centimeter ranges (Ntziachristos & Razansky, 2010). The obtained OA signal, and thus formed OA image, mostly depends on the target tissue properties, particularly the optical absorption coefficient. The OA image contrast arises from the amount of light absorbed by local chromophores rather than changes in the acoustic impedance (Beard, 2011). This is particularly powerful in biomedical imaging due to the vast variety of available endogenous chromophores including hemoglobin, lipids, water and collagen (Figure 1.4 B). The pulsed laser light employed in OAT is non-ionizing and has no toxic effect on tissue. The non-invasive nature of OAT along with the optically derived endogenous contrast and US imaging depths makes it a highly attractive system for preclinical and clinical imaging.

1.4.1 Cardiovascular optoacoustic imaging

OAT is particularly well suited to cardiovascular imaging due to differing absorption coefficients of deoxygenated haemoglobin (Hb) and oxygenated haemoglobin (HbO), allowing for *in vivo* discrimination of oxygenation levels in the intact vasculature system. Due to the strong optical absorbance of hemoglobin, a vast portion of biomedical research in OA imaging targets microvasculature dynamics, for example, neovascularization of tumors (Ron, Deán-Ben, Gottschalk, & Razansky, 2019) or hemodynamic changes in the brain in response to stimuli (Gottschalk et al., 2019). However, applying OAT for direct cardiovascular imaging applications, such as the murine heart or the carotid artery, has its own specific challenges.

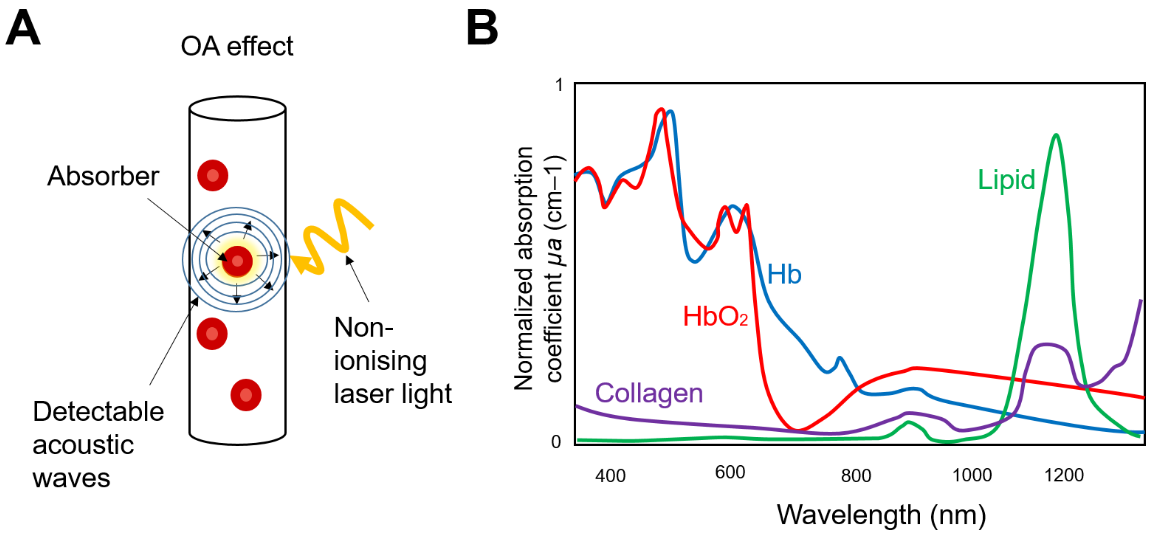

Figure 1.4 Optoacoustic effect and optical absorption coefficients. (A) Schematic of the optoacoustic effect, where light is absorbed by chromophores causing thermal expansion which emits acoustic waves. (B) Absorption spectra of biological tissue. (OA; optoacoustic, HbO_2; oxygenated haemoglobin, Hb; deoxygenated haemoglobin)

Cardiovascular OAT is typically carried out in the near-infrared (NIR) optical window, which ranges between 660-1300nm (Beard, 2011). Imaging using NIR wavelengths, as opposed to imaging in the visible range (380-730nm), allows for deeper penetration of light into the tissue, which is required to image deeper structures. Several clinically relevant chromophores for cardiovascular biology, such as Hb, HBO and lipids, have their peak absorption within the NIR window.

The cardiovascular system is dynamic under the influence of the beating heart, hence requiring a system with enough temporal resolution that can capture real-time information. However, the fundamental parameters required for cardiovascular imaging are not a case of 'one-size fits all'. Cardiovascular OAT requirements for murine models vary considerably compared to imaging humans. It is thus important to understand the technical adaptations required in OAT to obtain optimal pre-clinical and clinical images.

1.4.1.1 Pre-clinical cardiovascular optoacoustic imaging

OAT has been implemented in a number of preclinical mouse studies for cardiovascular applications. Yet, the small size and rapid heartbeat of the mouse is a challenge in OAT. Examples of cardiovascular OAT studies have included imaging of the abdominal and thoracic aortas in atherosclerotic ApoE-/- murine models, whereby gold nanoprobes were used to target specific characteristics of vulnerable plaques (Rouleau et al., 2013; C. Wu, Zhang, Li, Li, & Wang, 2016). However, studies were limited to *ex vivo* imaging analysis or cross-sectional 2D images that could only capture a small portion of the abdominal aorta.

Imaging of the intact murine heart has been achieved with OAT, initially captured with multispectral optoacoustic tomography (MSOT) with 2D cross-sectional views, targeting sites of myocardial infarction using the P and L selectin targeting probes at 10Hz frame rates (Taruttis et al., 2013). However, 10Hz imaging of the murine heart results in loss of information as it is an insufficient temporal resolution. Volumetric real-time OA imaging of the murine heart has since been achieved with a frame rate of 50Hz (Xosé Luís Deán-Ben, Ford, & Razansky, 2015). Functional parameters were extracted by beat to beat analysis, such as the pulmonary transit time (PTT), which is the time taken for blood to pass through the pulmonary circuit by measuring the time the blood is ejected from the RV and returned to the LV. In order to track blood flow, indocyanine green (ICG) was injected intravenously which binds to the serum blood protein, albumin, and can thus be tracked through the entire cycle of a single heartbeat. ICG is inherently a fluorescent NIR dye, with peak optical absorption at 800nm and is therefore an optimal contrast agent for imaging blood flow dynamics with OA, while still obtaining endogenous contrast for anatomical information. The PTT was further assessed by Lin *et al*, using the permanent occlusion surgical MI model (Lin et al., 2017). PTT values were assessed at different stages post MI, using 50Hz frame rate and ICG intravenous injection. A decrease in PTT values was detected for the longer time points (21 days vs 3 days) post MI. The obtained PTT values had a positive correlation with infarct size (Figure 1.5 A). In addition, the PTT values were corroborated with LV ejection fraction (LVEF) values obtained with MRI, where PTT and LVEF had an inverse correlation (Figure 1.5 B) meaning that the lower the PTT values the higher the LVEF, which is indicative of increased LV function (Lin et al., 2017).

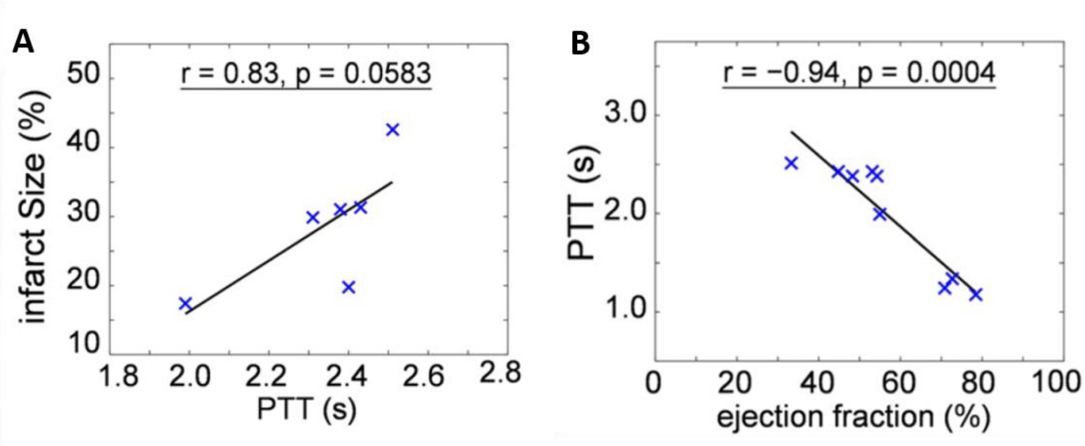

Figure 1.5 Pulmonary transit time (PTT) (A) PTT plotted against infarct size (extracted from histological measurements), showing a positive correlation. (B) PTT plotted against ejection fraction (measured from MRI) showing an inverse correlation. (PTT, pulmonary transit time; MRI; magnetic resonance imaging) *Adapted with permission from Lin et al. (2017).*

1.4.1.2 Clinical cardiovascular optoacoustic imaging

In recent years, OAT has begun to transition from pre-clinical animal research towards a focus on clinical applications. For this to successfully occur, the OAT system must include technical parameters that are geared towards human imaging. OAT has been implemented successfully in the clinics for several applications including detection of Crohn’s disease (Knieling, 2017), dermatological pathologies (Chuah et al., 2019) and breast cancer detection (Heijblom et al., 2016; Oraevsky et al., 2018). It has also been demonstrated in studies primarily focusing on atherosclerosis detection. Vulnerable plaques have been detected in rabbit models of CAD with OA intravascular devices (B. Wang et al., 2012) and several *ex vivo* studies on human samples have also demonstrated vulnerable plaque detection by utilizing the peak optical absorption of lipids at 1200nm (Allen, Hall, Dhillon, Owen, & Beard, 2012; Kruizinga et al., 2014) and matrix metalloproteinase activity in vulnerable plaques in *ex vivo* CAs (Razansky et al., 2012). However, these studies are limited in proper clinical translation due to the invasive nature of intravascular methods and *ex vivo* limitations. Non-invasive OAT attempts have been shown in peripheral arteries of the foot in healthy volunteers, showing clear detection between veins and arteries and their real-time pulsing motion (Taruttis et al., 2016). In addition, imaging of the CA in a healthy volunteer has been shown with OAT (Dima & Ntziachristos, 2012), however limited to 2D cross-sectional views. There has been a large focus recently on detecting the CA with OAT as it is an attractive region of interest (ROI), laying relatively superficial below the skin with depths of mm-cm range. More importantly, the CA is clinically attractive due to the tendency of plaque development around the bifurcation site, which could subsequently lead to stroke.

1.4.2 Optoacoustic imaging setup

There are numerous OAT setups, usually geared towards a specific application of interest. Figure 1.6 illustrates a schematic of a general OAT setup. Initial OAT setups only provided 2D cross-sectional images, similar to conventional US imaging. However cross-sectional imaging of complex biological tissue structures is challenging, since one can only visualize a single 2D plane at a time and acquisition of larger volumes rather than a single slice decreases temporal resolution considerably (X. L. Deán-Ben et al., 2017). Volumetric or 3D OAT addresses this limitation. In particular, the development of 4D-OAT[2] enables imaging of large volumes, such as whole murine hearts and brains, within a single frame

---

[2] 3D in combination with real-time imaging.

and little scanning time (Xosé Luís Deán-Ben et al., 2015; Gottschalk, Fehm, Deán-Ben, Tsytsarev, & Razansky, 2016). Although the introduction of 3D and 4D OAT has allowed for a large increase in variety of applications to be explored with OA, the design and development of 3D probes and their associated instrumentation must still be carefully tailored towards preclinical or clinical applications. In order to achieve this, careful coordination and design of the OA imaging set up is necessary to establish a successful and functional multidisciplinary OAT setup.

1.4.2.1 Ultrasound transducer requirements

The US transducer used in every OAT system detects the acoustic wave generated by the OA effect. It is usually composed of piezoelectric elements forming the active surface of the transducer, which detect pressure changes and convert them to an electrical signal. A high number of elements increases imaging sensitivity, however detection sensitivity scales with element size, therefore element numbers and size need to be carefully selected (Beard, 2011).

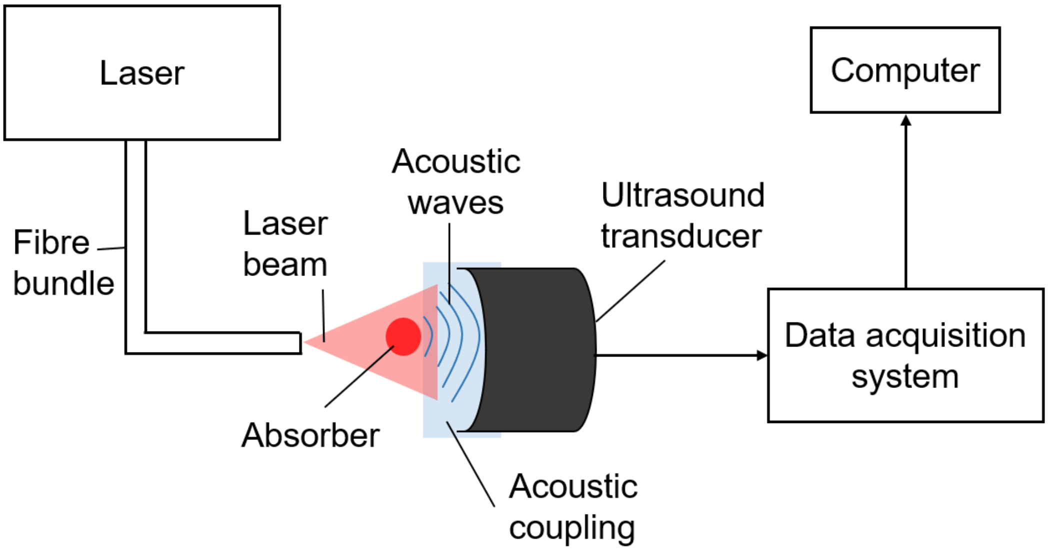

Figure 1.6 Schematic of OAT imaging setup.

3D image acquisition is dependent on the shape of the transducer. Curved linear arrays are common in OAT setups, they however are limited to cross-sectional 2D imaging. 3D images can be obtained by the transformation of the transducer surface array from a linear to hemi-spherical shape (Schellenberg

& Hunt, 2018; Upputuri & Pramanik, 2016). The tightly packed elements arranged on the spherical surface detect OA signals from multiple positions and angles around a central focal point, thus forming a volumetric image (X. Luís Deán-Ben & Razansky, 2013).

A single hemispherical transducer design cannot be ideal for a variety of applications, especially when balancing the requirements of pre-clinical and clinical cardiovascular imaging. Mice and humans possess very different size scales and differences in their physiologies. It is possible to obtain an OA image of the whole murine heart or brain in a single frame with a fixed transducer (X. L. Deán-Ben et al., 2017), while in humans the same transducer would most likely not be able to capture an entire organ and would benefit more with a handheld approach. In order to account for differences between mice and humans, the transducer geometry is crucial. By changing the diameter of the transducer or the radial distance between the transducer and the center of the sphere (central focal point), which in turn effects the angular coverage of the transducer of the ROI, a variety of imaging parameters can be achieved. For pre-clinical imaging of the murine heart, employing a hemispherical transducer of a size that can hold the mouse on top would be ideal. Therefore, the angular coverage should be high with sufficient penetration depth to capture the heart. However, this particular geometry would be suboptimal for human imaging. To successfully image humans with OAT, a hand-held and easy-to-maneuver device would maximize coverage across the body, therefore transducer size should be minimized. The transducer must also possess mm-cm scale imaging depths to account for anatomical variations and deep structures, such as the CA.

Another parameter that must be addressed in transducer design and optimization is the acoustic coupling. For murine heart imaging the transducer is stationary and therefore containing the coupling medium is simple. However, for clinical imaging, containing the coupling medium is important for two reasons: 1) It must be fully contained due to the handheld nature of the transducer and 2) the holder itself must be suitable for imaging humans, i.e. a design that can easily and safely move across the skin. In addition to containing the coupling medium, a holder must be designed so that the focal center of the transducer is still targeting the ROI.

1.4.2.2 Laser requirements

Light delivery to the target tissue is essential in OAT and like transducer design, laser requirements vary across different applications. The typical laser used in OAT employs short nanosecond laser pulses tunable between visible and NIR wavelengths, typically achieved with optical parametric oscillators (OPOs). In addition, the per pulse energy is critical for OAT in order to image at mm-cm depths. Nanosecond pulses with energies between 5-100 mJ are required to penetrate tissue and generate sufficient OA signal. The safety recommendations dictated by the ANSI limits are used as a guideline for maximum energy allowed per square centimeter of imaged tissue (ANSI, 2007). Another important laser parameter is the repetition rate of the laser, i.e. laser shots per second, which can range between few hertz and several kilohertz. Ideally, a single laser source would be used which can provide all the required parameters. However, such a laser would be very complex, large and costly (Stylogiannis et al., 2018). Therefore, different lasers are usually assigned to specific application needs. For example, imaging fast processes such as the heartbeat or brain activity in mice requires high temporal resolutions to account for the rapid biological processes and obtain meaningful data. On the other hand, when imaging at a human scale, such as the CA, the pulsing motion of the artery is at a much slower rhythm than the murine heart, hence temporal resolution requirements are not as demanding. However, the structure of the CA requires deeper light penetration to be detected, which is achieved by imaging at higher per-pulse energies and thus requiring a laser capable of 10-100 mJ per pulse. Particularly for CA OAT, a tunable laser switchable between 800-1200nm would allow for CA detection and lipid detection at 1200nm if imaging atherosclerotic patients.

Another important consideration in the OAT setup is light delivery from the laser to the tissue. Several approaches have been used in a variety of OAT setups (Schellenberg & Hunt, 2018; Xia & Wang, 2014). For example, the light delivery bundle or fiber bundle, could be placed separately from the transducer so that light is directed on one side and OA signal detected from the other side (or nearby) by the transducer. Another effective method is the combination of transducer and fiber bundle in the same location, so that light delivery and signal detection are simultaneous. In OAT, a fiber bundle usually consists of multiple single fibers tightly packed into a bundle, therefore maximizing light delivery. A single fiber bundle is often used, however multiple fiber bundles can be used to maximize the illuminated area of the ROI, allowing for increased permissible per-pulse energies and hence better imaging depth, effective field of view and signal to noise ratio (Schellenberg & Hunt, 2018; Xia & Wang, 2014)

1.4.2.3 Image acquisition and processing

The OA effect combines two physical processes; acoustics and optics, both of which have to be accounted for when acquiring the OA image. The two most frequently used algorithms for OAT reconstruction include filtered back-projection (BP) and model-based (MB). MB offers a more accurate reconstruction, however compared to BP is highly computationally expensive(X. Luís Deán-Ben, Ma, Razansky, & Ntziachristos, 2011; K. Wang et al., 2013). Biological tissue is heterogeneous causing variability in its acoustic properties. Accurate estimation of tissue acoustic properties, such as speed of sound, which varies between 1400-1600m/s, can have a large improvement on image quality (Lutzweiler & Razansky, 2013). Another reconstruction challenge are limited view artefacts, which are obtained from incomplete signal detection of the ROI, especially in hemispherical OAT transducers as the elements do not completely surround the object (Yao & Jiang, 2011). However, several approaches have been developed to improve limited view artefacts, recently including deep learning methods (Davoudi, Deán-Ben, & Razansky, 2019; Yao & Jiang, 2011).

The optical properties must also be accounted for in OA image processing. The OA signal is a product of the optical absorption coefficient and light fluence; the amount of light at a given volume. OA contrast arises from the amount of absorbed light of the tissue chromophore and as light penetration in tissue is limited due to scattering of photons, the deeper the ROI the less OA signal is detected. However, the obtained OA signal corresponds to the tissue chemical composition thus providing accurate information of the molecular composition of the tissue. Imaging at different wavelengths, i.e. multispectral imaging allows the composition of the tissue to be differentiated into specific molecular components, while estimating the concentration of the molecule within the imaged region (Lutzweiler & Razansky, 2013; H. F. Zhang, Maslov, & Wang, 2008).

1.5 Aims of the thesis

To gain further insights into CVD, advanced cardiac imaging tools are needed to investigate rapid cardiovascular dynamics, *in vivo* and non-invasively. The murine heart and the human carotid artery are fundamentally different. The murine heart is small, superficial from the skin surface and has a rapid heartbeat, which requires an extremely high temporal resolution to capture in real-time. The anatomy of the human carotid artery varies considerably among individuals, especially the depth and the diameter. In order to capture the carotid bifurcation and account for the anatomical variations, it is essential to have high-energy lasers for deeper penetration of light and a scannable probe in order to locate the ROI. To address the differences in imaging requirements, the thesis aims to explore and optimise technical imaging parameters for implementation of OAT for the following cardiovascular applications:

Aim 1: Ultra-fast volumetric optoacoustic tomography for monitoring of post-ischemic myocardial remodelling of murine models of myocardial infarction. (Chapter 2)

Aim 2: Volumetric optoacoustic tomography of impaired heart function under hypoxic conditions. (Chapter 3)

Aim 3: Volumetric optoacoustic tomography of the human carotid artery visualised in a multispectral, non-invasively and in a real-time manner. (Chapter 4)

2. Volumetric optoacoustic tomography differentiates myocardial remodelling

Submitted in *Molecular Imaging and Biology (under review)*

Authors

Ivana Ivankovic[1,2], Xosé Luís Déan-Ben[1,2], Helena Haas[3], Melanie A. Kimm[3], Moritz Wildgruber[3,4], and Daniel Razansky[1,2]

[1]Faculty of Medicine and Institute of Pharmacology and Toxicology, University of Zurich, Switzerland

[2]Institute for Biomedical Engineering and Department of Information Technology and Electrical Engineering, ETH Zurich, Switzerland

[3]Department of Diagnostic and Interventional Radiology, Faculty of Medicine, Klinikum Rechts der Isar Technical University of Munich, Germany;

[4]Translational Research Imaging Center, Department of Clinical Radiology, Universität Klinikum Münster, Germany.

No conflict of interest disclosed

2.1 Abstract

Myocardial healing following myocardial infarction (MI) is a complex process that is yet to be fully understood. Clinical attempts in regeneration of the injured myocardium using cardiac stem cells faced major challenges, calling for a better understanding of the processes involved at a more basic level in order to foster translation. We examined the feasibility of volumetric optoacoustic tomography (VOT) in studying healing of the myocardium in different models of MI, including permanent occlusion (PO) of the left coronary artery, temporary occlusion (ischemia-reperfusion - I/R), as well as infarcted c-kit mutants, a genetic mouse model with impaired cardiac healing. Murine hearts were imaged at 100Hz frame rate using 800nm excitation wavelength, corresponding to the peak absorption of indocyanine green (ICG) in plasma and the isobestic point of haemoglobin. The non-invasive real-time volumetric imaging capabilities of VOT have allowed the detection of significant variations in the pulmonary transit time (PTT), a parameter affected by MI, across different murine models. Upon intravenous injection of ICG, we were able to track alterations in cardiac perfusion in I/R models, which were absent in wild-type (*wt*) PO or $kit^{W}/kit^{W\text{-}v}$ PO mice. The *wt*-PO and I/R models further exhibited irregularities in their cardiac cycles. Clear differences in the PTT, ICG perfusion and cardiac cycle patterns were identified between the different models and days post MI. Overall, the results highlight the unique capacity of VOT for multi-parametric characterization of morphological and functional changes in murine models of MI.

2.2 Introduction

Ischemia of the myocardium is the most common type of myocardial injury characterised by a prolonged period of reduced blood flow to the heart muscle (Tanai & Frantz, 2011). Ischemic damage of the heart induces a process of cardiac remodelling, by which extensive morphological, histological and molecular changes occur both within the necrotic and healthy myocardium (St. John Sutton & Sharpe, 2000). Until recently, the mammalian heart was assumed to lack regeneration capabilities due to the incapacity in of cardiomyocytes to proliferate (Kazu & Poss, 2012). Recent studies have shown that resident cardiac stem cells positive for the stem cell factor c-kit, possess regenerative properties and can promote the healing response of the myocardium following myocardial infarction (MI) (Urbanek et al., 2005). These observations have fostered preclinical research and clinical studies on stem cell therapies for post-infarct myocardial healing (Behfar, Crespo-Diaz, Terzic, & Gersh, 2014; Bergmann et al., 2009; Madigan & Atoui, 2018). However, while initial clinical trials yielded promising results, these were not substantiated by larger trials involving different types of cell therapies. This called for a better understanding of the fundamental processes involved in cardiac healing post MI and how pluripotent cells effect the healing response. Efforts are therefore being redirected towards improving the preclinical settings in terms of MI models and providing methodological advances to enable more effective *in vivo* observations (Tompkins et al., 2018).

Arguably, longitudinal *in vivo* imaging represents the most promising approach for assessing dynamic changes in morphology, function and molecular biology during the healing phase post MI. The existing technologies, such as positron emission tomography and magnetic resonance imaging (MRI) (Yu, Qian, Chen, Dodd, & Koretsky, 2014), lack key performance metrics required for imaging rapid dynamics in the whole mouse heart, and only regular heartbeat can be observed via prospective or retrospective gaiting (Lindsey, Kassiri, Virag, Castro Bras, & Scherrer-Crosbie, 2018). Ultrasound (US) provides a cost-effective and non-invasive approach for imaging of the murine heart in real time. US has been shown to be capable of resolving anatomical changes in response to MI. However, standard 2D cross-sectional US images are prone to artefacts related to cardiac motion and inter-user variability. (Provost et al., 2014). While there has been significant development in increasing temporal resolution of 3D US, gaiting techniques are still required for murine cardiac imaging (Damen et al., 2017).

Recently, volumetric optoacoustic tomography (VOT) has been suggested as a novel imaging tool for *in vivo* murine heart analysis capable of capturing the entire 3D volume of the beating mouse heart non-invasively and in real-time (Xosé Luís Deán-Ben et al., 2015; Lin et al., 2017). Beat-to-beat analysis of healthy and infarcted murine heart models enabling quantification of functional parameters, such as the pulmonary transit time (PTT), defined as the time it takes for blood to pass through the pulmonary circuit connecting the two ventricles (Ivankovic et al., 2019; Lin et al., 2017). The PTT is estimated by tracking the bolus of a blood pool dye (indocyanine green – ICG) following intravenous (IV) injection (Xosé Luís Deán-Ben et al., 2015). The PTT was found to increase in MI models while an inverse relationship between PTT and time post MI surgery was further observed. (Lin et al., 2017). Herein, we employed VOT for assessing myocardial function *in vivo* in different MI models, in order to assess the feasibility of VOT to detect functional changes of the myocardium across different murine models of MI. We hypothesize that VOT is able to capture distinct differences in myocardial function post MI induced via permanent occlusion (PO) or ischemia-reperfusion (I/R) as well as infarcted c-kit deficient ($kit^{W}/kit^{W\text{-}v}$) mice, a genetic mouse model with impaired cardiac healing which has been frequently used to study the effects of pluripotent stem cells on the healing of the myocardium (Marino et al., 2019).

2.3 Materials and methods

2.3.1 Acute murine MI models: permanent occlusion, reperfusion, c-kit deficiency

All animal procedures and their care were conducted in conformity with national and international guidelines (EU 2010/63) with approval from the local authority (Government of Upper Bavaria) and supervised by the Animal Care and Use Committee of Klinikum Rechts der Isar, Munich and the Helmholtz Center Munich. Animals were housed in standard animal rooms (12 h light/dark cycle, 50-60% humidity, 18-23°C temperature, bedding material) in individually ventilated cage systems (IVS Techniplast) under specific pathogen-free conditions with free access to water and standard laboratory chow ad libitum. Female wild-type albino C57Bl/6J mice (*wt*) (n = 26) and WBB6F1-KitW/KitW–v mice ($kit^{W}/kit^{W\text{-}v}$) (n=13) aged 12-14 weeks were used as MI models (Figure. 2.1A). All mice were intubated and mechanically ventilated for MI surgery after removal of hair from their chest. The intervention was performed by a veterinarian experienced in small animal surgeries. The rib cage was exposed between the 4th and 5th rib. MI induction was based on ligation of the left anterior descending coronary artery (LAD) (Wildgruber et al., 2014). In the *wt* -PO model (n=13), MI induction involved consistent closure of the LAD using 8 sutures (Figure 2.1A, left panel). The *wt*-I/R model (n=8) involved temporary occlusion of the LAD for approximately 30 minutes followed by reperfusion (Figure. 2.1A, middle panel). $kit^{W}/kit^{W\text{-}v}$ mice lack the tyrosine receptor kinase c-kit, which is essential for proliferation, survival and migration of cardiac stem cells (Di Siena et al., 2016). MI was induced via PO in $kit^{W}/kit^{W\text{-}v}$ models ($kit^{W}/kit^{W\text{-}v}$ PO) (n = 13) (Figure 2.1A, right panel). In all MI models, the rib cage was bound with three stiches and the skin was subsequently closed with transparent surgical glue. Control or non-infarct mice for *wt* models (n=9) and $kit^{W}/kit^{W\text{-}v}$ (n=5) underwent no surgery. VOT imaging was as performed at 3 (3d), 10 (10d) and 21 (21d) days post-surgery (MI) for *wt*-PO (3d, n=3; 10d, n=6, 21d, n=4) and $kit^{W}/kit^{W\text{-}v}$ PO (3d, n=4; 10d, n =5; 21d, n=3) models, while I/R injury was assessed at 3 and 21 days post-surgery (3d, n=3; 21d, n=5).

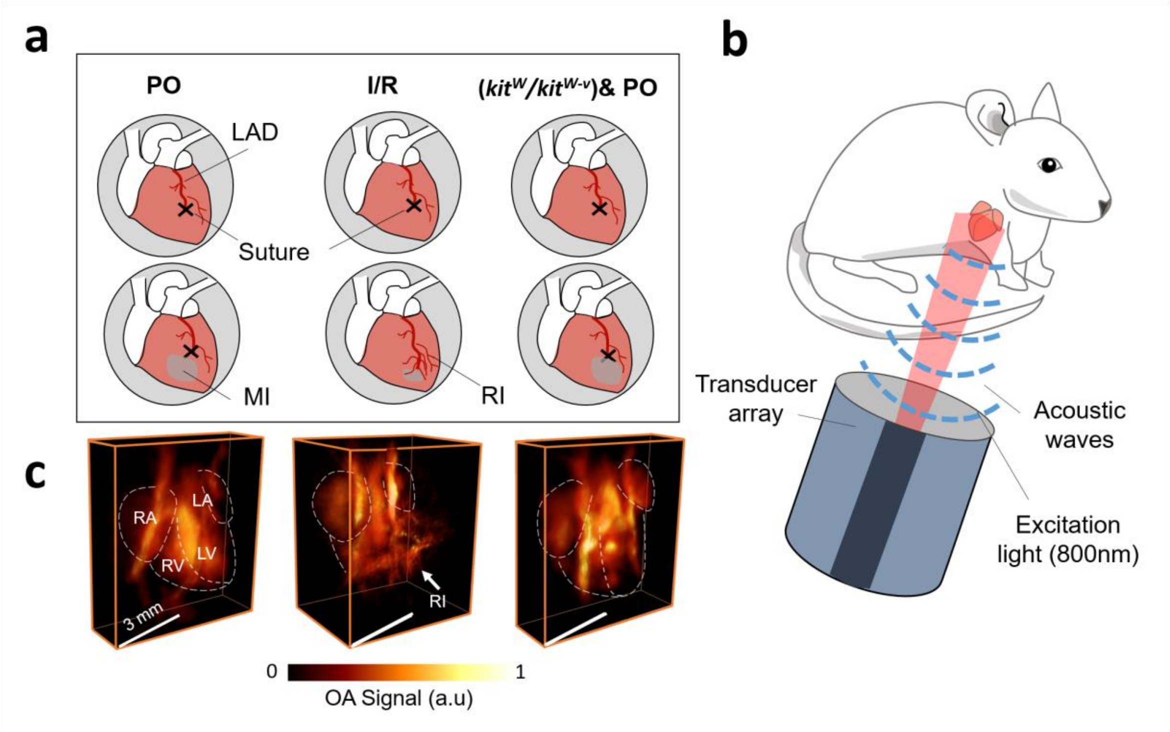

Figure 2.1: Schematic of experimental procedure. (a) Procedure of MI induction for varying models with surgical technique and MI outcome. The black cross indicates the suture, the grey shading on left ventricle indicates infarct area and 30 minutes indicates length of occlusion of LAD (MI; myocardial infarction, LADAD; left anterioranterior descending artery, PO; permanent occlusion, I/R; ischemic reperfusion, RI; reperfusion injury) (b) Simplified diagram of ultrasound transducer with fibre output for light delivery to murine heart and curved array for detection of optoacoustic signals. (c) 3D rendered volumes of optoacoustic images of murine hearts corresponding to PO (left), I/R (middle) and *kit*^{W}/*kit*$^{W-v}$

2.3.2 VOT imaging setup

A detailed description of the VOT imaging set-up is provided elsewhere (Lin et al., 2017). In short, the imaging system consists of a 512-element hemispherical array transducer (custom-made Imasonic SaS, Voray, France) with a central US frequency of 5 MHz and ~100% detection bandwidth (Figure 2.1B). The VOT images rendered with this array have an almost isotropic resolution of 150 µm within an effective field of view (FOV) of approximately 10x10x10 mm^3. OA signal excitation was achieved by illuminating the mice with a tuneable (700-900 nm) pulsed (<10 ns) near-infrared laser (Innolas Laser GmbH, Krailing, Germany) via an optical fibre bundle (Ceram Optec GmbH, Bonn Germany) through a central cavity in the transducer array. In the experiments, the wavelength was tuned to 800 nm (peak absorption of ICG in plasma) and the laser was operated at 100 Hz with maximum per-pulse energy of 20 mJ. All 512 OA signals detected by the array elements were simultaneously sampled at 40 Megasamples per second by a custom-made data acquisition system (Falkenstein Mikrosysteme GmbH, Taufkirchen, Germany). 3D volumes of 12x12x12 mm^3 (120x120x120voxels) were reconstructed for each laser pulse using the filtered back projection algorithm (Dean-Ben, Ozbek, & Razansky, 2013) without employing signal averaging (Figure 2.1C). For this, the raw signals were band-pass filtered between 0.1-7 MHz and deconvolved with the impulse response of the transducer elements. For better visualization, a median filter with kernel size 3x3x3 was applied to the reconstructed images. The graphics processing unit (GPU) implementation of the algorithm further enabled real-time preview during the experiments. All processing steps and analyses were performed in Matlab (version 9.1, R106; MathWorks) and Amira (Zuse Institute, Berlin, Germany) was used for image visualization.

2.3.3 In vivo imaging procedures

For imaging with the VOT imaging set-up, mice were anesthetised with a 2% isoflurane-medical air mixture (0.8 l/min gas flow). Hair on the chest surrounding the imaged heart region was shaved to minimise image artefacts associated to light and sound attenuation. Mice were then placed in prone position on top of a solid agar block (1.3% w/v) filling the volume enclosed by the spherical array pointing upwards. Optimal acoustic coupling for ultrasound transmission was further guaranteed by adding a layer of ultrasound gel between the agar and the skin. The mouse heart was placed into the centre of field of view with the help of real-time image preview (Dean-Ben et al., 2013). Subsequently, IV injection of 100 nmol indocyanine green (ICG, Profiplus Bvba, Korstessem, Belgium) diluted in 50 µl of saline solution was performed and the PTT was measured by tracking the ICG bolus perfusion through the heart with VOT (Xosé Luís Deán-Ben et al., 2015). A total of 5000 volumetric image frames were acquired over 50 sec at a wavelength of 800 nm (peak absorbance of ICG) with the injection performed 15 sec after beginning the acquisition. Mice were reinjected with the same ICG concentration 10 minutes after the first acquisition. Imaging of each mouse lasted for about 30 minutes. The physiological parameters of the animal were constantly monitored throughout the experiments (PhysioSuite, Kent Scientific, Torrington, Connecticut).

2.3.4 PTT in response to varying MI models

The PTT was measured for all models and compared between the different groups. The automated method to extract the PTT has been described previously (Lin et al., 2017). In short, tracking the ICG bolus perfusing through the heart was done by tracking the OA signal intensity variations at different points. The PTT was estimated as the difference between the time points corresponding to maximum signal intensities at the right and left ventricles. The value obtained (in seconds) corresponds to the time it takes for the ICG bolus (blood) to complete the pulmonary circuit. All PTT values for each MI model (*wt* and $kit^{W}/kit^{W\text{-}v}$) were initially compared to non-infarct mice (*wt* and $kit^{W}/kit^{W\text{-}v}$) and then plotted on different days post infarct in order to identify presence of a positive myocardium remodelling.

2.3.5 In vivo analysis of reperfusion injury

Analysis of reperfusion injury in *wt*-I/R models was carried out post image reconstruction. Areas located in the region where the LAD was temporary occluded were thoroughly analysed in the VOT images for suspected damage. The hearts of *wt*-I/R models were compared to *wt*-PO models and non-infarcted mice to identify presence of the reperfusion injury, which should be absent in the surgical PO and non-infarcted mice. Perfusion of ICG through the heart and its interaction with the suspected reperfusion injury was further assessed on a beat-to-beat basis for both I/R and PO models. Endothelial dysfunction is a known outcome of reperfusion injury, where the vasculature in the injured area may become leaky. Therefore, the dynamics of the OA signal intensity was measured at the different stages of ICG perfusion to examine whether albumin-bound ICG extravasates due to increased vascular permeability at sites of reperfusion injury.

For validation of increased microvascular permeability for ICG, cryosections containing IV injected ICG obtained 24 hours after I/R, were further stained for CD31 (ab28364, Abcam) and detected with an Alexa 647-coupled secondary antibody (Jackson 111-605-144). Mounting media containing DAPI (Thermo Scientific) was used for tissue embedding and visualization of the cell nuclei. All slices were imaged using an Eclipse 50i microscope (Nikon) and NIS-Elements BS 3.22 software (Nikon).

Cryosections were H&E stained according to standard protocols and imaged using an Axio Imager M2 microscope (Carl Zeiss) equipped with Zeiss Zen pro 2.0 software (Carl Zeiss).

2.3.6 Cardiac cycle characterization

The high temporal resolution of the VOT system enabled analysis of heart activity on a beat-to-beat basis. Irregularities within the cardiac cycle were detected using the interactive viewer View4D (Matlab), where the cardiac cycle could be clearly visualised in the OA signal intensity time profiles. The cardiac cycles in the recorded 5000 volumetric image frames were analysed for all models and time points post MI.

2.3.7 Statistical Analysis

Statistical analysis was carried out on measurements taken from *wt*-PO, *wt*-I/R and *kit*^{W}/*kit*$^{W-v}$ PO and non-infarct models. Boxplots of PTT values were plotted for all MI models and non-infarct models and subsequently compared with each other with a one-way analysis of variance (ANOVA). ANOVA was carried out for assessing differences in heart regeneration of the different models at time points (3, 10 and 21 days) post MI followed by Tukey’s post hoc test for multiple comparisons. The result of the ANOVA rejects the null hypothesis at 5% significance level, i.e., p values less than 0.05 were considered to show statistical significance.

2.4 Results

2.4.1 PTT varies across different MI models

PTT values for different mouse models were estimated via ICG injection as described in the methods section. The PTTs of the *wt*-PO were significantly longer compared to non-infarct mice (Figure 2.2A, $p<0.0001$). The highest PTT values were observed 3 days post MI and subsequently decreased over time indicating healing of the injured myocardium and functional improvements over 21 days. As the ANOVA analysis indicated significant difference in the PTTs at different days post MI, Tukey post hoc tests were performed. Post hoc comparisons using the Tukey HSD test indicated that the PTT in mice at 10 days post MI were significantly different from 3 and 21 days post MI ($M= 2.2720$, $SD=0.1878$, $p=0.0017$). For the *wt*-I/R model, which induces a less severe infarct, longer PTTs were also observed compared to the non-infarct mice (Figure 2.2B, $p=0.0206$). However, the decrease in PTT values from day 3 to day 21 post MI showed no statistically significant difference over time ($p=0.2828$).

PTT values of the kit^{W}/kit^{W-v} group were analysed to assess effects of the c-kit protein deficiency on heart function and remodelling post MI. kit^{W}/kit^{W-v} after PO were compared with non-infarcted kit^{W}/kit^{W-v} mice in addition with *wt*-PO to assess effects of c-kit expression on the functional healing response in MI by VOT. The effect of the deficiency of the c-kit protein on heart function was assessed from VOT measurements of kit^{W}/kit^{W-v} mice at 3, 10 and 21 days post MI surgery. No improvement in the PTT was measured in kit^{W}/kit^{W-v} mice after PO with respect to non-infarct kit^{W}/kit^{W-v} (Fig. 3, $p<0.0001$). In contrast to what was observed in *wt* mice (Fig. 2a), ventricular function did not recover in kit^{W}/kit^{W-v} PO mice. VOT-derived PTT values following MI showed no significant differences at different days (3, 10 and 21) post MI (Fig. 3, $p = 0.7079$). These results imply that the lack of proper healing and impaired cardiac function in kit^{W}/kit^{W-v} mice post MI can accurately be captured by VOT.

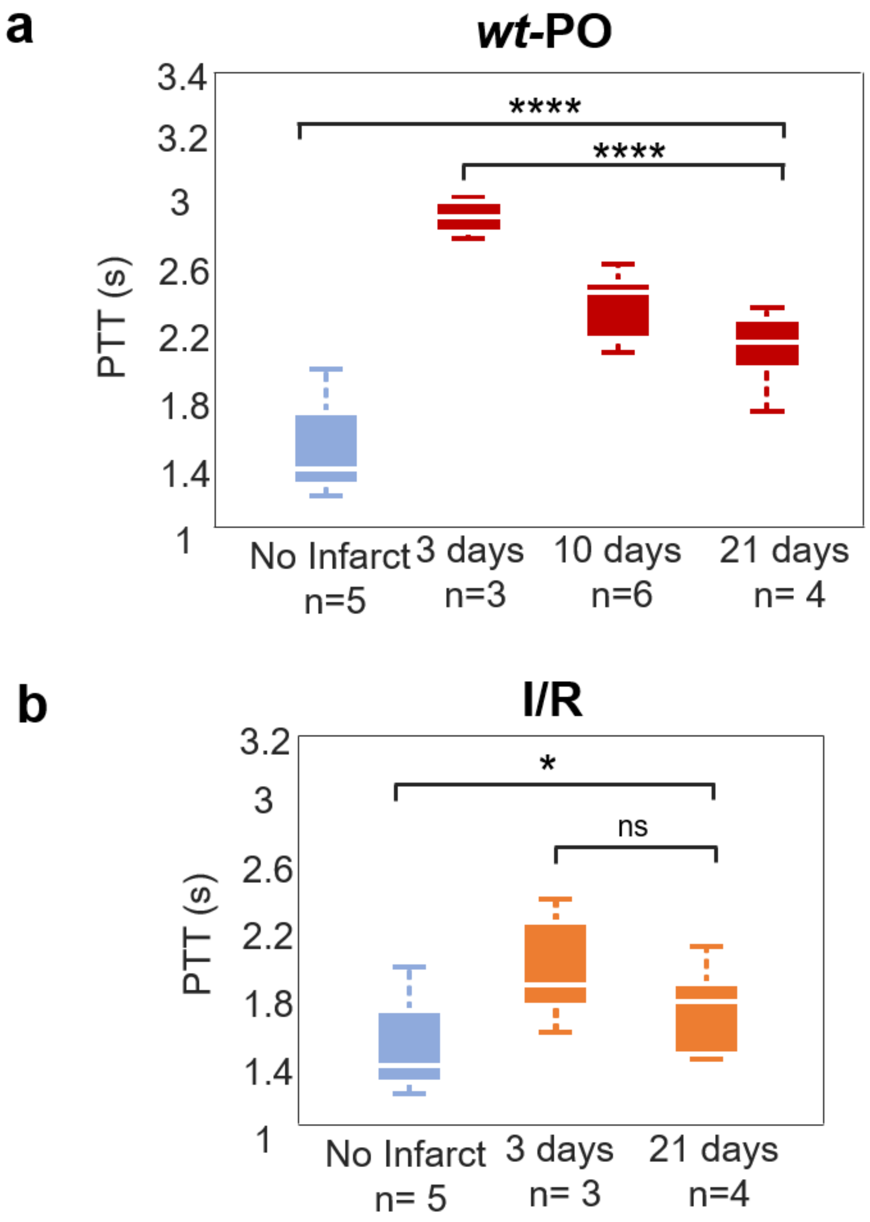

Figure 2.2: Pulmonary transit times in PO and I/R models. (a) PTT values represented no MI (blue) and 3, 10 and 21 days post MI for *wt*-PO (red) models. ANOVA analysis showed statistical significance for different days *($p < 0.0001$)*, suggesting myocardial healing. (PTT; pulmonary transit time, PO; permanent occlusion, MI; myocardial infarction). (b) PTT values represented in boxplots for no MI (blue) and I/R models (orange), where the PTT was statistically shorter in no MI mice compared to I/R models ($p = 0.03$) and PTT values represented at 3 and 21 days post MI showed no statistical difference *($p = 0.28$)* suggesting no myocardial healing. (I/R, ischemic reperfusion)

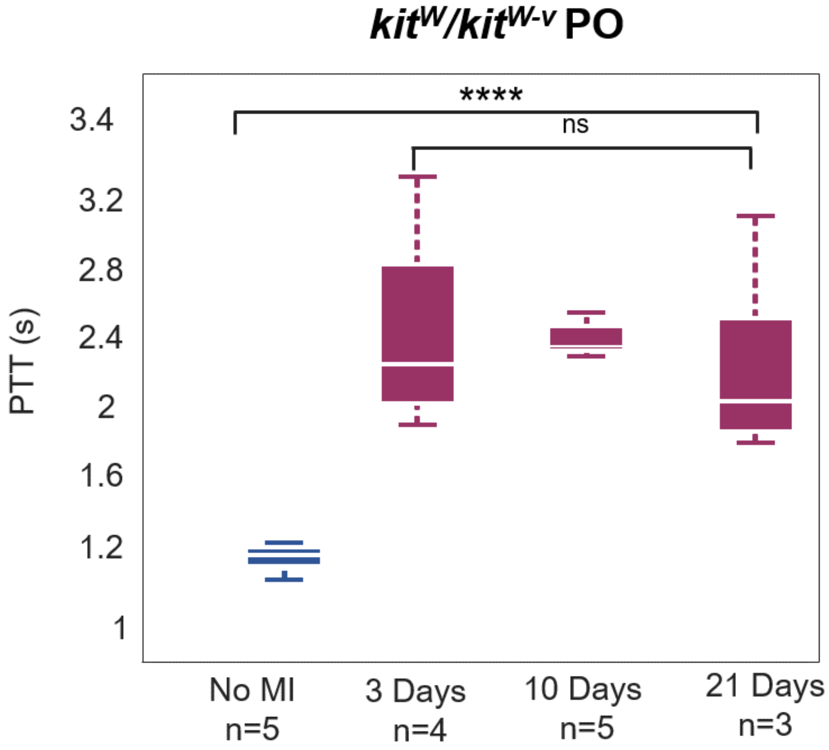

Figure 2.3: Pulmonary transit times in *kit*^{W}/*kit*$^{W-v}$ models. PTT values represented with no MI (blue) and 3, 10 and 21 days post MI (purple). ANOVA analysis showed significant difference in PTT values between no MI and MI models ($p<0.0001$) and no significant difference in PTT values was detected for 3, 10 and 21 days post MI ($p= 0.7079$) indicating no positive myocardial healing (PTT; pulmonary transit time, MI; myocardial infarction)

2.4.2 VOT detects ICG perfusion through reperfusion area

Reperfusion injury is a pathophysiology associated with rapid blood reperfusion following recanalization of an occluded coronary artery during MI treatment. *wt*-I/R mice showed disrupted vasculature located in regions affected by the temporary LAD ligation (Figure 2.1C, white arrows). Similar vasculature was not detected in PO models (*wt* and *kit*^{W}/*kit*$^{W-v}$ mice). The presence of injuries in *wt*-I/R models was corroborated by assessing the ICG perfusion through the suspected injury sites and compared to the PO and non-infarct mice (Figure 2.4A). ICG (bound to blood plasma) clearly perfused through structures located on top of the heart (white arrows in Figure 2.4A), as manifested by an increase in the OA signal intensity at these points (Figure 2.4B). No signal increase was detected in the

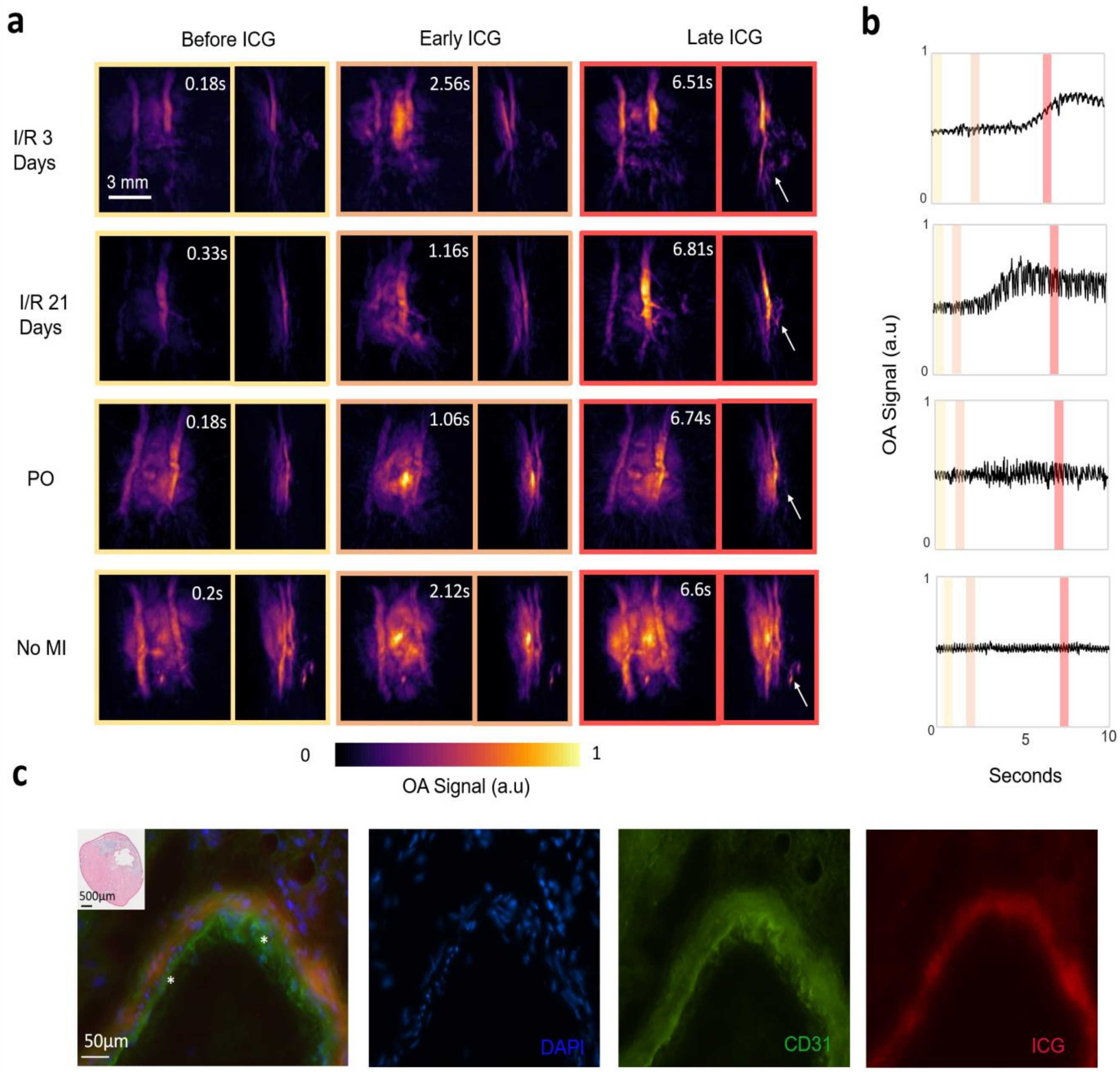

Figure 2.4: Reperfusion injury detection (a) ICG perfusion tracking in I/R (3 & 21 days), PO and no MI models, where before (yellow), early (orange) and late (red) ICG phases are shown. Note white arrows identifying areas where ICG either perfused through (both I/R models) and where ICG didn't perfuse through (PO & no MI). Each column of OA MIP images represent coronal views (left) and sagittal views (right). (ICG; indocyanine green, I/R; ischemic reperfusion, PO; permanent occlusion, MI; myocardial infarction). (b) OA signal time intensity plotted at reperfusion injury sites or similar locations are shown for each model over a period of 1000 frames, where different phases of ICG perfusion are depicted (before - yellow, early - orange, late - red). OA images in (A) correspond to the colored bars in the OA signal time intensity plots. Note how there is a clear increase in OA signal in I/R models and no OA signal change in PO and control models. (OA; optoacoustic) (c) Fluorescence microscopy of infarcted myocardium 24h following I/R shows a gradient of ICG (red) across the microvascular endothelium (*, CD31 staining in green) into the perivascular space. H&E staining of infarcted myocardium at the midventricular level towards the apex shown in upper left panel.

PO and non-infarct mice, suggesting that the observed absorbing structures do not correspond to disrupted vasculature. On the other hand, the increased VOT signal intensity was maintained for a relatively long time for the selected structures in the *wt*-I/R models, which appears to indicate the presence of leaky vasculature. See supplementary video 1 for visualisation of ICG perfusion through the I/R heart. Altered ICG leakage due to increased endothelial permeability was confirmed using fluorescence microscopy (Fig. 4C). Within the infarcted myocardium, ICG (red) was shown to distribute along a gradient across the microvascular endothelium (green*) into the perivascular space, corroborating the *in vivo* OA detected ICG signal in reperfusion models.

2.4.3 VOT detects arrhythmic cardiac dynamic variations between PO and I/R mice

Cardiac cycles were examined with VOT in the *wt*-PO, *wt*-I/R mice as well as in *kit*^{W}/*kit*$^{W-v}$ mice after PO MI. An example of 5000 volumetric OA image frames recorded over 50s is available in Supplementary video 2. Irregularities in the cardiac cycle (arrhythmias) were associated to elongated cycles with 82 ±31% increase in duration as compared to standard (periodic) cycles (Figure 2.5A). In periodic cycles (yellow shade), ventricular activity remained relatively consistent, while ventricular activity was concentrated in diastole in the irregular cycles (Figure 2.5A, red shade), occupying approximately 75% of the cycle length. Cardiac cycle irregularities were detected in all *wt*-PO mice (n=21) and in 37.5% of *wt*-I/R mice (3 out of 8 mice, n=8), while only periodic cycles were detected in *kit*^{W}/*kit*$^{W-v}$ PO mice (n=12) (Figure 2.5B). Longer PTTs were also found in *wt*-I/R mice featuring cardiac cycle irregularities but not in mice with regular cardiac cycles (Figure 2.5C, $p<0.01$). Thus suggests a high correlation between PTT values and the presence of arrhythmic events, as also observed in hypoxic mouse models (Ivankovic et al., 2019).

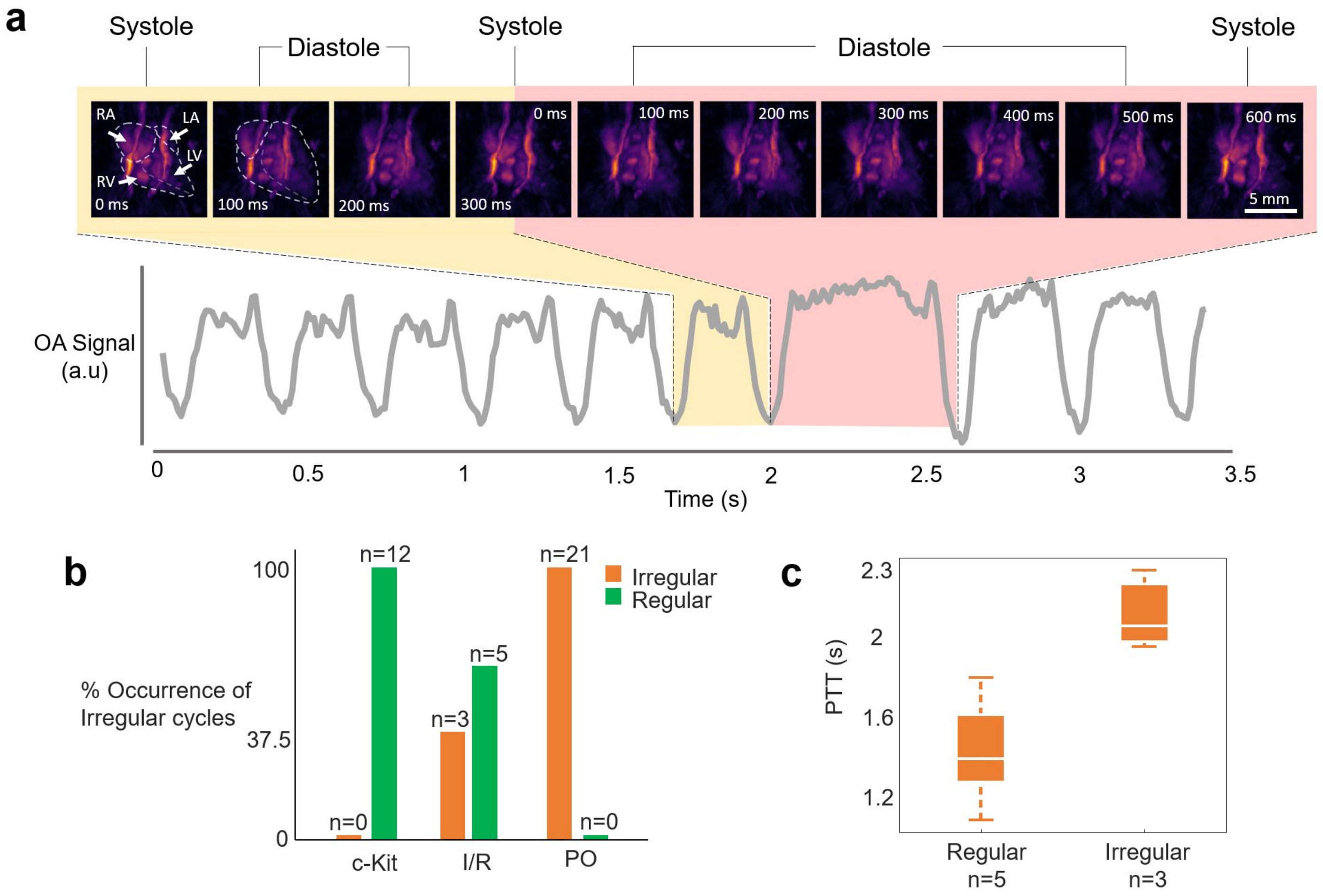

Figure 2.5: Cardiac cycle characterization in MI models. (a) OA signal intensity time profile plotted in grey curve where periodic cycles are detected in the beginning followed by irregularity. Above time plot are individual OA frames of the beating heart across 600 ms, where yellow shading represents a periodic cycle and red shading represents and irregular cycle. Note the differences in systolic and diastolic phases. (OA; optoacoustic, RA; right atrium, LA; left atrium, RV; right ventricle, LV; left ventricle). (b) Histogram showing occurrence of cycle irregularities in PO, I/R and $kit^{W}/kit^{W\text{-}v}$ models, where 0% occurrence was noted in c-kit models, 37.5% occurrence in I/R models and 100% occurrence in PO models. Orange color represents irregular cycles and green represents regular cycles. (PO; permanent occlusion, I/R; ischemic reperfusion) (c) Boxplot representation of relationship between PTT values and cardiac cycle trends in I/R models, where a longer PTT was found in models with cycle irregularities (n=3) compared to models with regular cardiac cycles (n=5) *($p = 0.005$)*

2.5 Discussion

The presented results illustrate the advantages of VOT in assessing cardiac dynamics following myocardial infarction. Various models of MI are available to help deepen our understanding of the healing response in response to mechanically or genetically-induced ischemic injuries. The goal of this study was to assess whether VOT can capture distinct yet subtle differences in myocardial injury following MI. The unique capacity of the VOT technique for the simultaneous assessment of cardiac morphology, function, rhythm and vascular morphology *in vivo* and in real time has the potential to offer new insights into the biology of myocardial healing and remodelling.

The PO model involves consistent closure of the LAD, which mimics a clinical acute, untreated MI with relatively large infarct size and worse prognosis (Lindsey, Bolli, et al., 2018; Muthuramu, Lox, Jacobs, & De Geest, 2014). Ligation of the LAD for 30 minutes in *wt*-I/R models resembles the clinical scenario of coronary revascularization by undergoing rapid treatment in acute MI (Lindsey, Bolli, et al., 2018). The different surgical techniques employed in this study which have imposed varying mechanical stress levels to the heart, have also resulted in different healing routes post MI. Herein, it was shown that PTT values vary amongst different MI models. In PO models, the PTT was generally longer than in the *wt*-I/R models agreeing with the high severity of the induced injury. The PTT has previously been shown to vary depending upon the time point post MI and its size (Lin et al., 2017). The PTT and left ventricular ejection fraction (LVEF) have also been shown to inversely correlate, suggesting that ventricular function can be determined by analysing the PTT. In addition, PTT measurements enabled the assessment of cardio-pulmonary interactions and function under stress (Ivankovic et al., 2019). In general, longer PTT values indicate impaired heart function. The normalization of PTT values in the PO model indicate myocardium healing following MI, while no significant changes in PTT values were detected in the I/R model. In support of these findings, no change or improvement in LVEF was detected in patients with reperfused MI and subsequent reperfusion injury (Ganame et al., 2009). Therefore, although it is generally accepted that I/R models impose less severe infarcts compared to PO models, it appears that the healing capacity in I/R models is hindered, which possibly reflects the impact of reperfusion injury.

The regenerative capabilities of c-kit cells in the heart has long been debated. Experimental results have shown that c-kit cells do indeed promote heart regeneration post MI, which have prompted clinical trials yielding controversial outcomes (Hsieh et al., 2007; Yu et al., 2014). The inconclusive results call for more preclinical investigations before translating treatment strategies into the clinical setting. For this, advanced imaging techniques with sufficient spatio-temporal resolution for studying the murine heart can be of great value. VOT is capable of capturing the murine heart in real-time, non-invasively and volumetrically, posing as an ideal imaging device to image cardiovascular disease in preclinical models. We tested the sensitivity of VOT by examining different murine MI models. In the $kit^{W}/kit^{W\text{-}v}$ mice, no relevant regeneration of cardiac function was detected by VOT over a 21-day period post permanent LAD ligation. These findings were compared to PO in wild-type mice under identical experimental conditions, where an improvement in LV function was recorded. This highlights VOT's capacity to assess different degrees of the healing response to MI and emphasizes the important role of c-kit cells in cardiac regeneration post MI (Hsieh et al., 2007).

The acquired data of the *wt*-I/R model were further investigated to assess the presence of impaired vasculature with increased endothelial permeability, common in reperfusion injuries. The VOT images of the *wt*-I/R hearts presented morphological differences compared to mice without reperfusion injury (PO and infarct). Notably, increased leakage of ICG into extravascular space was identified around the infarct area, where reperfusion injury is expected to occur (Granger & Kvietys, 2017). I/R is known to cause endothelial dysfunction through various mechanisms, where permeability of the endothelium increases following I/R, thus perpetuating myocardial injury (Granger & Kvietys, 2017). Albumin, which ICG binds to *in vivo* when IV injected, has been previously shown to be a bio-marker of vascular permeability as its structure (like other large serum proteins) tend to accumulate in areas of increased vascular permeability (Vandoorne, Addadi, & Neeman, 2010). The increased VOT-detected leakage of albumin-bound ICG following IV injection, may thus serve as a bio-marker of endothelial dysfunction in *wt*-I/R models (Alander et al., 2012). These observations were only recorded in *wt*-I/R models and were not present in wild-type and *kit*^{W}/*kit*$^{W\text{-}v}$ mice following PO. The ICG retention in the injured region, as confirmed by fluorescence microscopy, of the I/R hearts similarly follow a previously described schematic on ICG perfusion in MI models (Sonin et al., 2017; Vandoorne et al., 2010). Different phases of ICG perfusion post MI were studied in an I/R rat model. It was shown that in the initial (arterial) phase of perfusion, ICG fills the coronary arterial network of the heart including vasculature with restored blood flow. It was also shown that this is followed by the delayed (capillary) phase, where ICG is detected only in regions of myocardial injury. Disrupted coronary microcirculation was also observed in areas of irreversible reperfusion injury, where excessive leakage of plasma was present (Sonin et al., 2017). Compared to the unaffected myocardium, the excessive leakage causes retention of ICG, resulting in an OA signal increase measured by VOT. In this study, the entire perfusion cycle of ICG and its retention in the reperfused areas of the myocardium could be detected in real-time and non-invasively. This allowed for fast and direct detection of areas subject to irreversible damage from I/R MI and could serve as a diagnostic tool in classifying the severity of the cardiac injury in those models.

High-frame-rate (100 Hz) imaging with VOT has further allowed for a beat-to-beat analysis of the cardiac cycles. Rapid detection of cycle irregularities was possible due to the true 4D imaging capabilities of VOT, whereby volumetric images of the heart and the OA signal intensity time profiles at different points could simultaneously be analysed. All PO-induced mice presented at least one instance of cycle irregularity in the cardiac cycle post MI, while in *wt*-I/R models irregularities were detected only in 3 out of 8 mice. Notably, no irregularities were observed in the *kit*^{W}/*kit*$^{W\text{-}v}$ mice. Cardiac arrhythmias are common in patients following MI, where cycle irregularity can be attributed to slower or faster heart rates (Cohen, Boiangiu, & Abidi, 2010; Tung & Zimetbaum, 2010). The irregular cycles detected by VOT exhibited almost double the length of the regular periodic cycles, where ventricular activity was extended in the diastolic phase; potentially representing arrhythmic events. The real-time heart motion of the heart is known to serve as an important indicator for the MI assessment (Thygesen et al., 2012). The obtained results suggest that severity of the MI models (with PO considered as the most severe) may dictate frequency of the detected arrhythmic events. However, it remains unclear why no arrhythmic events were detected in the *kit*^{W}/*kit*$^{W\text{-}v}$ mice, and future studies are anticipated to elucidate these findings.

In conclusion, we have shown that dedicated preclinical cardiac VOT imaging can serve as an advanced imaging tool for assessing myocardial injury and function in different MI murine models. VOT is capable of rendering real-time, volumetric and non-invasive data of the murine heart, thus allowing for a comprehensive analysis of the whole heart function under MI stress. Thereby, it has the potential to become a powerful preclinical imaging tool in advancing our understanding of cardiovascular diseases.

3. Volumetric optoacoustic tomography enables non-invasive *in vivo* characterization of impaired heart function in hypoxic conditions

Published in Scientific Reports, 2019 10th June; 9(1):8369. DOI:10.1038/s41598-019-44818-8

Authors

Ivana Ivankovic[1,2], Xose Luís Deán-Ben [1,2], Hsiao-Chun Amy Lin [3,4], Zuwen Zhang [5], Benjamin Trautz[5], Andreas Petry[5,] Agnes Görlach[4,5,6] and Daniel Razansky [1,2,3,4]

[1]Faculty of Medicine and Institute of Pharmacology and Toxicology, University of Zurich, Switzerland

[2]Institute for Biomedical Engineering and Department of Information Technology and Electrical Engineering, ETH Zurich, Switzerland

[3]Institute for Biological and Medical Imaging, Helmholtz Center Munich, Neuherberg, Germany

[4]Faculty of Medicine, Technical University of Munich, Germany

[5] Experimental and Molecular Pediatric Cardiology, German Heart Center Munich at the TU Munich, Germany

[6]DZHK (German Centre for Cardiovascular Research), Partner site Munich, Munich Heart Alliance, Munich, Germany

No conflict of interest disclosed

3.1 Abstract

Exposure to chronic hypoxia results in pulmonary hypertension characterized by increased vascular resistance and pulmonary vascular remodelling, changes in functional parameters of the pulmonary vasculature, and right ventricular hypertrophy, which can eventually lead to right heart failure. The underlying mechanisms of hypoxia-induced pulmonary hypertension have still not been fully elucidated while no curative treatment is currently available. Commonly employed pre-clinical analytic methods are largely limited to invasive studies interfering with cardiac tissue or otherwise *ex vivo* functional studies and histopathology. In this work, we suggest volumetric optoacoustic tomography (VOT) for non-invasive assessment of heart function in response to chronic hypoxia. Mice exposed for 3 consecutive weeks to normoxia or chronic hypoxia were imaged *in vivo* with heart perfusion tracked by VOT using indocyanide green contrast agent at high temporal (100 Hz) and spatial (200 µm) resolutions in 3D. Unequivocal difference in the pulmonary transit time was revealed between the hypoxic and normoxic conditions concomitant with the presence of pulmonary vascular remodelling within hypoxic models. Furthermore, a beat-to-beat analysis of the volumetric image data enabled identifying and characterizing arrhythmic events in mice exposed to chronic hypoxia. The newly introduced non-invasive methodology for analysis of impaired pulmonary vasculature and heart functions under chronic hypoxic exposure provides important inputs into development of early diagnosis and treatment strategies in pulmonary hypertension.

3.2 Introduction

Pulmonary hypertension (PH) is a disorder characterized by pulmonary vascular remodelling, right ventricular hypertrophy and increased pulmonary arterial pressure. PH has been associated with various disorders while, according to the recent WHO classification, it is regarded as a separate entity when associated with hypoxia or chronic diseases of the respiratory system (Heresi et al., 2017). The latter include chronic obstructive pulmonary disease (COPD), interstitial lung diseases, sleep disordered breathing, but also chronic exposure to high altitude and some rare neonatal diseases (Forfia et al., 2013; Stenmark et al., 2006).

Murine models have been widely used to gain deeper insight into lung-heart interactions under chronic hypoxic conditions (E. Cahill et al., 2012). The hypoxia-inducible factor (HIF) has been highly implicated in the development of PH (Shimoda & Semenza, 2011) where several preclinical studies focus on the molecular mechanisms of HIF and its role in PH (Chen, Shen, Zhang, & Shu, 2017; Li et al., 2016; L. Wang, Zhou, Li, & Zhu, 2014; Yamashita et al., 2008). However, there is a lack of direct functional studies of the heart in response to chronic hypoxia. Methods for assessing pulmonary and cardiac structural alterations in PH are usually limited to histopathological *ex vivo* analyses looking at right ventricular (RV) hypertrophy and pulmonary vasculature changes. RV catheterization is an invasive *in vivo* procedure to measure pressure differences as a surrogate parameter of increased pulmonary arterial pressure (Campen, Shimoda, & O'Donnell, 2005; Fagan, 2001; Howell, Preston, & McLoughlin, 2003; McGuire & Bradford, 1999). Yet, the majority of the analytical methods interfere with integrity of the heart, which calls for introduction of new methods for direct *in vivo* assessment of cardiopulmonary coupling in small animal models.

In vivo imaging of the murine heart is challenging due to its small size and rapid motion (Doevendans, Daemen, De Muinck, & Smits, 1998), which imposes hard requirements on the spatial and temporal resolution of non-invasive imaging modalities to accurately capture a heart volume of less than a cubic centimeter beating at a 400-600 cardiac cycles per minute. Even though cardio-respiratory gating in magnetic resonance imaging (MRI) and X-ray computed tomography (CT) may enable characterizing some of the *in vivo* functional cardiac parameters, those methods are generally ill-suited for cardiac imaging due to insufficient temporal resolution when performing true 3D whole-heart imaging at high spatial resolution (Kojonazarov et al., 2018; Yu et al., 2014). To this end, ultrasound (US), and more recently ultrafast US, are arguably the most suitable modalities for cardiac imaging in murine models. US enables discerning anatomy and measuring important physiological parameters, such as blood flow (Pistner et al., 2010). Yet, it is generally not suitable for measuring some of the key functional parameters in the entire heart volume in 3D, in particular for analysis of right ventricular size within murine models. To our knowledge, very few methods generally exist for non- or minimally-invasive imaging and assessment of the effects of exposure to chronic hypoxia in pre-clinical models.

Optoacoustic (OA) imaging is becoming an increasingly powerful tool in pre-clinical research, in particular for *in vivo* cardiac imaging in murine models, for a number of reasons: (1) the high number of effective voxels rendered by state-of-the-art systems allows for imaging the whole murine heart with high spatial resolution using stationary matrix detection arrays; (2) optical contrast allows for blood perfusion monitoring (Xosé Luís Deán-Ben et al., 2015), and (3) the high temporal resolution in 3D facilitates analyzing functional parameters of the living murine heart on a beat to beat basis (Lin et al., 2017). An important functional parameter that can be measured with OA via injection of a contrast agent is the pulmonary transit time (PTT). The latter has been shown to significantly decrease in infarct murine models and hence can serve as an important indicator of heart function (Lin et al., 2017). Another key feature of volumetric optoacoustic tomography (VOT) is the ability of imaging the entire heart with a single laser pulse. This is crucial to characterize potential delays in cardiac activation across different regions, e.g. during arrhythmic events. In this work, we demonstrate the capabilities of a recently developed real-time three-dimensional OA imaging system for analyzing heart function *in vivo* and non-invasively in chronic hypoxic murine models.

3.3 Materials and methods

3.3.1 Animal models

All animal procedures were approved by the local legislation on protection of animals (Government of Upper Bavaria, Munich, Germany under animal protocol reference number 55.2-1-2532-50-12) and conducted in accordance with the European directive 86/609/EEC and internal regulations of the Technical University of Munich and Helmholtz Centre Munich. Mice (129S/Sv/C57BL6 mixed background) were maintained for 21 days either under normoxic conditions (n=3) or under hypoxic conditions (10% oxygen, n=4) in a custom-built normobaric chamber, as described previously (Chalupsky, Kračun, Kanchev, Bertram, & Görlach, 2015).

3.3.2 Animal handling

All mice were anesthetized with approximately 2% isoflurane – oxygen medical mix (~0.81 L/min gas flow) for *in vivo* imaging of the heart. The fur covering the region of interest was initially clipped and then completely removed with hair removal cream. During imaging, the anesthetized mice were placed on top of a solid agar matrix filling the volume enclosed by the spherical array (Figure 3.1 A). Warmed ultrasound gel was further used between the tissue surface and the agar matrix for optimum acoustic coupling and maintaining homeostasis. Approximately 15 sec after beginning of the image acquisition each mouse was intravenously injected with 100 nmol/L of indocyanine green (ICG) contrast agent (Profiplus Bvba, Kortessem, Belgium) diluted in 50 µl saline solution. Mice were then injected a second time 10 minutes after the first injection.

3.3.3 Volumetric optoacoustic tomography (VOT) of the murine heart

High-frame-rate images of the beating murine heart were acquired with a VOT system specifically designed for high performance pre-clinical cardiac imaging (Figure 3.1 B) (Dean-Ben et al., 2013; Xosé Luís Deán-Ben et al., 2015). The imaging system consists of a spherical array transducer (Imasonic Sas, Voray, France) composed of 512 piezoelectric elements with 5 MHz central frequency and >80% detection bandwidth. The array provides 140° solid angular coverage with 40 mm radius.

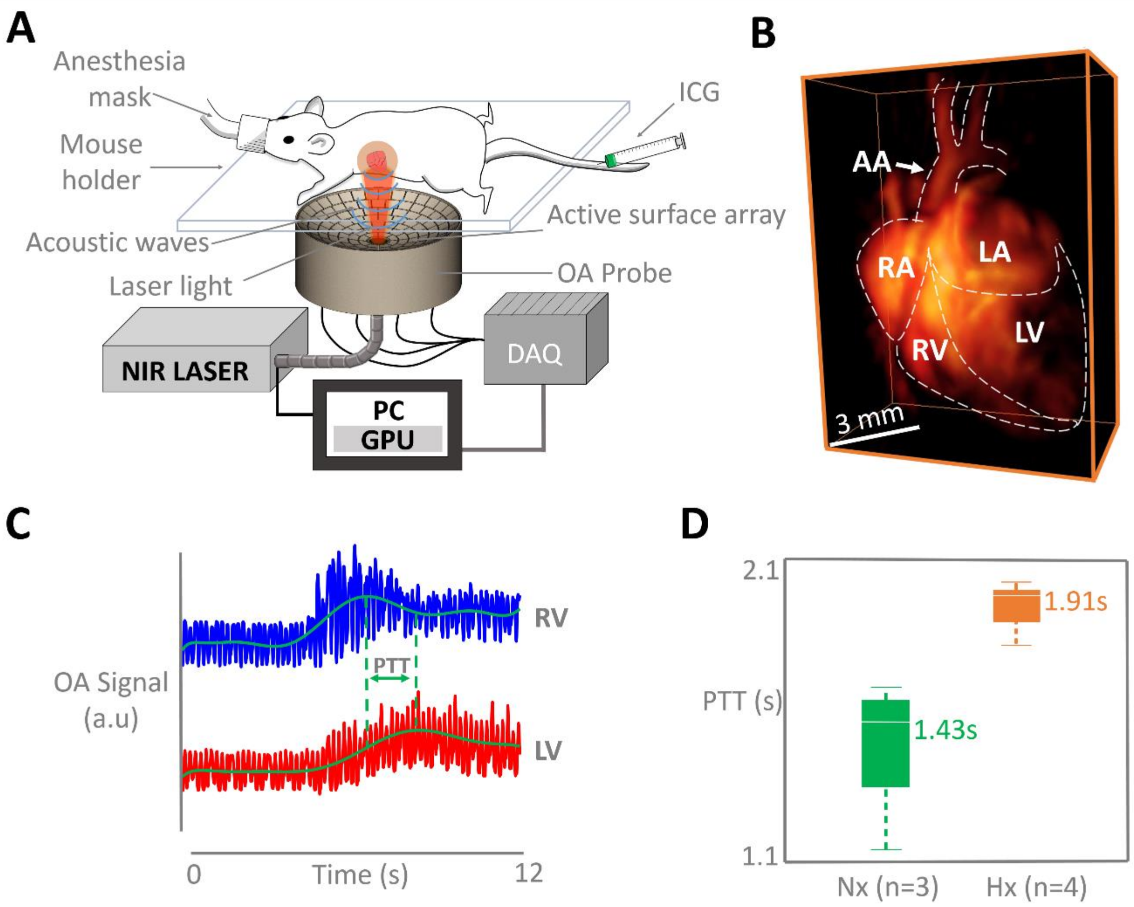

Figure 3.1: The experimental protocol (A) Non-invasive imaging procedure of the murine heart with the volumetric optoacoustic tomography. (OA; optoacoustic, ICG; indocyanine green, NIR; near-infrared, PC; personal computer, GPU; graphics processing unit, DAQ; data acquisition system). **(B)** 3D view of the optoacoustic image a of the murine heart reconstructed with a single laser pulse (AA - aortic arch, RA - right atrium, LA - left atrium, RV - right ventricle, LV - left ventricle). **(C)** Temporal profiles of the optoacoustic signal intensities in two voxels in RV and LV, as indicated in (B). **(D)** The pulmonary transit time (PTT) is calculated as difference in time of arrival of the contrast agent, i.e. time difference corresponding to the maximum signal values in the RV and LV (Hx; mean-1.91 [1.7386 – 2.02] s versus Nx; mean-1.43 [1.0602-1.64] s, $P < 0.0023$). [Add copyright info here, do this for all images.]

The large angular coverage of the array reduces limited-view effects and further enables an improved sensitivity and deeper penetration. In the experiments, the spherical array was held pointing upwards (Figure 3.1 A). The spherical volume enclosed by the spherical aperture was filled with clear agar (3w/v% concentration), which provided acoustic coupling while being transparent for light. Short light pulses (<10 ns) at 800 nm wavelength and 100 Hz repetition frequency were generated by a fast-tuning optical parameter oscillator laser (Innolas Laser GmbH, Krailling, Germany) and guided via a fibre bundle (Ceram Optec GmbH, Bonn, Germany) through the center of the transducer array. The 800nm wavelength corresponds to the absorbance peak of ICG. The OA signals for all elements of the array were simultaneously sampled by a custom-made parallel data acquisition system (Falkenstein

Microsysteme GmbH, Taufkirchen, Germany). Volumetric images were reconstructed on the fly for each laser pulse by a graphics processing unit-based 3D back-projection reconstruction algorithm, which enabled real-time preview during the experiments and facilitated correct positioning of the animal (Ozbek, Dean-Ben, & Razansky, 2013). After correct positioning, VOT data was acquired for a total of 5000 frames and 3D images were later reconstructed offline in a volume of 12x12x12 mm^3 (120x120x120 voxels). All processing steps were performed in MATLAB (MathWorks Inc, Natick, USA).

3.3.4 Pulmonary transit time (PTT)

The method for extracting the PTT values from the heart image sequence has been previously described (Xosé Luís Deán-Ben et al., 2015). In short, the PTT was measured as the difference between the time points corresponding to the maximum signal peaks for the right (RV) and left ventricles (LV), corresponding to the time of appearance of the ICG bolus (Figure 3.1 C). The PTT was measured for both hypoxic and normoxic models, followed by statistical analyses. Voxels in the RV and LV were identified in the VOT images using a 4-dimensional viewing toolbox in Matlab.

3.3.5 Cardiac cycle characterization

OA signal intensity profiles were extracted from different locations in the LV and RV, the left atria and right atria as well as the aortic arch by selection of voxels in the images. These cycles were used for characterizing the heart rate as well as irregularities corresponding to arrhythmias. The latter were identified when the length of a single cycle significantly exceeded the average cycle length of a normal periodic rhythm. Also, the spectrogram of the cardiac cycle was calculated as the short-time Fourier transform (STFT) of the signals. The STFT was used to resolve the frequency content at specific time points and track it over time. Abnormal beating events are expected to result in a lower frequency distribution in the STFT as opposed to the normal beating rhythm.

3.3.6 Immunohistochemistry and Fulton index

Hypoxia-induced pulmonary vascular remodelling was validated by immunohistochemistry, as described previously (Chalupsky et al., 2015). Briefly, lung tissue samples were immersed in 10% buffered formalin solution for 48 h and subsequently embedded in paraffin (FFPE). FFPE lung sections were stained with an antibody against α-smooth muscle actin (clone 1A4; DAKO, Hamburg, Germany). The slides were heated at 60°C for 1 h before rehydration in a series of alcohol solutions of decreasing alcohol concentration. The endogenous peroxidase activity was quenched in 1% hydrogen peroxide solution in methanol. The hydration process was completed by rinsing in DAKO wash buffer. Sections were heated in a water bath at 90°C while submerged in antigen retrieval pH 9 epitope retrieval solution (DAKO) for 30 min. They were subsequently blocked in blocking reagent for 1 h, and then incubated with the antibody 1:100 diluted in M*O*M diluent (Vector M*O*M kit) (Vector Laboratories, Burlingame, CA) for 1 h at room temperature in a humidity chamber. The sections were washed in DAKO wash buffer and the secondary antibody was applied (anti-mouse IgG in dilution 1:250). The avidin–biotin complex (Vectastatin Elite Kit, Vector Laboratories) was applied to the slides for 30 min at room temperature. The chromogenic reaction was performed with diaminobenzidine (DAB; DAKO) for 5 min at room temperature. Slides were counterstained with Mayer's hematoxylin for 30 s (Merck, Darmstadt, Germany), dehydrated in an ascending alcohol concentration, and mounted with Entelan (Merck). Positive and negative controls were included with each run. For evaluation of each lung, small α-smooth muscle actin positive vessels less than 30μm were identified in three randomly selected regions of interest covering an area of 1mm^2 each (Z. Zhang et al., 2019).

To determine the Fulton index as a measure of right ventricular hypertrophy, the right ventricle was separated from the left ventricle and septum, and masses were determined.

3.4 Results

3.4.1 Volumetric optoacoustic tomography of the murine heart:

The VOT imaging setup was optimally designed for *in vivo* murine heart imaging (Figure 3.1A). The dedicated design consists of a spherical array transducer which was held pointing upwards for optimal OA signal detection of the heart, a fiber bundle for light illumination, a fast-tuning optical parameter oscillator laser and a data acquisition system for simultaneous OA signal detection for all elements of the array. Mice which have been exposed to chronic hypoxia for 3 weeks (n=4) and normoxic counterparts (n=3) were anesthetized and laid on the transducer with the chest facing down. High-frame-rate images of the beating murine heart were acquired with the VOT system, specifically designed for high performance pre-clinical cardiac imaging (Figure 3.1 B). The VOT data was acquired for each ICG injection for a total duration of 50 s (5000 frames), which is a sufficient amount of time to track blood flow through the pulmonary circuit.

3.4.2 Pulmonary Transit Time

The PTT was measured as the difference between the time points corresponding to the maximum signal peaks for the right (RV) and left ventricles (LV), corresponding to the time of appearance of the ICG bolus (Figure 3.1C). Boxplots of the measured PTT values for hypoxia-treated (n=4 , 6 injections altogether) and normoxic models (n=3 , 6 injections altogether) are presented in Figure 3.1D. A t-test was carried out to analyze the difference between the observed PTT values. The PTT values measured from the hypoxic models were significantly longer than those obtained for the normoxic models (mean-1.91 [1.7386 – 2.02] s versus mean-1.43 [1.0602-1.64] s, $P < 0.0023$). This clear difference in PTT between hypoxia-treated and normoxic mice strongly suggests that chronic hypoxia affects cardiac function and/or pulmonary haemodynamic.

3.4.3 Immunohistochemistry and right ventricular hypertrophy

Characteristically, exposure to chronic hypoxia results in a vasoconstrictor response as well as in muscularization of small pulmonary vessels indicative of pulmonary vascular remodelling leading to an increase in pulmonary vascular resistance and right ventricular hypertrophy. As evinced by staining for α-smooth muscle actin of lung sections (Figure 3.2A), the number of small muscularized pulmonary vessels was significantly increased in lung sections from hypoxic mice in comparison to normoxic mice (Figure 3.2B), indicating pulmonary vascular remodelling. Subsequently, the masses of the right and left ventricle including septum were measured and the Fulton index was determined as a measure of right ventricular hypertrophy. Compared to the normoxic mice, the Fulton index was elevated in hypoxic mice indicating right ventricular hypertrophy (Figure 3.2C)

3.4.4 Heart beat characterization

Due to the excellent temporal resolution of the VOT system, it was possible to characterize the heart motion on a beat-by-beat basis. Heart rate variability was clearly identified within the hypoxic models (n=3 (3 of 4)) in VOT image sequences of 500 frames (100 frames per second), whereas only periodic cycles were recorded in normoxic models (Figure 3.3A). A t-test analysis revealed that the irregular cycles, marked with grey crosses in Figure 3.3A, have a length of 333 [282 – 437.3] ms versus 189 [145 – 229] ms, $P < 0.001$ (Figure 3.3B). The real-time 3D imaging capability of VOT allows for mapping the mechanical motion globally throughout the heart by plotting time-lapse OA signal intensity profiles in different locations within the heart wall (Figure 3.3C). The profiles indicate that the length of the irregular heart cycle is approximately twice the duration of the regular cycles. This may be attributed to a steady sinus rate and impaired atrioventricular conduction or ‘heart block’ rather than a supra-ventricular arrhythmia (Goldberger, 2017). Atrial deformations may additionally be produced during ventricular pauses, which may become visible if the resolution of the VOT system is enhanced by using a higher frequency array.

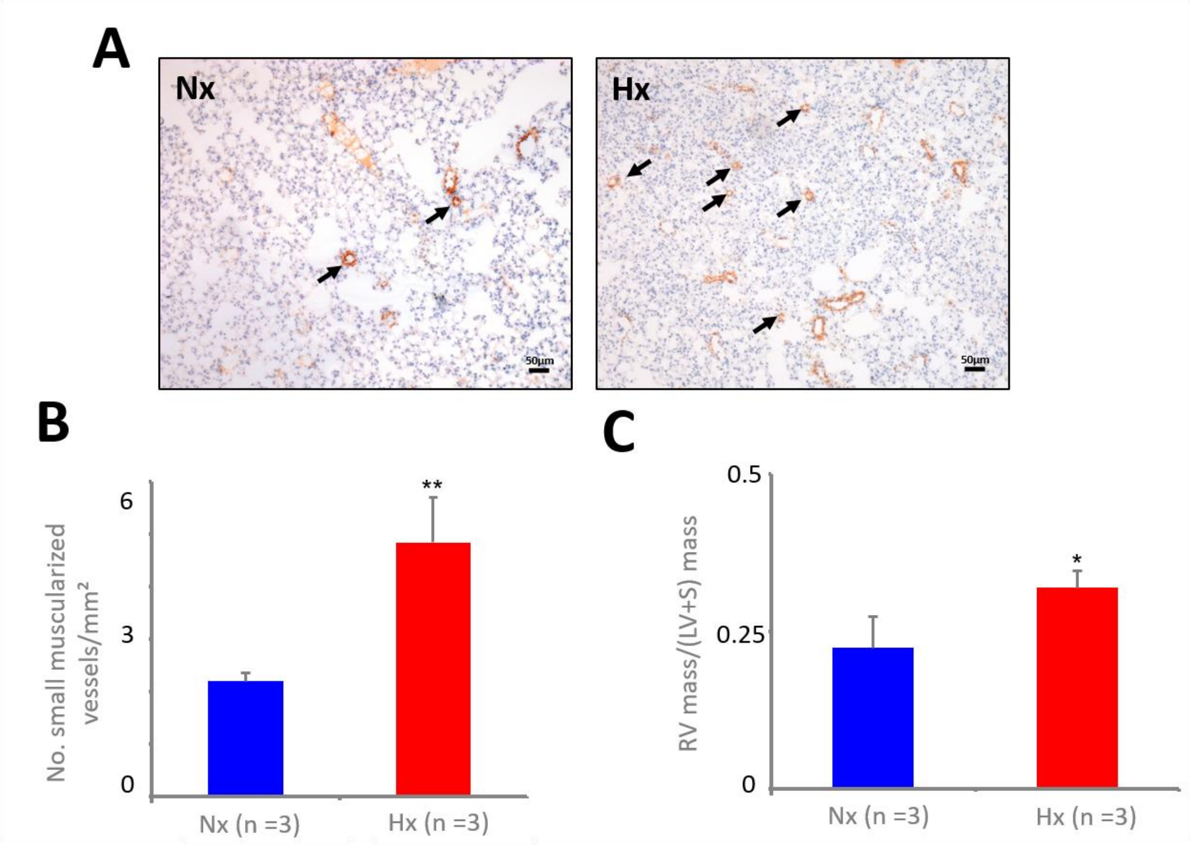

Figure 3.2: Staining for α-smooth-muscle actin of murine lungs. Formalin fixed and paraffin embedded (FFPE) lung sections derived from normoxic (Nx) or hypoxic (Hx) mice were stained for α-smooth-muscle actin and the number of muscularized small vessels (<30 µm) was counted. **(A)** Small muscularized vessels are indicated with arrows. **(B)** Graph shows the number of small muscularized vessels per mm^2 lung tissue, assembled from three regions of interest per lung (n=3, **p<0.01 Hx vs. Nx). (C) The Fulton index as measure of right ventricular hypertrophy was determined as ratio between mass of the right (RV) and left ventricle (LV) with septum (S) (n=3, *p<0.05 Hx vs. Nx).

The cycle length lasts for approximately 430 ms, by which ventricular activity is primarily in diastole (D). The irregular cycles are also clearly visible in the supplementary videos of the reconstructed VOT image sequences available in the on-line version of the journal. Figure 3.3D shows the short-time Fourier transform (STFT) analysis carried out on image data from a hypoxia-treated murine model revealing multiple irregularities throughout cycle length. By calculating the frequency spectra of the time profiles as a function of time, the STFT facilitates detecting changes of heart rate over time, corresponding to arrhythmic events as areas of lower frequencies of the time-series (Figure 3.3D). The green arrows in Figure 3.3D represent irregular cycles, while the white dashed lines indicate breathing periods. The profile in Figure 3.3D show that the peaks of normal contractions before and after arrhythmic events follow a defined periodicity, which further suggests failure in atrio-ventricular conductivity.

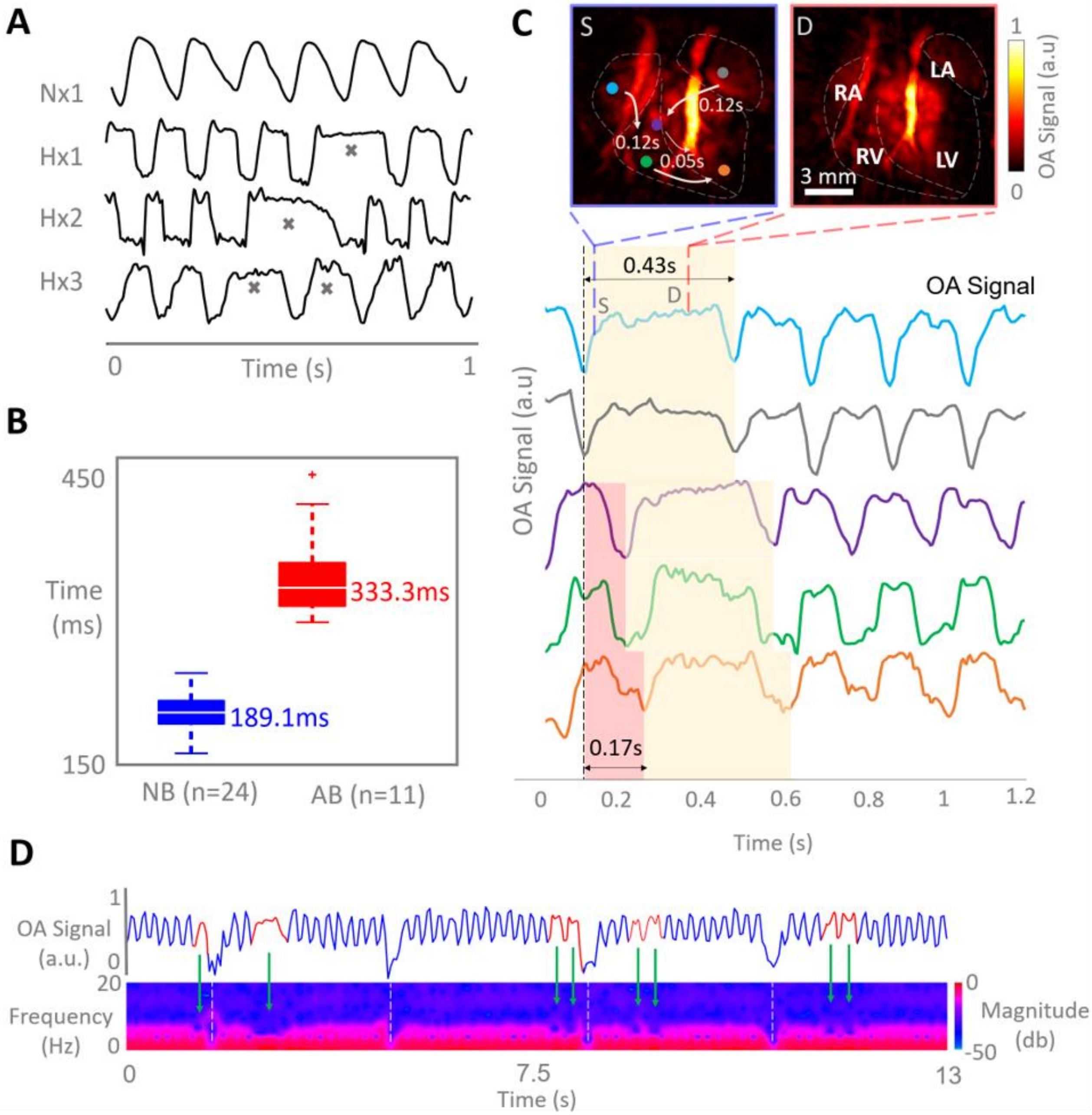

Figure 3.3: Optoacoustic characterization of impaired heart function in hypoxic models. (A) Examples of time-lapse optoacoustic signal intensity profiles for selected voxels in the heart of normoxic and hypoxic mice (n=4). Irregular heart beating events are marked with grey crosses in the time traces for hypoxic models. **(B)** Boxplots of the measured cycle period for normal versus abnormal beating cycles (NB - normal beating, AB - abnormal beating). **(C)** Volumetric mapping of the heart mechanical motion and onsets of the irregular beats, where the colored circles in the heart in systolic phase (S – blue box) correspond to the colored OA signal profiles below. The red shade in the profiles indicate heartbeat onset at varying locations and the yellow shade indicates the duration of the heartbeat. The diastolic phase of the heart (D-red panel) is the heart phase present for the majority of the heartbeat (RA – right atrium, LA, left atrium, RV – right ventricle, LV – left ventricle, S-systole, D-diastole). **(D)** Short-time Fourier transform (STFT) of the temporal OA signal profile in a selected voxel in hypoxic heart, where blue indicates normal beating periods and red indicates irregular beating periods. Green arrows identify the areas of abnormal beat periods in the time series and the areas of low frequency acquired from STFT. White dashed lines indicate breathing events.

3.5 Discussion

Pre-clinical animal models are commonly used to investigate the pathophysiology of pulmonary hypertension and potential therapeutic interventions. Exposure to chronic hypoxia over 3 weeks characteristically leads to pulmonary hypertension in mice. To this end, pre-clinical assessment of PH has been largely limited to *ex vivo* or invasive procedures that interfere with the integrity of the heart tissue, hampering an accurate assessment of heart function within an intact living organism. Development of new imaging approaches is thus crucial for comprehensive understanding of the scope of PH in an *in vivo* environment.

In this study, we have examined the potential of VOT for assessing *in vivo* heart function in murine models of chronic-hypoxia-induced PH. The high temporal resolution of the imaging system enables tracking fast perfusion of contrast agents and estimation of the pulmonary transit time (PTT), a valuable capacity for functional assessment of the heart and pulmonary circuit dynamics. PTT has previously been shown to serve as an accurate indicator of heart performance, specifically left ventricular performance under pathophysiological conditions in the murine heart (Lin et al., 2017). In this study, we have shown that the PTT in murine models exposed to chronic hypoxia was considerably longer than in normoxic models. As the PTT is determined by cardiac function and pulmonary hemodynamics, these findings point to deteriorated cardio-pulmonary function in response to chronic hypoxic conditions. In fact, as indicated in this study, chronic hypoxia results in pulmonary vascular remodelling and right ventricular hypertrophy. This has not only been associated with an increase in pulmonary vascular resistance and right ventricular pressure due to increased afterload in chronic hypoxic mice (Chalupsky et al., 2015; Z. Zhang et al., 2019), but has also been associated with a decreased ability of conductance vessels to store and deliver the entire stroke volume of the right ventricle and ultimately resulting in a loss of pulmonary flow during diastole (Stenmark et al., 2006). PTT values (or CPTT - Cardiopulmonary Transit Times) have been previously studied in humans by using the first pass radionuclide cardiography technique (Zavorsky, Walley, & Russell, 2006). In support of our studies on hypoxia-induced PH in mice, longer PTT values were shown in patients with pulmonary hypertension (Skrok et al., 2012; Y. W. Wu et al., 2017). PTT is becoming increasingly recognized as an important marker for cardiopulmonary function, where very recent studies have been evaluating the PTT in patients using MRI and US (Monahan et al., 2019). At present, pulmonary hypertension in mice is mostly characterized by invasive measurement of right ventricular pressure, and ex vivo histopathological analysis of pulmonary and cardiac tissues. Very recently, MRI and US has been applied to evaluate pulmonary hypertension in the more severe hypoxia/Sugen5416 murine model by measuring right ventricular ejection fraction (Breen, Scadeng, Lai, Murray, & Bigby, 2017) However, in mice PTT was only determined invasively using microangiography (Sonobe et al., 2011). VOT enables measuring the PTT *in vivo* in mice, thus offering a new efficient and non-invasive tool to monitor heart remodelling and pulmonary circuit dynamics in models of pulmonary hypertension.

Arrhythmic events, in particular atrial fibrillation or flutter have been frequently observed in patients with pulmonary hypertension or COPD (Hanrahan et al., 2008). However, heart rate or arrhythmia have not been well documented in the adult chronic hypoxia murine model. Here we show that irregular heart cycles were present in mice exposed to chronic hypoxia as detected in the time profiles of the VOT data that represented mechanical motion of the heart in three dimensions. Although actual blood pressure values cannot be extracted from the VOT data, the non-invasively recorded OA signal intensity changes extracted at given spatial locations, plotted similar patterns to pressure waveforms usually extracted via catheterization (Kern, Donohue, Bach, & Aguirre, 1992). This is expected considering that pressure changes in the heart chambers induce a displacement or strain in the heart walls, which are easily detectable in the OA signal intensity profiles. In catheterization procedures, pressure waveforms can only be measured at a specific location of the heart, which generally hinders measuring the delays between mechanical activation across different heart regions. With the suggested VOT approach, the OA signal intensity changes can be simultaneously obtained from multiple locations in the heart, which enables readily identifying such delays and could serve as an alternative method to strain imaging which also maps mechanical activation across the heart. The preliminary results presented here on cycle variability have promoted future studies on this topic using VOT in order to fully understand the effect of chronic hypoxia on the electromechanical activity of the heart, where ECG and VOT data would be directly compared.

In conclusion, *in vivo* simultaneous detection of two impaired heart functions have been demonstrated with VOT in the murine model of chronic-hypoxia-induced pulmonary hypertension. The PTT and heart rate were both altered in hypoxic hearts compared to normoxic hearts. Overall, VOT has been suggested as a method offering new capabilities for *in vivo* volumetric beat-by-beat characterization of cardio-pulmonary function in murine models of pulmonary hypertension, not attainable with existing approaches.

4. Real-time volumetric assessment of the human carotid artery: hand-held multi- spectral optoacoustic tomography

Published in Radiology, 2019 12th February; 291(1):45-50. DOI:10.1148/radiol.2019181325

Authors

Ivana Ivankovic [1,2,3,4], Elena Merčep [3,4], Claus-Georg Schmedt [5] , Xose Luís Deán-Ben [1,2,3,4], and Daniel Razansky [1,2,3,4]

[1]Faculty of Medicine and Institute of Pharmacology and Toxicology, University of Zurich, Switzerland

[2]Institute for Biomedical Engineering and Department of Information Technology and Electrical Engineering, ETH Zurich, Switzerland

[3]Institute for Biological and Medical Imaging, Helmholtz Center Munich, Neuherberg, Germany

[4]Faculty of Medicine, Technical University of Munich, Germany

[5] Department for Vascular Surgery, Diakonie-Klinikum Schwäbisch Hall, Germany

No conflict of interest disclosed

4.1 Summary Statement:

This study investigates whether volumetric multi-spectral optoacoustic tomography (vMSOT) can provide three-dimensional assessment of anatomical and functional status of the entire bifurcation area of the human carotid artery non-invasively and in real time.

4.2 Implications for patient care:

The study suggests the future potential of using OA imaging for the diagnosis of carotid artery diseases, e.g. for characterizing vulnerable plaques in humans.

The non-invasive nature of optoacoustics further indicates its applicability as a screening platform in asymptomatic patients, where biomarkers measured in the images can potentially be clinically relevant.

4.3 Abstract

Multispectral optical imaging has the capability of resolving hemoglobin, lipid, and water. Volumetric multispectral optoacoustic tomography (MSOT) is a hybrid imaging technique that provides a unique combination of functional and molecular contrast with real-time handheld imaging. The aim was to investigate whether volumetric MSOT can provide real-time assessment of the anatomic and functional status of the human carotid artery bifurcation noninvasively. Imaging of healthy volunteers ($n = 16$) was performed with a custom-designed handheld volumetric MSOT scanner capable of high-spatial-resolution (approximately 200 μm) and real-time (10 volumes/sec) three-dimensional imaging,
while further providing spectroscopic capacity through fast tuning of the excitation light wavelength. For comparison and anatomic cross-validation, volunteers were also scanned with clinical B-mode US. Volumetric MSOT achieved real-time imaging and characterization of the entire carotid bifurcation area across three dimensions simultaneously captured in a single volumetric image frame. Analysis of the acquired data further showed that a higher
contrast-to-noise ratio can be achieved for wavelengths corresponding to a high optical absorption of oxygenated hemoglobin. The human carotid artery was visualized by using handheld volumetric multispectral optoacoustic tomography. This imaging approach is less prone to motion artefacts than are the conventional clinical imaging methods, holding promise for providing additional image-based biomarkers for noninvasive label-free assessment of carotid artery disease.

4.4 Introduction

Most ischemic strokes are associated with carotid artery disease originating from the bifurcation area (Fairhead & Rothwell, 2005b; Mughal et al., 2011). Methods for visualizing human carotids include duplex US (Jahromi, Cinà, Liu, & Clase, 2005), CT (Josephson et al., 2004), and MRI (Cai et al., 2005). However, rapid characterization of tissue function and molecular composition is limited with these modalities. Recently, intravascular optical imaging approaches assisted with smart fluorescence molecular agents have demonstrated powerful performance in detecting specific atherosclerotic biomarkers, including inflammation, protease upregulation, lipid content in areas of high endothelial permeability, and vascular cell adhesion molecules (Jaffer et al., 2011, 2007; Kaul & Lindner, 2004; Vinegoni et al., 2011). Yet fluorescence-based methods can at best provide a qualitative indication of the existence of biomarker activity, rather than an accurate assessment of its biodistribution.

Optoacoustic imaging provides unique opportunities for accurate diagnostics and assessment of carotid artery disease. To this end, the technique has been used in diverse angiographic applications and enabled multiscale imaging of vascular structures ranging from capillaries to major vessels, including cross-sectional (two-dimensional) carotid imaging, at depths of several millimeters to centimeters in living tissues (X. L. Deán-Ben et al., 2017; Xosé Luís Deán-Ben & Razansky, 2013; Dima & Ntziachristos, 2012). Multispectral optoacoustic tomography (MSOT) can further provide valuable functional information by spectroscopically identifying the presence of specific tissue chromophores and extrinsic agents (Mandal, Deán-Ben, Burton, & Razansky, 2015) or evaluation of physiologic conditions with label-free mapping of blood oxygen saturation in tissues (Tzoumas et al., 2016). MSOT imaging of matrix metalloproteinase activity, typically associated with atherosclerotic plaque instability, has been demonstrated in ex vivo human carotid plaque samples (Razansky et al., 2012). By using excitation in the wavelength range of 1210 nm, corresponding to the peak optical absorption by lipids, optoacoustic imaging could clearly identify and characterize plaques within human aorta and carotid artery samples ex vivo (Allen et al., 2012; Kruizinga et al., 2014).

The goal of this study was to investigate whether optoacoustic imaging can be used clinically to provide three-dimensional assessment of anatomic and functional status of the entire bifurcation area of the human carotid artery noninvasively and in real time, thus addressing limitations of the existing imaging approaches used for the characterization of carotid artery disease.

4.5 Materials and Methods

We devised a handheld volumetric MSOT system to enable noninvasive, real-time, three-dimensional visualization of human carotids (Figure 4.1A). It features spherical array detection geometry with nearly isotropic three-dimensional resolution of 200 µm (X. Luís Deán-Ben & Razansky, 2013), wide tunability of the excitation light in the range of 680–950 nm, and parallel data acquisition for real-time imaging at a volumetric frame rate up to 100 Hz. The laser further features a separate output delivering the fundamental pumping wavelength of 1064 nm. The detection array was attached to a holder containing a liquid acoustic coupling medium (water) sealed with a transparent membrane (Figure 4.1A). The images were rendered in a volume of 20 × 20 × 20 mm^3 (200 × 200 × 200 voxels) and then cropped along the depth (or z) axis for better visualization of the carotid artery. Graphics processing unit–based implementation of the reconstruction procedure allowed for a live preview of the three-dimensional optoacoustic images (Dean-Ben et al., 2013). All processing steps were performed in Matlab (version 9.1, R2016b; MathWorks, Natick, Mass). Image visualization and analysis were performed in Amira (Zuse Institute, Berlin, Germany).

For this preliminary study, no institutional review board approval was required as set out for noninterventional human studies by the German Drug or Medical Device Act. Healthy volunteers consisting of female and male researchers (age range, 22–44 years) with no history of cardiovascular diseases were recruited between April 2017 and November 2018. Written informed consent was obtained from all volunteers. Exclusion criteria were physical or mental conditions inhibiting volunteers from making informed judgements, history of cardiovascular disease, pregnancy, or breastfeeding. The final cohort consisted of 16 healthy volunteers with mean age ± standard deviation of 29.75 years ± 5.55 (nine of 16 [56.25%] women with mean age of 28 years ± 2.66; seven of 16 [43.75%] men with mean age of 32 years ± 7.23). All volunteers consented to be imaged with the handheld volumetric MSOT probe in full accordance with the work safety regulations of the Helmholtz Centre Munich (Neuherberg, Germany).

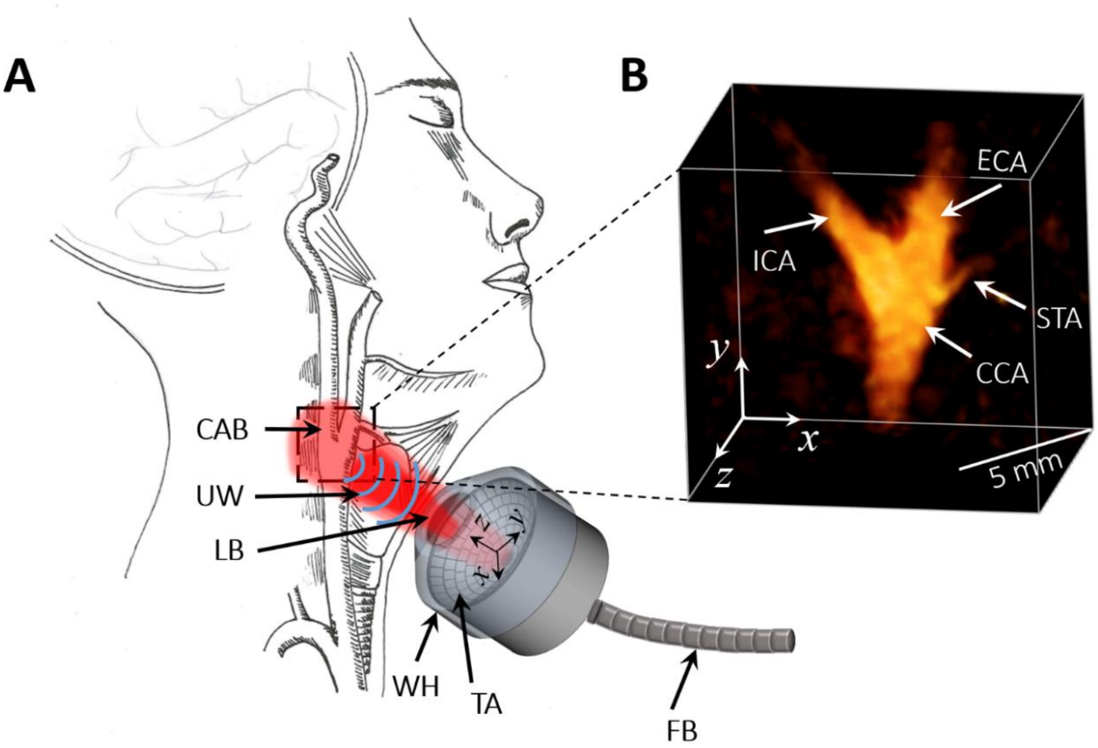

Figure 4.1: Images show volumetric multispectral optoacoustic tomographic (MSOT) imaging setup. *A*, Diagram illustrates handheld noninvasive scanning procedure, where volumetric MSOT probe is scanned on skin surface around carotid artery bifurcation area. *B*, Three-dimensional view of reconstructed volumetric MSOT image of carotid bifurcation captured at video rate of 10 Hz in a 44-year-old man. CAB = carotid artery bifurcation, CCA = common carotid artery, ECA = external carotid artery, FB = fiber bundle, ICA = internal carotid artery, LB = laser beam, STA = superior thyroid artery, TA = transducer array, TM = transparent membrane, UW = ultrasound waves, WH = water holder.

The pulse repetition rate of the laser was set to 10 Hz while the maximal light fluence on the skin surface was maintained below 20 mJ/cm^2 in the range of 730–900 nm and below 50 mJ/cm^2 at 1064 nm to fulfill the safety exposure limits (ANSIZ136.1, 2014) for nanosecond laser radiation in the entire wavelength range used in our experiments. All volunteers were imaged at wavelengths of 850 nm and 1064 nm for optimal visualization of the carotid artery. Five volunteers (three women [60%] with mean age of 26.6 years ± 3.3; two men [40%] with mean age of 40.5 years ± 3.5) were also imaged between 730–900 nm for multispectral evaluation. The acquired volumetric MSOT images of two volunteers (two women with mean age of 28.5 years ± 2.5) were further compared against state-of-the-art clinical US (Logiq S8; GE Healthcare, Wisconsin) obtained with 11L linear transducer (GE Healthcare) carried out by an experienced vascular surgeon (C.G.S.).

4.6 Results

No unpleasant sensations were reported during or after the imaging sessions. The skin area was also carefully examined for any unexpected damage immediately after the sessions. No adverse effects were reported within 1 month following the scanning procedures.

We first examined the general feasibility of identifying the carotid artery bifurcation with the handheld volumetric MSOT imaging probe. Figure 4.1B shows a perspective view of the three-dimensional tomographic reconstruction of this area acquired at a single wavelength of 850 nm from a healthy volunteer. Figure 4.2A shows the coronal and sagittal views color coded with depth, revealing the skin surface (red and orange), the closest carotid wall at a depth of 5–7 mm (green), and the deeper wall at a depth of 16 mm (blue). The optoacoustic signal is mainly generated by whole blood (haemoglobin) at the periphery of the vessel lumen, which allowed for clearly distinguishing the carotid walls (see *CW* in Figure 4.2A). The top maximum intensity projection of the captured image volume is displayed in Figure 4.2B, where superficial structures were removed so that the entire anatomy of the carotid bifurcation area is more clearly visible.

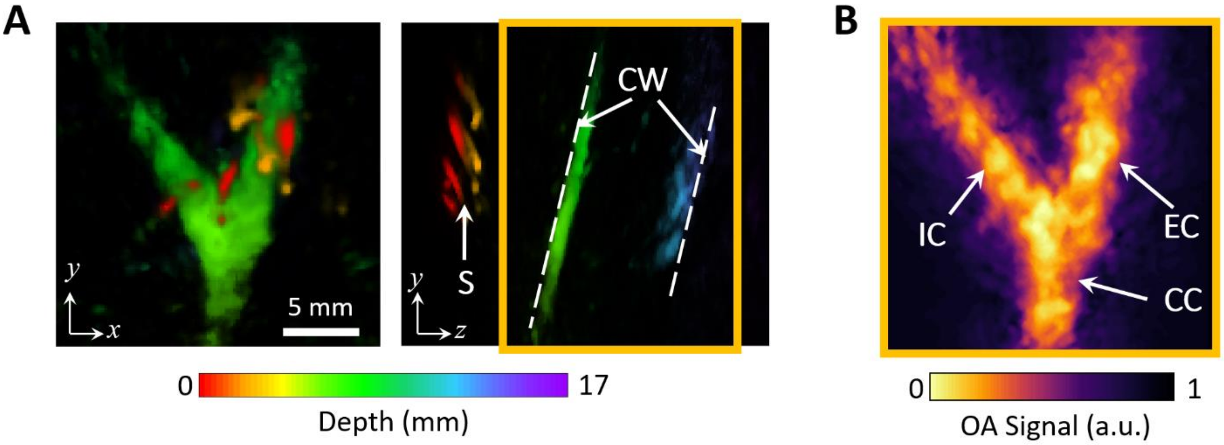

Figure 4.2: (A, B) Noninvasive volumetric multispectral optoacoustic (OA) tomographic anatomic imaging of carotid artery bifurcation in vivo in a 44-year-old man. (A) Image shows depth characterization. Maximum intensity projections (MIPs) of volumetric reconstructions along *z* and *y* directions are color coded to represent depth (in millimeters), where structures in red identify superficial contrast and blue and purple are indicative of deeper structures. (B) MIP of volumetric reconstruction of carotid bifurcation after removal of contrast arising from shallow structures. Orange box in A indicates depth range used for rendering MIP in B. CC = common carotid, CW = carotid wall, EC = external carotid, IC = internal carotid, S = skin.

We further scanned an extended area spanning 45 mm along the common carotid and bifurcation by using illumination wavelength of 1064 nm. The multiple image volumes were subsequently stitched by means of a spatial compounding technique (Nitkunanantharajah, Hennersperger, Dean-Ben, Razansky, & Navab, 2018) to render the carotid anatomy at a larger scale (Figure 4.3). The scanning procedure can be best visualized in Movie E1 (online), showing three-dimensional views of the carotid bifurcation along with the common carotid artery, internal carotid artery, and external carotid artery in a single imaging session. Figure 4.4 summarizes optoacoustic signal decay against carotid depth in all the 16 volunteers measured at wavelengths of either 850 nm or 1064 nm. Detectable signals with signal-to-noise ratio greater than 8 dB were recorded from the carotid up to a depth of 16 mm.

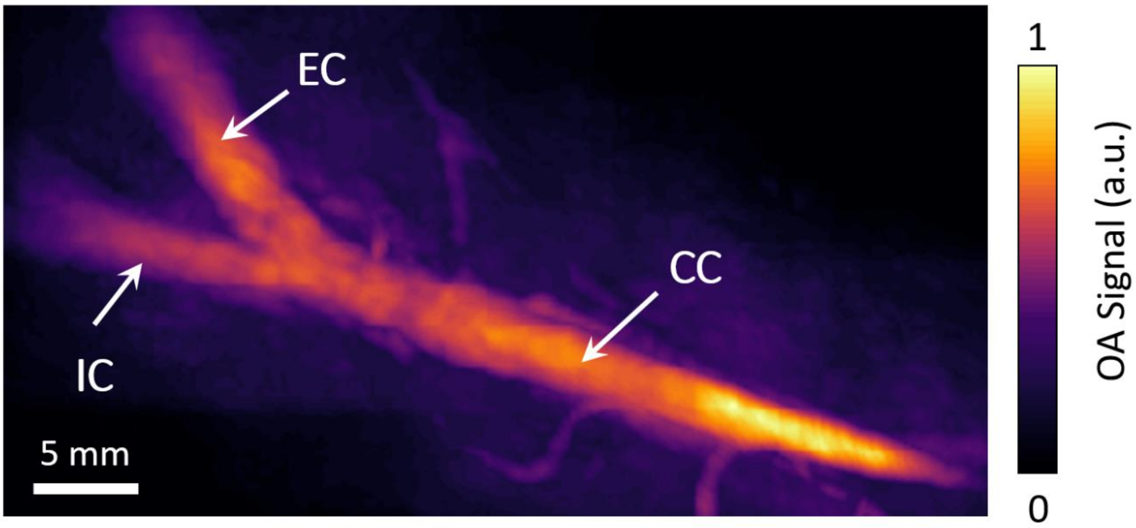

Figure 4.3: Compounded image of handheld volumetric multispectral optoacoustic (OA) tomography scan along entire carotid artery in a 26-year-old woman. CC = common carotid, EC = external carotid, IC = internal carotid.

Anatomic features resolved with the volumetric optoacoustic scans were validated against US images recorded from two female volunteers (mean age, 28.5 years) by using the clinical B-mode scanner (Figure 4.5). Although the entire carotid bifurcation area could be readily visualized with the volumetric MSOT owing to its three-dimensional imaging capabilities, it was not easily discernable in single cross-sectional US images. For instance, whereas US visualization of the whole carotid bifurcation in a single cross-section (Figure 4.5A) required an extended acquisition time to find the suitable orientation of the US probe, a similar view could readily be obtained from the three-dimensional optoacoustic image.

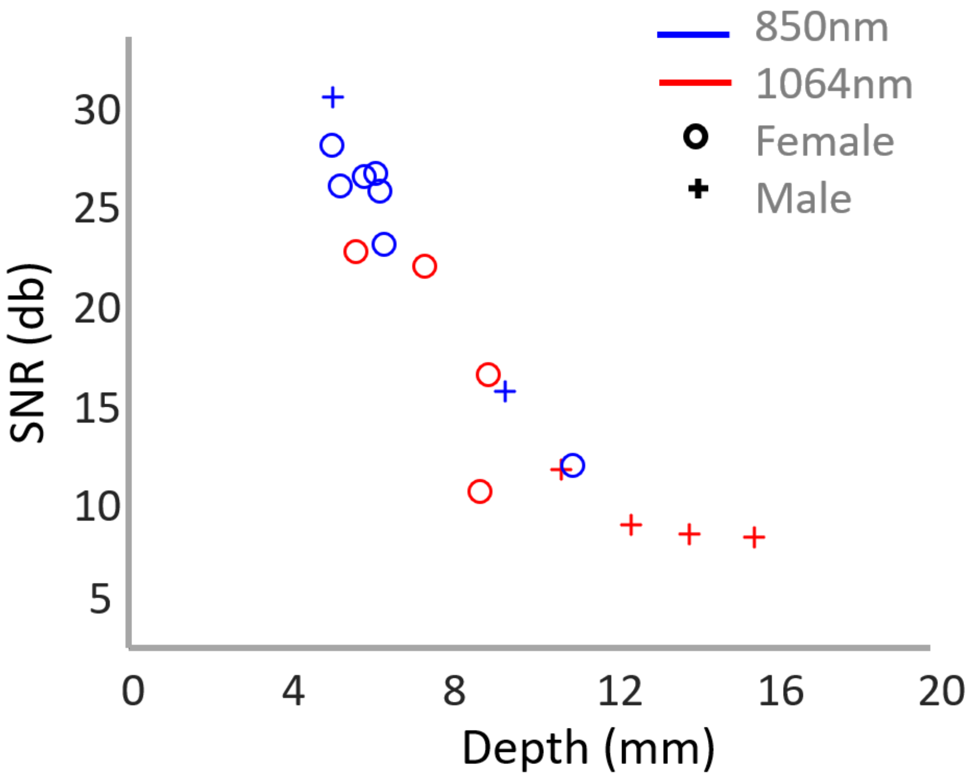

Figure 4.4: Graph shows signal-to-noise-ratio (SNR) of optoacoustic signal recorded noninvasively from superficial carotid wall and plotted against its depth in 16 volunteers. Measurements were performed at wavelength of either 850 nm (seven women [77.7%] with mean age ± standard deviation of 28.28 years ± 2.05; two men [22.22%] with mean age of 40.5 years ± 3.5) or 1064 nm (four women [50%] with mean age of 27.25 years ± 1.92; four men [50%] with mean age of 30 years ± 4.18).

Multispectral data were subsequently acquired from five healthy volunteers (three women [60%] with mean age of 26.6 years ± 3.3; two men [40%] with mean age of 40.5 years ± 3.5) at wavelengths of 730 nm, 760 nm, 800 nm, 850 nm, and 900 nm, as shown in Figure 4.6A. Note that the generated optoacoustic signal is affected by the wavelength-dependent light attenuation in tissues, which can be estimated by considering the hemogblobin absorption spectra (Figure 4.6B) (Xosé Luís Deán-Ben, Bay, & Razansky, 2014). From a theoretical standpoint (Jacques, 2013), for average tissue oxygenation values below 75%, such effective attenuation is expected to peak at 760 nm while having a local minimum at 800 nm (Figure 4.6C).

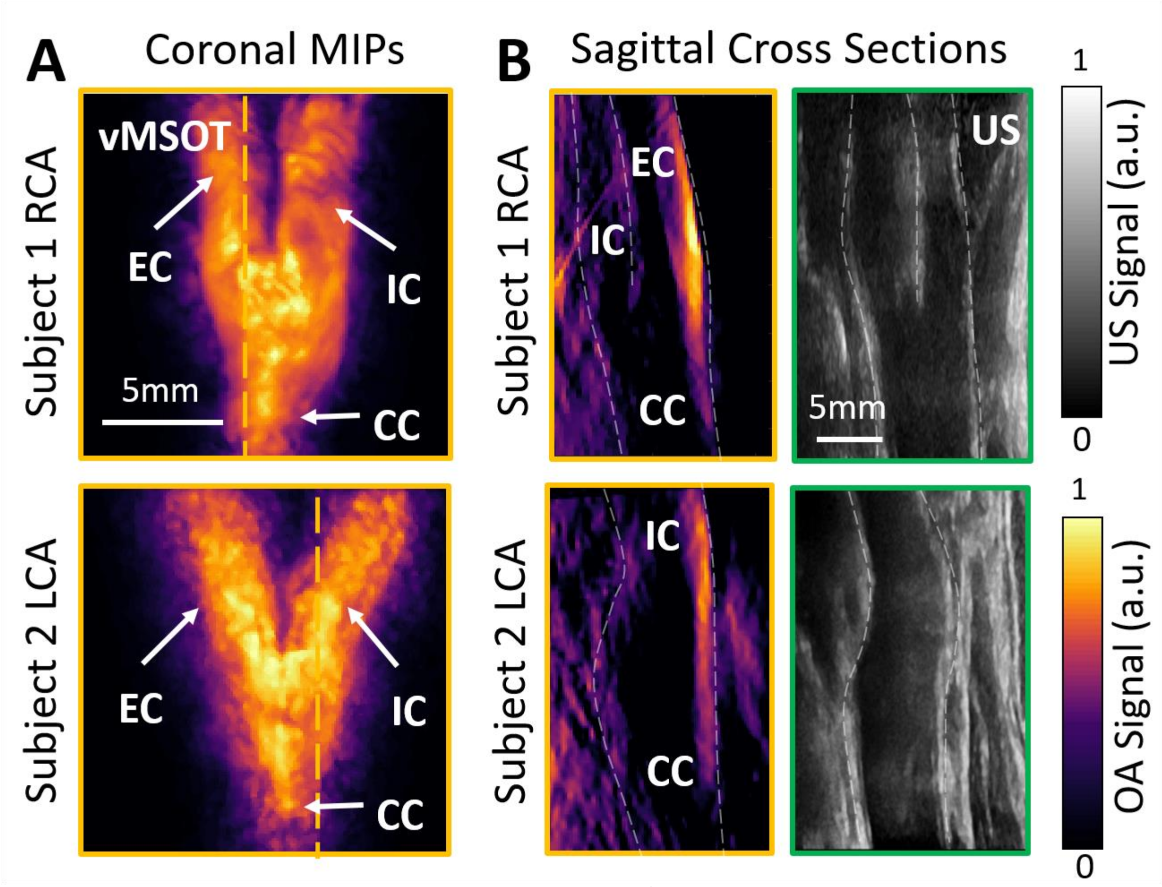

Figure 4.5: Images show qualitative comparison of image quality between volumetric multispectral optoacoustic tomographic (hereafter, vMSOT) and B-mode US in two volunteers. Right carotid artery (RCA) and left carotid artery (LCA) are shown in a 31-year-old woman (subject 1) and in a 26-year-old woman (subject 2), respectively. *A*, vMSOT images of carotid artery bifurcation in coronal view represented in maximum intensity projections (MIPs). *B*, vMSOT and B-mode US images of carotid bifurcation in sagittal cross-sectional views. Orange and green frames correspond to vMSOT and US images, respectively, where orange dashed lines in *A* indicate section shown in *B*. CC = common carotid, EC = external carotid, IC = internal carotid, OA = optoacoustic.

It was observed that the attenuation peak at 760 nm results in a local minimum in signal (and subsequently in contrast-to-noise ratio) at this wavelength for most volunteers (n = 5), whereas a contrast-to-noise ratio peak was observed at 800 nm for some of the volunteers, arguably due to the reduced attenuation at this wavelength. It is important to consider that the optoacoustic spectrum of the carotid artery is influenced by additional factors such as the depth at which the artery is located and the presence of veins or other highly absorbing structures in the surrounding tissue. Indeed, optical properties in biologic tissues are generally heterogeneous and difficult to estimate, which hampers accurate quantification of sO_2 in vascular structures. Overall, images at longer excitation wavelengths exhibit higher contrast-to-noise ratios owing to the high oxygen saturation of the arterial blood and the corresponding trend in the oxygenated hemoglobin absorption spectrum. The measured contrast-to-noise ratio of the images in the range of 800–900 nm has a mean value of 18.8 dB ± 4.28 while having lower values of 9.18 dB ± 3.8 for shorter wavelengths of 730–760 nm (Figure 4.6E).

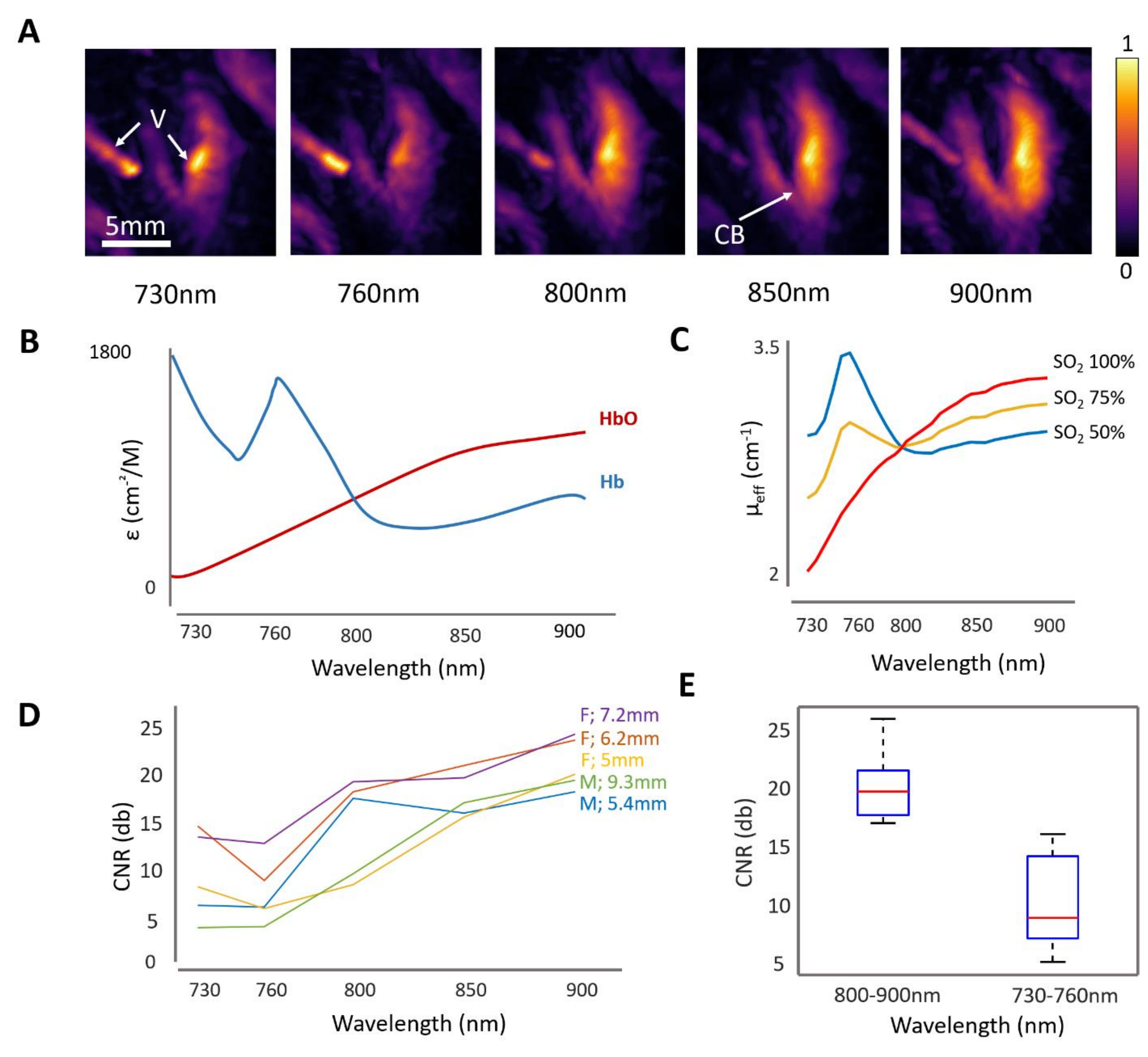

Figure 4.6: Multispectral and CNR analysis (A) Volumetric multispectral optoacoustic (OA) tomography images show right carotid artery bifurcation in a 23-yearold woman taken in wavelength range of 730–900 nm. (B) Graph shows spectral dependence of optical absorption by oxygenated hemoglobin (HbO) and deoxygenated hemoglobin (Hb). (C) Graph shows simulated wavelength-dependent effective light attenuation coefficient of average soft living tissue. (D) Graph shows contrast-to-noise ratio (CNR) of images as function of wavelength including five volunteers (three of five [60%] women with mean age 6 standard deviation of 26.6 years 6 3.3; two of five [40%] men with mean age of 40.5 years 6 3.5). (E) Graph shows statistical difference of CNR was calculated for longer wavelengths (800–900 nm) and shorter wavelengths (730–760 nm) (*p* < 0 .001, *T* test). CB = carotid bifurcation, F = female, M = male, V = vein.

4.7 Discussion

A study was carried out to assess capabilities of the handheld volumetric multispectral optoacoustic tomography (MSOT) approach for noninvasive characterization of healthy human carotid arteries. Optoacoustic vascular imaging is associated primarily with optical absorption of blood, whose oxygenation status is spectrally distinguished through a multiwavelength imaging approach. The handheld volumetric MSOT imaging probe was devised to optimize performance of carotid imaging at centimeter-scale depths and to provide an effective field of view of approximately 2 cm^3 in real time, with the ability to scan further around the area with handheld translation of the probe. The depth of the field of view effectively captured by the transducer with respect to the skin can easily be adjusted by changing the volume of the acoustic coupling medium, up to a maximum depth of approximately 30 mm. This is generally sufficient to visualize the carotid bifurcation area in most patients. Light attenuation may eventually be the main factor to limit the achievable depth, even if the transducer can potentially be redesigned to be sensitive to deeper regions.

We focused on exploiting the above advantages of volumetric MSOT for imaging the carotid bifurcation, an important reference point for atherosclerotic vascular disease. Multispectral imaging was further carried out in the near-infrared window with the best image contrast from the carotid artery achieved at 1064 nm and the 800–900-nm range due to an increase of the extinction coefficient of oxygenated haemoglobin for longer wavelengths and the low light attenuation by tissues in this range. Better visibility of deeper arteries was achieved with the 1064-nm excitation, which can be ascribed to the higher per-pulse energy of the laser and weaker light attenuation at this wavelength. The spectroscopic differentiation capacity is needed for identification of other carotid artery disease biomarkers, as well as extrinsically administered targeted or activatable labels (Razansky et al., 2012). Efforts in carotid plaque imaging are also geared toward noninvasive detection of vulnerable lipid-rich plaques (Finn et al., 2010; Kruizinga et al., 2014). In this context, optoacoustic lipid detection at 1200 nm has already been demonstrated ex vivo and in preclinical intravascular studies in vivo (Allen et al., 2012; Jansen, Van Soest, & van der Steen, 2014; Kruizinga et al., 2014). Thus, the suggested handheld volumetric MSOT approach holds promise for rapid volumetric assessment and spectroscopic characterization of the carotid artery and plaque vulnerability in a non-invasive manner. Multispectral imaging at a more extended spectral range with proper selection of wavelengths within a broader range of 650–1250 nm can enable resolving haemoglobin, lipid, and water contributions in the optoacoustic images. To detect vulnerable plaque, the carotid artery must first be anatomically identified in single-wavelength images (eg, at 1064 nm) and once located, multispectral imaging at around 1200 nm may help to further identify lipid content, which represents a key factor in vulnerable plaques.

The real-time three-dimensional imaging capacity of volumetric MSOT presents a key advantage of the suggested handheld imaging approach pertaining to visualization of the carotid anatomy, including the common carotid artery, internal carotid artery, and external carotid artery that are simultaneously captured in a single volumetric image frame. The technique allows three-dimensional volume rendering with a single laser shot without signal averaging or probe scanning. This decreases motion-related artefacts associated with temporal and spatial blurring. In contrast, clinical US diagnostics typically rely on two-dimensional cross-sectional views where multiple alternations between the transverse and sagittal planes are necessary for comprehensive assessment of the entire region of interest.

Several limitations were encountered in this study, among which the most prominent was the lack of patient data. This prevents proper quantification of clinically relevant biomarkers (eg, lipid content) that can only be assessed after studies in patients with carotid artery disease are performed. We also note that US images may provide more detailed anatomic information in some cross-sectional views, with the underlying reason being the fundamentally different contrast delivered by the two modalities. Optoacoustics also have generally lower penetration depth due to strong light attenuation in living tissues, which may have contributed to the lack of detail from deeper tissues layers. In particular, strong light absorption by whole blood may impose additional visibility constraints (Xosé Luís Deán-Ben & Razansky, 2016)when imaging large blood vessels such as the carotid artery. The unique real-time volumetric imaging capacity of optoacoustics can potentially be integrated with US for a more comprehensive characterization of the carotid artery by means of a hybrid imaging probe, as was recently shown for the two-dimensional imaging case (Merčep, Deán-Ben, & Razansky, 2018).

In summary, these results demonstrate the potential of volumetric multispectral optoacoustic tomography (MSOT) for spectroscopic volumetric characterization of the carotid artery in a non-invasive, real-time, and handheld manner. Volumetric MSOT is less prone to motion artefacts than are the conventional imaging methods used in clinical practice. Spectroscopic optoacoustics have the potential for label-free identification and assessment of clinically relevant biomarkers. As a result, volumetric MSOT holds promise for non-invasive functional assessment of cardiovascular disease.

5. Outlook

Cardiovascular disease is an ongoing worldwide threat, persistently challenging clinicians, scientists and the economy. This highlights the need for continuous research in all aspects of CVD, from basic to translational approaches. Biomedical imaging has become an indispensable tool in CVD research as it is a solution to visualise healthy and diseased biological processes *in vivo*, which are otherwise not possible. Optoacoustic imaging is now emerging as a potential key tool in CVD research and CVD diagnostics. Here we show OAT applied both in preclinical and clinical settings to demonstrate its capabilities as a multiscale and multidisciplinary imaging device suitable to the cardiovascular field.

5.1 Murine heart imaging

Imaging of the murine heart has long been challenging due to its small size and rapid heartbeat compared to the human heartbeat. Many studies must rely on histopathological data taken at different time points during the course of the disease. However, the adaptation of clinical US and MRI machines towards a more preclinical environment accounting for smaller size, has accelerated *in vivo* basic research studies and has become instrumental to translational research. Here we have presented a preclinical OAT device, tailored specifically towards the small size of the mouse and its fast heartbeat. Building upon studies where OAT of the heart was first shown in real-time and 3D (Xosé Luís Deán-Ben et al., 2015) along with the extraction of functional parameters such as the PTT, we applied the novel cardiovascular imaging tool to CVD models and explored how OAT can identify characteristics of heart disease by employing its 4D advantages.

5.1.1 Myocardial infarction imaging

Myocardial infarction is highly prominent globally and much of CVD research is focused on post-MI treatment to address myocardial remodelling, which imposes long-term effects on heart function after the MI event. MI varies in many ways, for example, the length of time the coronary artery is occluded, the size of the occlusion, course and speed of treatment and the general health status of the patient. It is thus particularly difficult to model these different scenarios pre-clinically. Yet, it is crucial to explore models mimicking different clinical scenarios to broaden the understanding of myocardial function post

MI. Here we have studied two different surgical models of MI, PO and I/R, and compared both in *wt* mice in addition to exploring the effects of c-kit deficiency in PO models. The results presented in these studies have several implications. Firstly, VOT is capable of detecting differences in myocardial function post MI at a mechanical level (PO vs I/R) and also indirectly at a molecular level (c-kit deficient vs *wt*). Therefore, subtle changes at the cellular level that translate into changes at the organ level are measurable by VOT in addition to visualising the heart *in vivo* and in real-time. Although VOT is not currently feasible for clinical implementation, the findings can still be used as a basis for studies in the clinics. MRI and US imaging of the PTT has recently been shown in humans (Monahan et al., 2019; Shors et al., 2003). An interesting future study would be the assessment of PTT values prior to the MI event, as the lead up to acute MI is a chronic process, beginning as early as childhood (Hong, 2010). However chronic development of atherosclerotic arteries is relevant in human pathophysiology, while mice on the other hand are relatively resistant to plaque formation in coronary arteries, thus making it challenging to model a highly relevant clinical scenario in mice (von Scheidt et al., 2017). However, there are atherosclerotic mouse models that encompass human risk factors, such as modified versions of the ‘western diet’ in addition to the more common genetic knockout atherosclerotic models. All in all, the mouse models have been indispensable to translational CVD research, even though direct comparisons sometimes cannot be made (Lee et al., 2017).

The past few decades have seen increased efforts for stem cell regeneration as a treatment method for MI. Promising results in preclinical settings were accelerated into the clinical trials, however produced inconsistent results leading to a reduction of myocardium regeneration attempts in the cardiac stem cell field (Zhou & Wu, 2018). However, it is still important to further investigate the field of research. Instead of addressing these questions directly at the molecular level, we explored a model deficient in the tyrosine receptor kinase, c-kit, and indirectly assessed the effects of the lack of c-kit on myocardial function post MI. The results supported the concept that cardiac progenitor cells are involved in myocardial healing post MI, whereby VOT was capable of detecting effects of molecular and genetic changes at the organ level. However, the translatability of these results into the clinics still remains unclear and more studies must be carried out. For example, contrast agents targeting specific cardiac stem cell markers could help delineate their pathway following MI. Given that the contrast agents would be designed for OA imaging, VOT could become a key player as an *in vivo* imaging system used to answer the unresolved CVD questions.

5.1.2 Pulmonary hypertension imaging

We have shown the capability of VOT being used as a pre-clinical imaging device to study murine models of myocardial infarction. However, in order to establish VOT as a CVD pre-clinical imaging modality, it was vital to be tested in other heart disease models. Here we used VOT to assess heart function in chronic hypoxic models, where models under chronic hypoxic conditions presented impaired heart function compared to control mice under normal conditions. Having used the same experimental methods and analytical parameters as in MI imaging, we were able to find a strong difference in heart function between the models. These findings strengthen our view that VOT is a suitable and advanced imaging tool to study a variety of diseases. What is further attractive about this study is that it is a multi-systemic study i.e. two major biological systems are being addressed, the cardiovascular and pulmonary systems. The first pathological signs in response to low oxygen levels are initially present in the lungs, followed by secondary pathological events in the heart. It is important to understand how a disease systematically effects the body and VOT could be an ideal imaging device to investigate heart function and how it responds to varying diseases. For example, it is known that heart failure risk is significantly increased in diabetic patients (Rosano, Vitale, & Seferovic, 2016). Therefore, it is possible that VOT can detect early signs of heart failure in diabetic mouse models, which could potentially give rise to new insights into the cardiac-renal interactions.

5.2 Carotid artery imaging

The goal of many developing biomedical imaging technologies is their translation into the clinics for imaging human pathologies. The human body is on a much grander scale compared to small animal imaging, therefore understanding the strengths and limitations of the imaging system is necessary for clinical imaging, in order to focus directly on the clinical question which your device could help answer. For OAT, the main factors to consider are the optical absorbance properties of the tissue and the accessibility of the tissue i.e. depth of ROI. Having assessed these parameters, the carotid artery in its healthy and atherosclerotic state is a prime imaging target for OAT.

Here we have shown a new approach to imaging the CA, in a non-invasive, real-time and volumetric manner. The ease of the handheld scanning capabilities of the probe allow for efficient detection of the CA bifurcation. The entire CA bifurcation can be captured in a single volumetric frame, compared to conventional US where the probe is often switched between longitudinal and axial planes for better understanding of the anatomical location. However, the most promising conclusion of the presented pilot study, is the potential of the OAT handheld probe for stroke prevention. The multispectral nature of OAT allows for rapid wavelength switching while imaging live; therefore, allowing the clinician to firstly locate the CA bifurcation (850-900nm) and rapidly switch wavelengths where lipids absorb light (1200nm) for vulnerable plaque detection. Although the presented work does not demonstrate plaque detection as it was carried out in healthy volunteers, several OA studies have demonstrated unambiguous detection of lipid content within plaque at 1200nm (Allen et al., 2012; B. Wang et al., 2012). The use of OAT as an additional screening modality alongside US could become indispensable to CA screening for stroke prevention. The current gold standard, US and colour Doppler US, are extremely powerful in detecting arterial stenosis. However, characterisation of plaque vulnerability, which is often performed by estimating the echogenicity of the suspected plaque region has high inter-user variability and is an estimation-at-best of the vulnerability of the plaque. OAT can offer an accurate reading as it specifically targets lipid tissue composition. OAT could have the benefit to guide surgical decisions and reduce the number of unnecessary interventions, improving patient safety and decreasing economic burden.

5.3 Future directions

Cardiovascular OAT is on route to becoming recognised as both a pre-clinical small animal imaging platform and a clinical imaging device for CA screening. However, for this to be achieved, a multidisciplinary team is critical. Coordination between engineers, biologists and medical doctors is essential for CVD research, so that unsolved problems can be addressed with novel and advanced technological approaches. Therefore, the future of cardiovascular OAT lies in collaborative efforts between bioengineers and doctors. OAT has a strong potential in becoming a standard pre-clinical tool for imaging models of CVD, especially by focusing on its strength on imaging the murine heart, but in order to do so, more disease models in which heart function is suspected to be impaired are necessary. Future studies with collaborators with expertise in CVD will help push OAT as a standard imaging platform for heart research.

Current studies have been focusing on the optimisation of technical parameters, particularly light delivery through the transducer to the ROI (Figure 5.1A). By increasing the number of fibre bundles from a single-fibre bundle, a larger area can be illuminated thus increasing the FOV (Figure 5.1B). In addition, the larger illuminated area increases the permissible pulse energy level therefore has potential for deeper tissue imaging. Figure 5.1 C&D represent 3D computer aided design (CAD) prototypes of holders for such fibre bundles. The holder is designed in such a way to contain the acoustic coupling while also supporting illumination from the fibre bundles. Multi-fibre illumination has the potential to improve all areas of OAT and is likely to be implemented in many future studies.

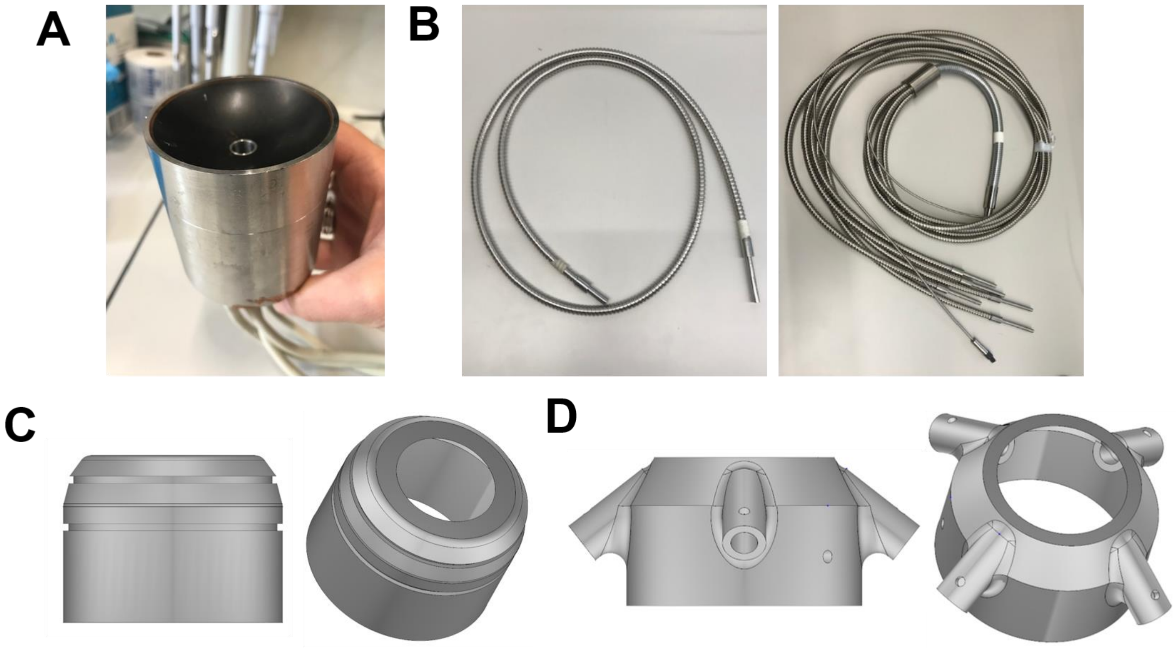

Figure 5.1 Single and multi-fibre designs for illumination. (A) Hemispherical OAT transducer. (B) Single-fibre bundle (left panel), multi-fibre bundle (right panel). (C) CAD prototype of holder for single-fibre use (D) CAD prototype of holder for multi-fibre use. (OAT; optoacoustic tomography, CAD; computer aided design)

OAT as a clinical imaging device is becoming very apparent. In fact, clinical studies to image patients at risk of stroke are currently in the pipeline, using the commercial version of OAT (MSOT Acuity, iThera Medical GmbH). Planned future clinical studies will implement the custom-designed volumetric handheld probe presented in this thesis (Figure 3.1A). Clinical studies for stroke prevention with OAT are now closer to reality, rather than a long-term goal. In addition to imaging of the CA clinically, the handheld OAT system is capable of imaging multiple diseases on a clinical level, including breast cancer, effects of radiation and haemodynamic responses to organ transplants. The increasing number of high impact successful clinical studies (Knieling, 2017; Regensburger et al., 2019) and increasing number of OAT devices located in hospitals globally, will highlight OAT as a clinical imaging device. With continuous technical development and collection of large volumes of clinical data, OAT has the potential to become a standard medical instrument across hospitals in the next few decades.

Overall, OAT has been shown to be an effective imaging device for CVD applications in pre-clinical and clinical research. By utilising its non-invasive, real-time, volumetric and multispectral capabilities, OAT has the potential to become a key cardiovascular imaging tool.

6. References

Akki, A., Gupta, A., & Weiss, R. G. (2013). Magnetic resonance imaging and spectroscopy of the murine cardiovascular system. *American Journal of Physiology-Heart and Circulatory Physiology*, *304*(5), H633–H648. https://doi.org/10.1152/ajpheart.00771.2011

Alander, J. T., Kaartinen, I., Laakso, A., Pätilä, T., Spillmann, T., Tuchin, V. V., … Välisuo, P. (2012). A Review of indocyanine green fluorescent imaging in surgery. *International Journal of Biomedical Imaging*, *2012*. https://doi.org/10.1155/2012/940585

Allen, T. J., Hall, A., Dhillon, A. P., Owen, J. S., & Beard, P. C. (2012). Spectroscopic photoacoustic imaging of lipid-rich plaques in the human aorta in the 740 to 1400 nm wavelength range. *Journal of Biomedical Optics*, *17*(6), 061209. https://doi.org/10.1117/1.jbo.17.6.061209

America, L. I. of. (2007). American National Standard for Safe Use of Lasers. *Laser Institute of America*. Retrieved from papers2://publication/uuid/D2E145A0-6015-4317-895E-3644589A4A40

Arnett, D. K., Blumenthal, R. S., Albert, M. A., Buroker, A. B., Goldberger, Z. D., Hahn, E. J., … Ziaeian, B. (2019). 2019 ACC/AHA Guideline on the Primary Prevention of Cardiovascular Disease: A Report of the American College of Cardiology/American Heart Association Task Force on Clinical Practice Guidelines. *Journal of the American College of Cardiology*, *74*(10), e177–e232. https://doi.org/10.1016/j.jacc.2019.03.010

Bärtsch, P., & Gibbs, J. S. R. (2007). Effect of altitude on the heart and the lungs. *Circulation*, *116*(19), 2191–2202. https://doi.org/10.1161/CIRCULATIONAHA.106.650796

Beard, P. (2011). Biomedical photoacoustic imaging. *Interface Focus*, *1*(4), 602–631. https://doi.org/10.1098/rsfs.2011.0028

Behfar, A., Crespo-Diaz, R., Terzic, A., & Gersh, B. J. (2014). Cell therapy for cardiac repair-lessons from clinical trials. *Nature Reviews Cardiology*, *11*(4), 232–246. https://doi.org/10.1038/nrcardio.2014.9

Bell, A. G., & Ph, D. (1880). *XXXIV.-On*. (118), 305–324.

Bergmann, O., Bhardwaj, R. D., Bernard, S., Zdunek, S., Barnabé-Heider, F., Walsh, S., … Frisén, J. (2009). Evidence for cardiomyocyte renewal in humans. *Science (New York, N.Y.), 324*(5923), 98–102. https://doi.org/10.1126/science.1164680

Blanco, I., Piccari, L., & Barberà, J. A. (2016). Pulmonary vasculature in COPD: The silent component. *Respirology*, *21*(6), 984–994. https://doi.org/10.1111/resp.12772

Breckenridge, R. A. (2013). Animal Models of Myocardial Disease. In *Animal Models for the Study of Human Disease*. https://doi.org/10.1016/B978-0-12-415894-8.00007-5

Breen, E. C., Scadeng, M., Lai, N. C., Murray, F., & Bigby, T. D. (2017). Functional magnetic resonance imaging for in vivo quantification of pulmonary hypertension in the Sugen 5416/hypoxia mouse. *Experimental Physiology*, *102*(3), 347–353. https://doi.org/10.1113/EP086067

Brinjikji, W., Huston, J., Alejandro, R. A., Gyeong-Moon, K., Lerman, A., & Lanzino, G. (2016). Journal of Neurosurgery. *Journal of Neurosurgery*, *124*, 27–42. https://doi.org/10.3171/2015.1.JNS142452.Disclosure

Cahill, E., Rowan, S. C., Sands, M., Banahan, M., Ryan, D., Howell, K., & McLoughlin, P. (2012). The pathophysiological basis of chronic hypoxic pulmonary hypertension in the mouse: Vasoconstrictor and structural mechanisms contribute equally. *Experimental Physiology*, *97*(6), 796–806. https://doi.org/10.1113/expphysiol.2012.065474

Cahill, T. J., Choudhury, R. P., & Riley, P. R. (2017). Heart regeneration and repair after myocardial infarction: Translational opportunities for novel therapeutics. *Nature Reviews Drug Discovery*, *16*(10), 699–717. https://doi.org/10.1038/nrd.2017.106

Cai, J., Hatsukami, T. S., Ferguson, M. S., Kerwin, W. S., Saam, T., Chu, B., … Yuan, C. (2005). In vivo quantitative measurement of intact fibrous cap and lipid-rich necrotic core size in atherosclerotic carotid plaque: Comparison of high-resolution, contrast-enhanced magnetic resonance imaging and histology. *Circulation, 112*(22), 3437–3444. https://doi.org/10.1161/CIRCULATIONAHA.104.528174

Campen, M. J., Shimoda, L. A., & O’Donnell, C. P. (2005). Acute and chronic cardiovascular effects of intermittent hypoxia in C57BL/6J mice. *Journal of Applied Physiology*, *99*(5), 2028–2035. https://doi.org/10.1152/japplphysiol.00411.2005

Caro, G. G. (2009). Discovery of the role of wall shear in atherosclerosis. *Arteriosclerosis, Thrombosis, and Vascular Biology*, *29*(2), 158–161. https://doi.org/10.1161/ATVBAHA.108.166736

Chalupsky, K., Kračun, D., Kanchev, I., Bertram, K., & Görlach, A. (2015). Folic Acid Promotes Recycling of Tetrahydrobiopterin and Protects Against Hypoxia-Induced Pulmonary Hypertension by Recoupling Endothelial Nitric Oxide Synthase. *Antioxidants and Redox Signaling*, *23*(14), 1076–1091. https://doi.org/10.1089/ars.2015.6329

Charolidi, N., & Carroll, V. A. (2017). Hypoxia and Pulmonary Hypertension. In *Hypoxia and Human Diseases*. https://doi.org/10.5772/67151

Chen, M., Shen, C., Zhang, Y., & Shu, H. (2017). MicroRNA-150 attenuates hypoxia-induced excessive proliferation and migration of pulmonary arterial smooth muscle cells through reducing HIF-1α expression. *Biomedicine and Pharmacotherapy*, *93*, 861–868. https://doi.org/10.1016/j.biopha.2017.07.028

Chiu JJ, & Chien C. (2011). Chiu JJ. (2011). NIH Public Access. Physiol Rev, 91(1). https://doi.org/10.1152/physrev.00047.2009.Effects. *Physiol Rev*, *91*(1). https://doi.org/10.1152/physrev.00047.2009.Effects

Cho, G. S., Fernandez, L., & Kwon, C. (2014). Regenerative medicine for the heart: Perspectives on stem-cell therapy. *Antioxidants and Redox Signaling*, *21*(14), 2018–2031. https://doi.org/10.1089/ars.2014.6063

Chuah, S. Y., Attia, A. B. E., Ho, C. J. H., Li, X., Lee, J. S. S., Tan, M. W. P., … Thng, S. T. G.

(2019). Volumetric Multispectral Optoacoustic Tomography for 3-Dimensional Reconstruction of Skin Tumors: A Further Evaluation with Histopathologic Correlation. *Journal of Investigative Dermatology*, *139*(2), 481–485. https://doi.org/10.1016/j.jid.2018.08.014

Cohen, M., Boiangiu, C., & Abidi, M. (2010). Therapy for ST-segment elevation myocardial infarction patients who present late or are ineligible for reperfusion therapy. *Journal of the American College of Cardiology*, *55*(18), 1895–1906. https://doi.org/10.1016/j.jacc.2009.11.087

Damen, F. W., Berman, A. G., Soepriatna, A. H., Ellis, J. M., Buttars, S. D., Aasa, K. L., & Goergen, C. J. (2017). High-Frequency 4-Dimensional Ultrasound (4DUS): A Reliable Method for Assessing Murine Cardiac Function. *Tomography (Ann Arbor, Mich.)*, *3*(4), 180–187. https://doi.org/10.18383/j.tom.2017.00016

Dave, J. K., Mc Donald, M. E., Mehrotra, P., Kohut, A. R., Eisenbrey, J. R., & Forsberg, F. (2018). Recent technological advancements in cardiac ultrasound imaging. *Ultrasonics*, *84*, 329–340. https://doi.org/10.1016/j.ultras.2017.11.013

Davoudi, N., Deán-Ben, X. L., & Razansky, D. (2019). Deep learning optoacoustic tomography with sparse data. *Nature Machine Intelligence*, *1*(10), 453–460. https://doi.org/10.1038/s42256-019-0095-3

Deán-Ben, X. L., Gottschalk, S., Mc Larney, B., Shoham, S., & Razansky, D. (2017). Advanced optoacoustic methods for multiscale imaging of: In vivo dynamics. *Chemical Society Reviews*, *46*(8), 2158–2198. https://doi.org/10.1039/c6cs00765a

Dean-Ben, X. L., Ozbek, A., & Razansky, D. (2013). Volumetric real-time tracking of peripheral human vasculature with GPU-accelerated three-dimensional optoacoustic tomography. *IEEE Transactions on Medical Imaging*, *32*(11), 2050–2055. https://doi.org/10.1109/TMI.2013.2272079

Deán-Ben, X. Luís, Ma, R., Razansky, D., & Ntziachristos, V. (2011). Statistical approach for optoacoustic image reconstruction in the presence of strong acoustic heterogeneities. *IEEE*

Transactions on Medical Imaging, *30*(2), 401–408. https://doi.org/10.1109/TMI.2010.2081683

Deán-Ben, X. Luís, & Razansky, D. (2013). Portable spherical array probe for volumetric real-time optoacoustic imaging at centimeter-scale depths. *Optics Express*, *21*(23), 28062. https://doi.org/10.1364/oe.21.028062

Deán-Ben, Xosé Luís, Bay, E., & Razansky, D. (2014). Functional optoacoustic imaging of moving objects using microsecond-delay acquisition of multispectral three-dimensional tomographic data. *Scientific Reports*, *4*, 1–6. https://doi.org/10.1038/srep05878

Deán-Ben, Xosé Luís, Ford, S. J., & Razansky, D. (2015). High-frame rate four dimensional optoacoustic tomography enables visualization of cardiovascular dynamics and mouse heart perfusion. *Scientific Reports*, *5*(July), 1–9. https://doi.org/10.1038/srep10133

Deán-Ben, Xosé Luís, & Razansky, D. (2013). Functional optoacoustic human angiography with handheld video rate three dimensional scanner. *Photoacoustics*, *1*(3–4), 68–73. https://doi.org/10.1016/j.pacs.2013.10.002

Deán-Ben, Xosé Luís, & Razansky, D. (2016). On the link between the speckle free nature of optoacoustics and visibility of structures in limited-view tomography. *Photoacoustics*, *4*(4), 133–140. https://doi.org/10.1016/j.pacs.2016.10.001

Di Siena, S., Gimmelli, R., Nori, S. L., Barbagallo, F., Campolo, F., Dolci, S., … Pellegrini, M. (2016). Activated c-Kit receptor in the heart promotes cardiac repair and regeneration after injury. *Cell Death and Disease*, *7*(7), 1–15. https://doi.org/10.1038/cddis.2016.205

Dima, A., & Ntziachristos, V. (2012). Non-invasive carotid imaging using optoacoustic tomography. *Optics Express*, *20*(22), 25044. https://doi.org/10.1364/oe.20.025044

Doevendans, P. A., Daemen, M. J., De Muinck, E. D., & Smits, J. F. (1998). Cardiovascular phenotyping in mice. *Cardiovascular Research*, *39*(1), 34–49. https://doi.org/10.1016/S0008-6363(98)00073-X

Ellison, G. M., Vicinanza, C., Smith, A. J., Aquila, I., Leone, A., Waring, C. D., … Nadal-Ginard, B.

(2013). Adult c-kitpos cardiac stem cells are necessary and sufficient for functional cardiac regeneration and repair. *Cell*. https://doi.org/10.1016/j.cell.2013.07.039

Fagan, K. A. (2001). Physiological and Genomic Consequencesof Intermittent Hypoxia Selected Contribution: Pulmonary hypertension in mice following intermittent hypoxia. *Journal of Applied Physiology*, 1600–1605.

Fairhead, J. F., & Rothwell, P. M. (2005a). The Need for Urgency in Identification and Treatment of Symptomatic Carotid Stenosis Is Already Established. *Cerebrovascular Diseases*, *19*(6), 355–358. https://doi.org/10.1159/000085201

Fairhead, J. F., & Rothwell, P. M. (2005b). The Need for Urgency in Identification and Treatment of Symptomatic Carotid Stenosis Is Already Established. *Cerebrovascular Diseases*, *19*(6), 355–358. https://doi.org/10.1159/000085201

Falk, E. (2006). Pathogenesis of Atherosclerosis. *Journal of the American College of Cardiology*, *47*(8 SUPPL.), 0–5. https://doi.org/10.1016/j.jacc.2005.09.068

Finn, A. V., Nakano, M., Narula, J., Kolodgie, F. D., & Virmani, R. (2010). Concept of vulnerable/unstable plaque. *Arteriosclerosis, Thrombosis, and Vascular Biology*, *30*(7), 1282–1292. https://doi.org/10.1161/ATVBAHA.108.179739

Forfia, P. R., Vaidya, A., & Wiegers, S. E. (2013). Pulmonary heart disease: The heart-lung interaction and its impact on patient phenotypes. *Pulmonary Circulation*, *3*(1), 5–19. https://doi.org/10.4103/2045-8932.109910

Ganame, J., Messalli, G., Dymarkowski, S., Rademakers, F. E., Desmet, W., Van De Werf, F., & Bogaert, J. (2009). Impact of myocardial haemorrhage on left ventricular function and remodelling in patients with reperfused acute myocardial infarction. *European Heart Journal*, *30*(12), 1440–1449. https://doi.org/10.1093/eurheartj/ehp093

Goldberger. (2017). *20.Goldberger1988.pdf*.

Gottschalk, S., Degtyaruk, O., Mc Larney, B., Rebling, J., Hutter, M. A., Deán-Ben, X. L., …

Razansky, D. (2019). Rapid volumetric optoacoustic imaging of neural dynamics across the mouse brain. *Nature Biomedical Engineering*, *3*(5), 392–401. https://doi.org/10.1038/s41551-019-0372-9

Gottschalk, S., Fehm, T. F., Deán-Ben, X. L., Tsytsarev, V., & Razansky, D. (2016). Correlation between volumetric oxygenation responses and electrophysiology identifies deep thalamocortical activity during epileptic seizures. *Neurophotonics*, *4*(1), 011007. https://doi.org/10.1117/1.nph.4.1.011007

Granger, D. N., & Kvietys, P. R. (2017). Reperfusion therapy—What's with the obstructed, leaky and broken capillaries? *Pathophysiology*, *24*(4), 213–228. https://doi.org/10.1016/j.pathophys.2017.09.003

Han, M. K., McLaughlin, V. V., Criner, G. J., & Martinez, F. J. (2007). Pulmonary diseases and the heart. *Circulation*, *116*(25), 2992–3005. https://doi.org/10.1161/CIRCULATIONAHA.106.685206

Hanrahan, J. P., Grogan, D. R., Baumgartner, R. A., Wilson, A., Cheng, H., Zimetbaum, P. J., & Morganroth, J. (2008). Arrhythmias in patients with Chronic Obstructive Pulmonary Disease (COPD): Occurrence frequency and the effect of treatment with the inhaled long-acting beta2-agonists arformoterol and salmeterol. *Medicine*, *87*(6), 319–328. https://doi.org/10.1097/MD.0b013e31818fcc02

Heijblom, M., Piras, D., van den Engh, F. M., van der Schaaf, M., Klaase, J. M., Steenbergen, W., & Manohar, S. (2016). The state of the art in breast imaging using the Twente Photoacoustic Mammoscope: results from 31 measurements on malignancies. *European Radiology*, *26*(11), 3874–3887. https://doi.org/10.1007/s00330-016-4240-7

Heresi, G. A., Platt, D. M., Wang, W., Divers, C. H., Joish, V. N., Teal, S. A., & Yu, J. S. (2017). Healthcare burden of pulmonary hypertension owing to lung disease and/or hypoxia. *BMC Pulmonary Medicine*, *17*(1), 1–10. https://doi.org/10.1186/s12890-017-0399-1

Hong, Y. M. (2010). Atherosclerotic cardiovascular disease beginning in childhood. *Korean Circulation Journal*, *40*(1), 1–9. https://doi.org/10.4070/kcj.2010.40.1.1

Howell, K., Preston, R. J., & McLoughlin, P. (2003). Chronic hypoxia causes angiogenesis in addition to remodelling in the adult rat pulmonary circulation. *Journal of Physiology*, *547*(1), 133–145. https://doi.org/10.1113/jphysiol.2002.030676

Hsieh, P. C. H., Segers, V. F. M., Davis, M. E., MacGillivray, C., Gannon, J., Molkentin, J. D., … Lee, R. T. (2007). Evidence from a genetic fate-mapping study that stem cells refresh adult mammalian cardiomyocytes after injury. *Nature Medicine*, *13*(8), 970–974. https://doi.org/10.1038/nm1618

Ivankovic, I., Deán-Ben, X. L., Lin, H. C. A., Zhang, Z., Trautz, B., Petry, A., … Razansky, D. (2019). Volumetric optoacoustic tomography enables non-invasive in vivo characterization of impaired heart function in hypoxic conditions. *Scientific Reports*, *9*(1), 1–8. https://doi.org/10.1038/s41598-019-44818-8

Jacques, S. L. (2013). Erratum: Optical properties of biological tissues: A review (Physics in Medicine and Biology (2013) 58). *Physics in Medicine and Biology*, *58*(14), 5007–5008. https://doi.org/10.1088/0031-9155/58/14/5007

Jaffer, F. A., Calfon, M. A., Rosenthal, A., Mallas, G., Razansky, R. N., Mauskapf, A., … Ntziachristos, V. (2011). Two-dimensional intravascular near-infrared fluorescence molecular imaging of inflammation in atherosclerosis and stent-induced vascular injury. *Journal of the American College of Cardiology*, *57*(25), 2516–2526. https://doi.org/10.1016/j.jacc.2011.02.036

Jaffer, F. A., Kim, D. E., Quinti, L., Tung, C. H., Aikawa, E., Pande, A. N., … Weissleder, R. (2007). Optical visualization of cathepsin K activity in atherosclerosis with a novel, protease-activatable fluorescence sensor. *Circulation*, *115*(17), 2292–2298. https://doi.org/10.1161/CIRCULATIONAHA.106.660340

Jahromi, A. S., Cinà, C. S., Liu, Y., & Clase, C. M. (2005). Sensitivity and specificity of color duplex ultrasound measurement in the estimation of internal carotid artery stenosis: A systematic review and meta-analysis. *Journal of Vascular Surgery*, *41*(6), 962–972. https://doi.org/10.1016/j.jvs.2005.02.044

Jansen, K., Van Soest, G., & van der Steen, A. F. W. (2014). Intravascular photoacoustic imaging: A new tool for vulnerable plaque identification. *Ultrasound in Medicine and Biology*, *40*(6), 1037–1048. https://doi.org/10.1016/j.ultrasmedbio.2014.01.008

Josephson, S. A., Bryant, S. O., Mak, H. K., Johnston, S. C., Dillon, W. P., & Smith, W. S. (2004). Evaluation of carotid stenosis using CT angiography in the initial evaluation of stroke and TIA. *Neurology*, *63*(3), 457–460. https://doi.org/10.1212/01.WNL.0000135154.53953.2C

Kaul, S., & Lindner, J. R. (2004). Visualizing Coronary Atherosclerosis In Vivo: Thinking Big, Imaging Small. *Journal of the American College of Cardiology*, *43*(3), 461–463. https://doi.org/10.1016/j.jacc.2003.11.010

Kazu, K., & Poss, K. D. (2012). Cardiac regenerative capacity and mechanisms. *Annual Review of Cell and Developmental Biology*, *28*, 719–741. https://doi.org/10.1146/annurev-cellbio-101011-155739

Keith, M. C. L., & Bolli, R. (2015). “String Theory” of c-kit ^{pos} Cardiac Cells. *Circulation Research*, *116*(7), 1216–1230. https://doi.org/10.1161/CIRCRESAHA.116.305557

Kern, M. J., Donohue, T., Bach, R., & Aguirre, F. (1992). Interpretation of cardiac pathophysiology from pressure waveform analysis: Cardiac arrhythmias. *Catheterization and Cardiovascular Diagnosis*, *27*(3), 223–227. https://doi.org/10.1002/ccd.1810270314

Knieling, L. (2017). Multispectral Optoacoustic Tomography for Assessment of Crohn’s Disease Activity. *The New England Journal of Medicine*, 1747–1751.

Kojonazarov, B., Belenkov, A., Shinomiya, S., Wilchelm, J., Kampschulte, M., Mizuno, S., … Schermuly, R. T. (2018). Evaluating Systolic and Diastolic Cardiac Function in Rodents Using Microscopic Computed Tomography. *Circulation. Cardiovascular Imaging*, *11*(12), e007653.

https://doi.org/10.1161/CIRCIMAGING.118.007653

Koo, V., Hamilton, P. W., & Williamson, K. (2006). Non-invasive in vivo imaging in small animal research. *Cellular Oncology : The Official Journal of the International Society for Cellular Oncology*, *28*(4), 127–139. https://doi.org/10.1155/2006/245619

Kruizinga, P., van der Steen, A. F. W., de Jong, N., Springeling, G., Robertus, J. L., van der Lugt, A., & van Soest, G. (2014). Photoacoustic imaging of carotid artery atherosclerosis. *Journal of Biomedical Optics*, *19*(11), 110504. https://doi.org/10.1117/1.jbo.19.11.110504

Kumar, A. (2017). Introductory Chapter: Recent Trends in Cardiovascular Risk Factors. In *Recent Trends in Cardiovascular Risks*. https://doi.org/10.5772/intechopen.69159

Lam, C. S. P., Lyass, A., Kraigher-Krainer, E., Massaro, J. M., Lee, D. S., Ho, J. E., … Vasan, R. S. (2011a). Cardiac dysfunction and noncardiac dysfunction as precursors of heart failure with reduced and preserved ejection fraction in the community. *Circulation*, *124*(1), 24–30. https://doi.org/10.1161/CIRCULATIONAHA.110.979203

Lam, C. S. P., Lyass, A., Kraigher-Krainer, E., Massaro, J. M., Lee, D. S., Ho, J. E., … Vasan, R. S. (2011b). Cardiac dysfunction and noncardiac dysfunction as precursors of heart failure with reduced and preserved ejection fraction in the community. *Circulation*, *124*(1), 24–30. https://doi.org/10.1161/CIRCULATIONAHA.110.979203

Lee, Y. T., Lin, H. Y., Chan, Y. W. F., Li, K. H. C., To, O. T. L., Yan, B. P., … Tse, G. (2017). Mouse models of atherosclerosis: A historical perspective and recent advances. *Lipids in Health and Disease*, *16*(1), 1–11. https://doi.org/10.1186/s12944-016-0402-5

Li, Y., Shi, B., Huang, L., Wang, X., Yu, X., Guo, B., & Ren, W. (2016). Suppression of the expression of hypoxia-inducible factor-1α by RNA interference alleviates hypoxia-induced pulmonary hypertension in adult rats. *International Journal of Molecular Medicine*, *38*(6), 1786–1794. https://doi.org/10.3892/ijmm.2016.2773

Lin, H. C. A., Déan-Ben, X. L., Ivankovic, I., Kimm, M. A., Kosanke, K., Haas, H., … Razansky, D.

(2017). Characterization of cardiac dynamics in an acute myocardial infarction model by four-dimensional optoacoustic and magnetic resonance imaging. *Theranostics*, *7*(18), 4470–4479. https://doi.org/10.7150/thno.20616

Lindsey, M. L., Bolli, R., Canty, J. M., Du, X. J., Frangogiannis, N. G., Frantz, S., … Heusch, G. (2018). Guidelines for experimental models of myocardial ischemia and infarction. *American Journal of Physiology - Heart and Circulatory Physiology*, *314*(4), H812–H838. https://doi.org/10.1152/ajpheart.00335.2017

Lindsey, M. L., Kassiri, Z., Virag, J. A. ., Castro Bras, L. E., & Scherrer-Crosbie, M. (2018). Guiedelines for measuring cardiac physiology in mice. *American Journal of Physiology - Heart and Circulatory Physiology*, *314*(733), 752.

Lutzweiler, C., & Razansky, D. (2013). Optoacoustic imaging and tomography: Reconstruction approaches and outstanding challenges in image performance and quantification. *Sensors (Switzerland)*, *13*(6), 7345–7384. https://doi.org/10.3390/s130607345

Madigan, M., & Atoui, R. (2018). Therapeutic use of stem cells for myocardial infarction. *Bioengineering*, *5*(2), 1–18. https://doi.org/10.3390/bioengineering5020028

Makkar, R. R., Smith, R. R., Cheng, K., Malliaras, K., Thomson, L. E. J., Berman, D., … Marbán, E. (2012). Intracoronary cardiosphere-derived cells for heart regeneration after myocardial infarction (CADUCEUS): A prospective, randomised phase 1 trial. *The Lancet*. https://doi.org/10.1016/S0140-6736(12)60195-0

Mandal, S., Deán-Ben, X. L., Burton, N. C., & Razansky, D. (2015). Extending biological imaging to the fifth dimension: Evolution of volumetric small animal multispectral optoacoustic tomography. *IEEE Pulse*, *6*(3), 47–53. https://doi.org/10.1109/MPUL.2015.2409103

Marino, F., Scalise, M., Cianflone, E., Mancuso, T., Aquila, I., Agosti, V., … Torella, D. (2019). Role of c-kit in myocardial regeneration and aging. *Frontiers in Endocrinology*, *10*(June), 1–15. https://doi.org/10.3389/fendo.2019.00371

Massberg, S., Brand, K., Grüner, S., Page, S., Müller, E., Müller, I., … Gawaz, M. (2002). A critical role of platelet adhesion in the initiation of atherosclerotic lesion formation. *Journal of Experimental Medicine*, *196*(7), 887–896. https://doi.org/10.1084/jem.20012044

McGuire, M., & Bradford, A. (1999). Chronic intermittent hypoxia increases haematocrit and causes right ventricular hypertrophy in the rat. *Respiration Physiology*, *117*(1), 53–58. https://doi.org/10.1016/S0034-5687(99)00047-X

McLaughlin, V. V., Presberg, K. W., Doyle, R. L., Abman, S. H., McCrory, D. C., Fortin, T., & Ahearn, G. (2004). Prognosis of pulmonary arterial hypertension: ACCP evidence-based clinical practice guidelines. *Chest*. https://doi.org/10.1378/chest.126.1_suppl.78S

Merčep, E., Deán-Ben, X. L., & Razansky, D. (2018). Imaging of blood flow and oxygen state with a multi-segment optoacoustic ultrasound array. *Photoacoustics*, *10*, 48–53. https://doi.org/10.1016/j.pacs.2018.04.002

Monahan, K., Coffin, S., Lawson, M., Saliba, L., Rutherford, R., & Brittain, E. (2019). Pulmonary transit time from contrast echocardiography and cardiac magnetic resonance imaging: Comparison between modalities and the impact of region of interest characteristics. *Echocardiography*, *36*(1), 119–124. https://doi.org/10.1111/echo.14209

Mughal, M. M., Khan, M. K., Demarco, J. K., Majid, A., Shamoun, F., & Abela, G. S. (2011). Symptomatic and asymptomatic carotid artery plaque. *Expert Review of Cardiovascular Therapy*, *9*(10), 1315–1330. https://doi.org/10.1586/erc.11.120

Muthuramu, I., Lox, M., Jacobs, F., & De Geest, B. (2014). Permanent ligation of the left anterior descending coronary artery in mice: A model of post-myocardial infarction remodelling and heart failure. *Journal of Visualized Experiments*, (94), 1–7. https://doi.org/10.3791/52206

Naylor, A. R., Ricco, J. B., de Borst, G. J., Debus, S., de Haro, J., Halliday, A., … Venermo, M. (2018). Editor's Choice – Management of Atherosclerotic Carotid and Vertebral Artery Disease: 2017 Clinical Practice Guidelines of the European Society for Vascular Surgery (ESVS).

European Journal of Vascular and Endovascular Surgery, *55*(1), 3–81. https://doi.org/10.1016/j.ejvs.2017.06.021

Nitkunanantharajah, S., Hennersperger, C., Dean-Ben, X. L., Razansky, D., & Navab, N. (2018). Trackerless panoramic optoacoustic imaging: a first feasibility evaluation. *International Journal of Computer Assisted Radiology and Surgery*, *13*(5), 703–711. https://doi.org/10.1007/s11548-018-1723-9

Ntziachristos, V., & Razansky, D. (2010). Molecular imaging by means of multispectral optoacoustic tomography (MSOT). *Chemical Reviews*, *110*(5), 2783–2794. https://doi.org/10.1021/cr9002566

Nyman, E., Lindqvist, P., Näslund, U., & Grönlund, C. (2018). Risk Marker Variability in Subclinical Carotid Plaques Based on Ultrasound is Influenced by Cardiac Phase, Echogenicity and Size. *Ultrasound in Medicine and Biology*, *44*(8), 1742–1750. https://doi.org/10.1016/j.ultrasmedbio.2018.03.013

Oraevsky, A. A., Clingman, B., Zalev, J., Stavros, A. T., Yang, W. T., & Parikh, J. R. (2018). Clinical optoacoustic imaging combined with ultrasound for coregistered functional and anatomical mapping of breast tumors. *Photoacoustics*, *12*(August), 30–45. https://doi.org/10.1016/j.pacs.2018.08.003

Ozbek, A., Dean-Ben, X. L., & Razansky, D. (2013). Realtime parallel back-projection algorithm for three-dimensional optoacoustic imaging devices. *Optics InfoBase Conference Papers*, *8800*, 1–6. https://doi.org/10.1117/12.2033376

Phoon, C. K. L., & Turnbull, D. H. (2016). Cardiovascular Imaging in Mice. *Current Protocols in Mouse Biology*, *6*(1), 15–38. https://doi.org/10.1002/9780470942390.mo150122

Pistner, A., Belmonte, S., Coulthard, T., & Blaxall, B. C. (2010). Murine echocardiography and ultrasound imaging. *Journal of Visualized Experiments*, (42), 1–4. https://doi.org/10.3791/2100

Provost, J., Papadacci, C., Arango, J. E., Imbault, M., Fink, M., Gennisson, J. L., … Pernot, M. (2014). 3D ultrafast ultrasound imaging in vivo. *Physics in Medicine and Biology*, *59*(19), L1–

L13. https://doi.org/10.1088/0031-9155/59/19/L1

Razansky, D., Harlaar, N. J., Hillebrands, J. L., Taruttis, A., Herzog, E., Zeebregts, C. J., … Ntziachristos, V. (2012). Multispectral optoacoustic tomography of matrix metalloproteinase activity in vulnerable human carotid plaques. *Molecular Imaging and Biology*, *14*(3), 277–285. https://doi.org/10.1007/s11307-011-0502-6

Regensburger, A. P., Fonteyne, L. M., Jüngert, J., Wagner, A. L., Gerhalter, T., Nagel, A. M., … Knieling, F. (2019). optoacoustic tomography as an imaging biomarker for Duchenne muscular dystrophy. *Nature Medicine*, *25*(December). https://doi.org/10.1038/s41591-019-0669-y

Ron, A., Deán-Ben, X. L., Gottschalk, S., & Razansky, D. (2019). Volumetric optoacoustic imaging unveils high-resolution patterns of acute and cyclic hypoxia in a murine model of breast cancer. *Cancer Research*, *79*(18), 4767–4775. https://doi.org/10.1158/0008-5472.CAN-18-3769

Rosano, G. M., Vitale, C., & Seferovic, P. (2016). Heart failure in patients with diabetes mellitus. *Cardiac Failure Review*, *3*(1), 51–55. https://doi.org/10.15420/cfr.2016

Roth, G. A., Johnson, C., Abajobir, A., Abd-Allah, F., Abera, S. F., Abyu, G., … Murray, C. (2017a). Global, Regional, and National Burden of Cardiovascular Diseases for 10 Causes, 1990 to 2015. *Journal of the American College of Cardiology*, *70*(1), 1–25. https://doi.org/10.1016/J.JACC.2017.04.052

Roth, G. A., Johnson, C., Abajobir, A., Abd-Allah, F., Abera, S. F., Abyu, G., … Murray, C. (2017b). Global, Regional, and National Burden of Cardiovascular Diseases for 10 Causes, 1990 to 2015. *Journal of the American College of Cardiology*, *70*(1), 1–25. https://doi.org/10.1016/j.jacc.2017.04.052

Rouleau, L., Berti, R., Ng, V. W. K., Matteau-Pelletier, C., Lam, T., Saboural, P., … Tardif, J. C. (2013). VCAM-1-targeting gold nanoshell probe for photoacoustic imaging of atherosclerotic plaque in mice. *Contrast Media and Molecular Imaging*, *8*(1), 27–39. https://doi.org/10.1002/cmmi.1491

Schellenberg, M. W., & Hunt, H. K. (2018). Hand-held optoacoustic imaging: A review. *Photoacoustics*, *11*(June), 14–27. https://doi.org/10.1016/j.pacs.2018.07.001

Shah, P. K. (2003). Mechanisms of plaque vulnerability and rupture. *Journal of the American College of Cardiology*, *41*(4 SUPPL. 4), S15–S22. https://doi.org/10.1016/s0735-1097(02)02834-6

Shimoda, L. A., & Semenza, G. L. (2011). HIF and the lung: Role of hypoxia-inducible factors in pulmonary development and disease. *American Journal of Respiratory and Critical Care Medicine*, *183*(2), 152–156. https://doi.org/10.1164/rccm.201009-1393PP

Shors, S. M., Cotts, W. G., Pavlovic-Surjancev, B., François, C. J., Gheorghiade, M., & Finn, J. P. (2003). Heart Failure: Evaluation of Cardiopulmonary Transit Times with Time-resolved MR Angiography. *Radiology*, *229*(3), 743–748. https://doi.org/10.1148/radiol.2293021363

Skrok, J., Shehata, M. L., Mathai, S., Girgis, R. E., Zaiman, A., Mudd, J. O., … Vogel-Claussen, J. (2012). Pulmonary arterial hypertension: MR imaging-derived first-pass bolus kinetic parameters are biomarkers for pulmonary hemodynamics, cardiacfunction, and ventricular remodeling. *Radiology*, *263*(3), 678–687. https://doi.org/10.1148/radiol.12111001

Sonin, D., Papayan, G., Pochkaeva, E., Chefu, S., Minasian, S., Kurapeev, D., … Galagudza, M. (2017). In vivo visualization and ex vivo quantification of experimental myocardial infarction by indocyanine green fluorescence imaging. *Biomedical Optics Express*, *8*(1), 151. https://doi.org/10.1364/boe.8.000151

Sonobe, T., Schwenke, D. O., Pearson, J. T., Yoshimoto, M., Fujii, Y., Umetani, K., & Shirai, M. (2011). Imaging of the closed-chest mouse pulmonary circulation using synchrotron radiation microangiography. *Journal of Applied Physiology*, *111*(1), 75–80. https://doi.org/10.1152/japplphysiol.00205.2011

St. John Sutton, M. G., & Sharpe, N. (2000). Left ventricular remodeling after myocardial infarction: Pathophysiology and therapy. *Circulation*, *101*(25), 2981–2988. https://doi.org/10.1161/01.cir.101.25.2981

Stenmark, K. R., Fagan, K. A., & Frid, M. G. (2006). Hypoxia-induced pulmonary vascular remodeling: Cellular and molecular mechanisms. *Circulation Research*, *99*(7), 675–691. https://doi.org/10.1161/01.RES.0000243584.45145.3f

Stylogiannis, A., Prade, L., Buehler, A., Aguirre, J., Sergiadis, G., & Ntziachristos, V. (2018). Continuous wave laser diodes enable fast optoacoustic imaging. *Photoacoustics*, *9*, 31–38. https://doi.org/10.1016/j.pacs.2017.12.002

Tanai, E., & Frantz, S. (2011). Pathophysiology of heart failure. *Comprehensive Physiology*, *6*(1), 187–214.

Taruttis, A., Timmermans, A. C., Wouters, P. C., Kacprowicz, M., Van Dam, G. M., & Ntziachristos, V. (2016). Optoacoustic imaging of human vasculature: Feasibility by using a handheld probe. *Radiology*, *281*(1), 256–263. https://doi.org/10.1148/radiol.2016152160

Taruttis, A., Wildgruber, M., Kosanke, K., Beziere, N., Licha, K., Haag, R., … Ntziachristos, V. (2013). Multispectral optoacoustic tomography of myocardial infarction. *Photoacoustics*, *1*(1), 3–8. https://doi.org/10.1016/j.pacs.2012.11.001

Thygesen, K., Alpert, J. S., Jaffe, A. S., Simoons, M. L., Chaitman, B. R., White, H. D., … Wagner, D. R. (2012). Third universal definition of myocardial infarction. *Circulation*, *126*(16), 2020–2035. https://doi.org/10.1161/CIR.0b013e31826e1058

Tompkins, B. A., Balkan, W., Winkler, J., Gyöngyösi, M., Goliasch, G., Fernández-Avilés, F., & Hare, J. M. (2018). Preclinical Studies of Stem Cell Therapy for Heart Disease. *Circulation Research*, *122*(7), 1006–1020. https://doi.org/10.1161/CIRCRESAHA.117.312486

Tung, R., & Zimetbaum, P. (2010). Use of the Electrocardiogram in Acute Myocardial Infarction. *Cardiac Intensive Care*, 106–109. https://doi.org/10.1016/B978-1-4160-3773-6.10011-4

Tzoumas, S., Nunes, A., Olefir, I., Stangl, S., Symvoulidis, P., Glasl, S., … Ntziachristos, V. (2016). Eigenspectra optoacoustic tomography achieves quantitative blood oxygenation imaging deep in tissues. *Nature Communications*, *7*(May), 1–10. https://doi.org/10.1038/ncomms12121

Upputuri, P. K., & Pramanik, M. (2016). Recent advances toward preclinical and clinical translation of photoacoustic tomography: a review. *Journal of Biomedical Optics*, *22*(4), 041006. https://doi.org/10.1117/1.jbo.22.4.041006

Urbanek, K., Rota, M., Cascapera, S., Bearzi, C., Nascimbene, A., De Angelis, A., … Anversa, P. (2005). Cardiac stem cells possess growth factor-receptor systems that after activation regenerate the infarcted myocardium, improving ventricular function and long-term survival. *Circulation Research*, *97*(7), 663–673. https://doi.org/10.1161/01.RES.0000183733.53101.11

VanderLaan, P. A., Reardon, C. A., & Getz, G. S. (2004). Site Specificity of Atherosclerosis: Site-Selective Responses to Atherosclerotic Modulators. *Arteriosclerosis, Thrombosis, and Vascular Biology*, *24*(1), 12–22. https://doi.org/10.1161/01.ATV.0000105054.43931.f0

Vandoorne, K., Addadi, Y., & Neeman, M. (2010). Visualizing vascular permeability and lymphatic drainage using labeled serum albumin. *Angiogenesis*, *13*(2), 75–85. https://doi.org/10.1007/s10456-010-9170-4

Vinegoni, C., Botnaru, I., Aikawa, E., Calfon, M. A., Iwamoto, Y., Folco, E. J., … Jaffer, F. A. (2011). Indocyanine green enables near-infrared fluorescence imaging of lipid-rich, inflamed atherosclerotic plaques. *Science Translational Medicine*, *3*(84). https://doi.org/10.1126/scitranslmed.3001577

von Scheidt, M., Zhao, Y., Kurt, Z., Pan, C., Zeng, L., Yang, X., … Lusis, A. J. (2017). Applications and Limitations of Mouse Models for Understanding Human Atherosclerosis. *Cell Metabolism*, *25*(2), 248–261. https://doi.org/10.1016/j.cmet.2016.11.001

Wang, B., Karpiouk, A., Yeager, D., Amirian, J., Litovsky, S., Smalling, R., & Emelianov, S. (2012). In vivo Intravascular Ultrasound-guided Photoacoustic Imaging of Lipid in Plaques Using an Animal Model of Atherosclerosis. *Ultrasound in Medicine and Biology*, *38*(12), 2098–2103. https://doi.org/10.1016/j.ultrasmedbio.2012.08.006

Wang, K., Huang, C., Kao, Y. J., Chou, C. Y., Oraevsky, A. A., & Anastasio, M. A. (2013).

Accelerating image reconstruction in three-dimensional optoacoustic tomography on graphics processing units. *Medical Physics*, *40*(2), 1–15. https://doi.org/10.1118/1.4774361

Wang, L., Zhou, Y., Li, M. X., & Zhu, Y. P. (2014). Expression of hypoxia-inducible factor-1α, endothelin-1 and adrenomedullin in newborn rats with hypoxia-induced pulmonary hypertension. *Experimental and Therapeutic Medicine*, *8*(1), 335–339. https://doi.org/10.3892/etm.2014.1728

Weitzenblum, E. (2003). Chronic cor pulmonale. *Heart (British Cardiac Society)*, *89*(2), 225–230. https://doi.org/10.1136/heart.89.2.225

Wildgruber, M., Bielicki, I., Aichler, M., Kosanke, K., Feuchtinger, A., Settles, M., … Botnar, R. M. (2014). Assessment of myocardial infarction and postinfarction scar remodeling with an elastin-specific magnetic resonance agent. *Circulation: Cardiovascular Imaging*, *7*(2), 321–329. https://doi.org/10.1161/CIRCIMAGING.113.001270

Wilson, B. C., Jermyn, M., & Leblond, F. (2018). Challenges and opportunities in clinical translation of biomedical optical spectroscopy and imaging. *Journal of Biomedical Optics*, *23*(03), 1. https://doi.org/10.1117/1.JBO.23.3.030901

Wu, C., Zhang, Y., Li, Z., Li, C., & Wang, Q. (2016). A novel photoacoustic nanoprobe of ICG@PEG-Ag2S for atherosclerosis targeting and imaging: In vivo. *Nanoscale*, *8*(25), 12531–12539. https://doi.org/10.1039/c6nr00060f

Wu, Y. W., Hsu, P. Y., Lin, Y. H., Cheng, M. F., Ko, C. L., Huang, Y. H., … Hsu, H. H. (2017). Diagnostic and prognostic implications of exercise treadmill and rest first-pass radionuclide angiography in patients with pulmonary hypertension. *Clinical Nuclear Medicine*, *42*(9), e392–e399. https://doi.org/10.1097/RLU.0000000000001720

Xia, J., & Wang, L. V. (2014). Small-animal whole-body photoacoustic tomography: A review. *IEEE Transactions on Biomedical Engineering*, *61*(5), 1380–1389. https://doi.org/10.1109/TBME.2013.2283507

Yamashita, T., Ohneda, O., Nagano, M., Iemitsu, M., Makino, Y., Tanaka, H., … Yamamoto, M. (2008). Abnormal Heart Development and Lung Remodeling in Mice Lacking the Hypoxia-Inducible Factor-Related Basic Helix-Loop-Helix PAS Protein NEPAS. *Molecular and Cellular Biology*, *28*(4), 1285–1297. https://doi.org/10.1128/mcb.01332-07

Yao, L., & Jiang, H. (2011). Photoacoustic image reconstruction from few-detector and limited-angle data. *Biomedical Optics Express*, *2*(9), 2649. https://doi.org/10.1364/boe.2.002649

Yoshimura, S., Kawasaki, M., Yamada, K., Enomoto, Y., Egashira, Y., Hattori, A., … Iwama, T. (2012). Visualization of internal carotid artery atherosclerotic plaques in symptomatic and asymptomatic patients: A comparison of optical coherence tomography and intravascular ultrasound. *American Journal of Neuroradiology*, *33*(2), 308–313. https://doi.org/10.3174/ajnr.A2740

Yu, X., Qian, C., Chen, D. Y., Dodd, S. J., & Koretsky, A. P. (2014). Deciphering laminar-specific neural inputs with line-scanning fMRI. *Nature Methods*, *11*(1), 55–58. https://doi.org/10.1038/nmeth.2730

Zavorsky, G. S., Walley, K. R., & Russell, J. a. (2006). Red cell pulmonary transit times through the healthy human lung Experimental Physiology : *Experimental Physiology*, (2).

Zhang, H. F., Maslov, K., & Wang, L. V. (2008). Effects of wavelength-dependent fluence attenuation on the noninvasive photoacoustic imaging of hemoglobin oxygen saturation in subcutaneous vasculature in vivo. *Photons Plus Ultrasound: Imaging and Sensing 2008: The Ninth Conference on Biomedical Thermoacoustics, Optoacoustics, and Acousto-Optics*, *6856*(2008), 68561T. https://doi.org/10.1117/12.761984

Zhang, Z., Trautz, B., Kračun, D., Vogel, F., Weitnauer, M., Hochkogler, K., … Görlach, A. (2019). Stabilization of p22phox by Hypoxia Promotes Pulmonary Hypertension. *Antioxidants and Redox Signaling*, *30*(1), 56–73. https://doi.org/10.1089/ars.2017.7482

Zhou, B., & Wu, S. M. (2018). Reassessment of c-Kit in cardiac cells a complex interplay between expression, fate, and function. *Circulation Research*, *123*(1), 9–11. https://doi.org/10.1161/CIRCRESAHA.118.313215